

**Self-pulsing 1050 nm quantum dot edge emitting  
laser diodes for optical coherence tomography**

Haoling Liu

PhD Thesis

School of Physics and Astronomy

Cardiff University

December 2010

UMI Number: U585436

All rights reserved

INFORMATION TO ALL USERS

The quality of this reproduction is dependent upon the quality of the copy submitted.

In the unlikely event that the author did not send a complete manuscript and there are missing pages, these will be noted. Also, if material had to be removed, a note will indicate the deletion.



UMI U585436

Published by ProQuest LLC 2013. Copyright in the Dissertation held by the Author.  
Microform Edition © ProQuest LLC.

All rights reserved. This work is protected against  
unauthorized copying under Title 17, United States Code.



ProQuest LLC  
789 East Eisenhower Parkway  
P.O. Box 1346  
Ann Arbor, MI 48106-1346

## DECLARATION

This work has not previously been accepted in substance for any degree and is not concurrently submitted in candidature for any degree.

Signed ..... Haoling Liu ..... (candidate)  
Date ..... 31, 12, 2010 .....

## STATEMENT 1

This thesis is being submitted in partial fulfillment of the requirements for the degree of ..... PhD .....

Signed ..... Haoling Liu ..... (candidate)  
Date ..... 31, 12, 2010 .....

## STATEMENT 2

This thesis is the result of my own independent work/investigation, except where otherwise stated.

Other sources are acknowledged by explicit references.

Signed ..... Haoling Liu ..... (candidate)  
Date ..... 31, 12, 2010 .....

## STATEMENT 3

I hereby give consent for my thesis, if accepted, to be available for photocopying and for inter-library loan, and for the title and summary to be made available to outside organisations.

Signed ..... Haoling Liu ..... (candidate)  
Date ..... 31, 12, 2010 .....

## Abstract

Self pulsed quantum dot lasers are proposed as a means to generate broadband emission in the 1050 nm region for optical coherence tomography applications. Existing quantum dot materials which are not intentionally designed for broadband emission are examined. Devices for self pulsation are configured with split contacts. When operated without a saturable absorber the laser emits a number of discrete narrow (1 nm) modes, which merge to form a broad continuous lasing spectrum (10 nm) on application of the saturable absorber.

Under a continuous drive current, a single mode ridge waveguide laser was operated at 15 °C such that a spectral width of ~ 10 nm at FWHM centred at 1050 nm with an average output power of 7.5 mW was achieved. The measured gain/loss spectra have been used in a rate equation model to explain the spectral broadening that has been obtained and to show that the broadened spectra are consistent with the modulated carrier density expected under Q-switched operation. The mechanism and the operational principle of self pulsation quantum dot lasers have been studied. A comparison with a quantum well material shows that the realisation of self pulsation and the spectrum broadening induced by the self pulsation are closely related to the specific gain spectra of the quantum dot materials. A self pulsed quantum well laser only emits light with a bandwidth of 2.5 nm. Experimental result and simulation show that a bandwidth of ~ 30 nm may be obtained from the existing quantum dot material. If self pulsation can be performed using an intentionally designed quantum dot material for broadband emission, even broader bandwidth may be obtained. This provides a simple technique for generation of fast broadband laser emission not only for OCT but also for other applications.

## Acknowledgements

I would like to thank my supervisor Peter Smowton for his guidance, advice, time, and encouragement throughout my PhD studies. I would also like to thank my supervisor Wolfgang Drexler for his scientific and financial support. I thank my supervisor Huw Summers for his guidance and help for the cleanroom fabrication. I would like to thank Professor Peter Blood for offering me the opportunity to enter the field of laser physics.

Thanks also to everyone in the group who have always been willing to help and made my time at Cardiff enjoyable. Special thanks to Robert Thomas for the daily discussions and helping on the simulation work. Thanks to Ian Sandall, Adrian George, John Thomson for their help at the beginning of my PhD. Thanks to Stella Elliott, Mohamed Al-Ghamdi, Deeple Naidu, James Ferguson and Ian O'Driscoll for the interesting discussions. I would like to thank Gareth Edwards, Karen Barnett, Angela Sobiesierski for the cleanroom processing and Rob Tucker for his help and advice with electronics and workshop.

Finally, I would like to thank my family for their endless support throughout my studies.

# CONTENTS

<b>CHAPTER 1 INTRODUCTION AND BACKGROUND .....</b>	<b>1</b>
1.1 INTRODUCTION.....	1
1.2 THESIS STRUCTURE .....	1
1.3 OPTICAL COHERENCE TOMOGRAPHY .....	2
1.4 RATIONALE OF 1050 NM OCT.....	7
1.5 STATE OF THE ART OCT LIGHT SOURCES AT 1050 NM.....	9
1.6 LASER DIODE BASICS AND QUANTUM DOTS.....	11
1.6.1 <i>Optical transitions</i> .....	11
1.6.2 <i>Laser diode threshold gain</i> .....	15
1.6.3 <i>Quantum dots and density of states</i> .....	16
1.6.4 <i>Broadening in quantum dots</i> .....	20
1.7 DESCRIPTION AND RATIONALE OF SELF PULSATION QD LASER .....	22
1.7.1 <i>Introduction to Q-switching and mode-locking</i> .....	22
1.7.2 <i>Self-pulsation in semiconductor lasers</i> .....	25
1.8 THE AIM OF THE THESIS.....	26
1.9 SUMMARY .....	27
1.10 REFERENCES .....	27
<b>CHAPTER 2 EXPERIMENTAL TECHNIQUES.....</b>	<b>37</b>
2.1 INTRODUCTION.....	37
2.2 MATERIAL DESCRIPTION .....	37
2.3 THE DEVICES.....	42
2.3.1 <i>Stripe laser</i> .....	42
2.3.2 <i>Ridge waveguide laser</i> .....	43
2.3.3 <i>The multisection devices</i> .....	45
2.4 LIGHT-CURRENT MEASUREMENTS.....	46
2.5 FAR FIELD MEASUREMENT .....	48
2.6 SPECTRA MEASUREMENTS.....	48
2.7 TIME-RESOLVED SPECTRA MEASUREMENTS .....	49
2.8 PULSE FREQUENCY MEASUREMENT .....	52
2.9 THE SEGMENTED CONTACT METHOD .....	52
2.9.1 <i>The principle</i> .....	53
2.9.2 <i>The device</i> .....	55
2.9.3 <i>Modal gain</i> .....	55
2.9.4 <i>Modal loss and internal optical loss</i> .....	56
2.9.5 <i>Spontaneous emission</i> .....	58
2.9.6 <i>The setup</i> .....	58

---

2.10 NOISE MEASUREMENT .....	62
2.11 SUPERLUMINESCENT DIODE MEASUREMENT .....	63
2.12 NANOUB DEVICE MEASUREMENTS.....	64
2.13 SUMMARY .....	64
2.14 REFERENCES .....	64
<b>CHAPTER 3 OPTICAL PROPERTIES OF INGAAS QUANTUM DOT LASERS.....</b>	<b>67</b>
3.1 INTRODUCTION.....	67
3.2 MEASUREMENT OF STRIPE LASER .....	67
3.2.1 <i>Light-current characterization</i> .....	67
3.2.2 <i>Optical spectra measurements</i> .....	70
3.2.3 <i>Power measurements</i> .....	76
3.3 RIDGE WAVEGUIDE LASER.....	77
3.3.1 <i>Light-current characterization</i> .....	77
3.3.2 <i>Far field measurement</i> .....	78
3.3.3 <i>Optical spectra measurement</i> .....	79
3.4 GAIN AND LOSS MEASUREMENT .....	81
3.5 SUMMARY .....	84
3.6 REFERENCES .....	85
<b>CHAPTER 4 SELF PULSATION IN QUANTUM DOT LASERS.....</b>	<b>89</b>
4.1 INTRODUCTION.....	89
4.2 MULTI-SECTION STRIPE LASERS .....	89
4.2.1 <i>Light-current measurements</i> .....	91
4.2.2 <i>Spectra broadening due to self-pulsation</i> .....	94
4.2.3 <i>Streak camera measurements</i> .....	95
4.2.4 <i>Pulse frequency measurement</i> .....	96
4.3 MULTI-SECTION RIDGE LASERS .....	98
4.3.1 <i>Spectra broadening due to self pulsation</i> .....	99
4.3.2 <i>Drive current, reverse bias and temperature effects on self-pulsation</i> .....	104
4.4 RATE EQUATION SIMULATION OF SELF PULSATION.....	107
4.4.1 <i>The conditions for self pulsation</i> .....	111
4.4.2 <i>The effect of driving current</i> .....	113
4.4.3 <i>The effect of reverse bias</i> .....	119
4.4.4 <i>The effect of temperature</i> .....	121
4.4.5 <i>The effect of absorber length</i> .....	123
4.4.6 <i>Emission wavelength changes due to self pulsation</i> .....	124
4.4.7 <i>Comparison with a quantum well laser</i> .....	126
4.5 SUMMARY AND DISCUSSION.....	127
4.6 REFERENCES .....	128
<b>CHAPTER 5 MEASUREMENTS OF OTHER LIGHT SOURCES .....</b>	<b>130</b>

5.1 INTRODUCTION.....	130
5.2 EXALOS SLD MEASUREMENTS.....	130
5.3 EC PROJECT LIGHT SOURCE.....	134
5.4 DISCUSSIONS AND SUMMARY .....	138
5.5 REFERENCES .....	139
<b>CHAPTER 6 SUMMARY AND FURTHER WORK.....</b>	<b>140</b>
6.1 SUMMARY .....	140
6.1.1 <i>Broadband emission centred at ~ 1050 nm</i> .....	141
6.1.2 <i>Self pulsation and spectra broadening</i> .....	142
6.1.3 <i>Different effects to the self pulsation</i> .....	143
6.1.4 <i>Comparisons to a quantum well</i> .....	144
6.2 FUTURE WORK .....	145
6.3 REFERENCES .....	146
<b>APPENDIX A: DERIVATIONS FOR THE CAVITY ROUND TRIP RESONANCE CONDITION.....</b>	<b>148</b>
<b>APPENDIX B: MATHCAD CODE FOR THE SIMULATION.....</b>	<b>151</b>
<b>APPENDIX C: PUBLICATIONS AND PRESENTATIONS .....</b>	<b>154</b>

# **Chapter 1 Introduction and background**

## **1.1 Introduction**

The work in this thesis examines self pulsating quantum dot edge emitting laser diodes as a broadband light source for optical coherence tomography (OCT). The work started with analysing the requirements of light sources for state-of-art OCT. This was followed by investigating the optical properties of samples fabricated from different dot materials. I propose that quantum dot materials will have some advantages relative to quantum well materials. The selected dot material has been fabricated into multi-section stripe and ridge structures to realise self-pulsation. Self-pulsation in both structures has been achieved. The effect of spectrum broadening due to self-pulsation has been studied. The modal gain, modal absorption spectra of ridge waveguide laser structures have been measured and these parameters have been used in a rate equation model for simulating self pulsation. Results indicate that the self-pulsing quantum dot laser diodes can be used to generate broadband laser light sources for OCT applications. The cooling system for continuous current operation and the coupling issues from laser diode to a single mode fibre and to an existing OCT system have also been solved. Furthermore, the commercial super luminescent diode (SLD) and the European commission's project SLD devices have been examined.

## **1.2 Thesis structure**

The rest of this chapter provides a general description of OCT and discusses key technological parameters of state-of-art ultra high resolution ophthalmic OCT. It also describes some basic semiconductor physics and the rationale of the project.

Chapter two describes a variety of experimental methods and setups developed in this project. The measured optical properties including emission spectra, optical power of different samples and the modal gain/loss spectra of the examined devices are presented in chapter three. Chapter four uses experimental results to discuss and explain the effect of self pulsation on the broadening of the lasing spectrum. It also presents a rate equation model to simulate the self pulsation and explain the spectra broadening effect. Furthermore, it discusses the function of different parameters for self pulsed quantum dot lasers. Chapter five shows experimental results measured for a commercial SLD and a SLD chip developed within the framework of a European project (NANOUB). Finally, the thesis ends with a conclusion in chapter six, which also points out the future work which would add to the insight gained from this thesis.

### **1.3 Optical coherence tomography**

Medical imaging technologies are crucial for modern medicine, because they can significantly improve early diagnosis and effective treatment of a disease. Since its invention in 1990, optical coherence tomography (OCT) [1.1, 1.2, 1.3] attracted many research groups' as well as industry's interests and underwent rapid technology development. OCT enables non-invasive, high-resolution, cross-sectional as well as three-dimensional imaging of living internal tissue microstructure in a variety of medical fields. The technique was first employed for ophthalmic application, but in combination with endoscopy [1.4] it enables broad usages in the medical field such as cardiology [1.5], gastrointestinal tract diseases [1.6, 1.7] and others. It is also used for dental care [1.8] (investigation of teeth cavities) and dermatology [1.9] (diagnosis of skin cancer). Hence, OCT has become a prominent biomedical tissue imaging technique because it also offers critical advantages over other medical imaging systems, e.g. it offers micrometer

resolution and millimetre penetration depth, which makes it suitable for high resolution morphological tissue imaging. Medical ultrasonography and magnetic resonance imaging (MRI) [1.10] have inferior resolution; confocal microscopy [1.11] lacks millimetre penetration depth. Unlike technologies such as MRI or X-ray computed tomography (CT) [1.12] OCT can be engineered into a compact, portable, and relatively inexpensive instrument, allowing cost-effective screening and wide clinical accessibility. Instead of using X-ray radiation, OCT uses light in the wavelength region ranging from 400 to 1700 nm which has much a reduced potential hazard to human health. This enables OCT to perform non-invasive imaging as well as monitoring of disease progression or real time investigation of the dynamic response to therapeutic agents. One major drawback of OCT as compared to full-body imaging techniques is its limited penetration depth into non-transparent biological tissue. The maximum OCT imaging depth in most tissues (other than the eye) is limited by optical attenuation and scattering to approximately 1 to 2 mm [1.1]. The eye is essentially transparent, transmitting light with only minimal optical attenuation and scattering and provides easy optical access to the anterior segment as well as the retina. Hence, ophthalmic OCT is the largest application. For different OCT applications, the wavelength applied and the technique demands may be various because of the different absorbing and scattering properties of the tissues.

OCT is an optical analogue to ultrasound. Instead of sound waves, a special broad band light source in combination with low coherence interferometry [1.13] is used in OCT. Therefore OCT imaging can be performed without the need for direct contact with the tissue, and therefore increases the patient's comfort. The light non-invasively probes the investigated tissue to visualise its structure with high resolution. A broadband source in combination with a Michelson interferometer is used to locate the sites of light reflections within the tissue and two or

three dimensional images of the investigated tissue can be acquired. The principle of OCT is based on low coherence interferometry. Light emitted by the source is split into two arms (see figure 1.1) -- a sample arm (containing the item of interest) and a reference arm (usually a mirror). The combination of reflected light from the sample and the reference gives rise to an interference pattern if light from both paths have travelled approximately the same optical distance (a difference less than a coherence length) and low coherent, i.e. polychromatic light is used.

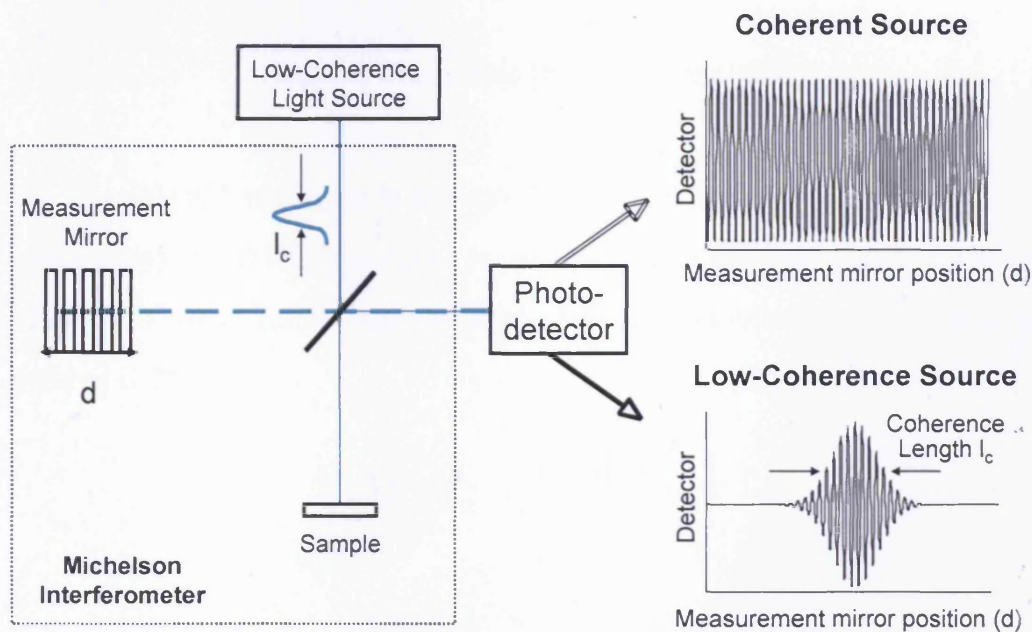


Figure 1.1 Low-Coherence Interferometry

Initially, OCT instruments were operated in the so called time domain. There are two basic scan procedures in time domain OCT: the (one-dimensional) axial scan (see figure 1.2), also referred to as depth scan or A-scan, it is performed by moving the reference mirror. The (two-dimensional) lateral scan (B-scan, see figure 1.2) is either performed by moving the sample or by scanning the probe beam illuminating the sample. Combining these scans in the third dimension, a 3-D image can be obtained.

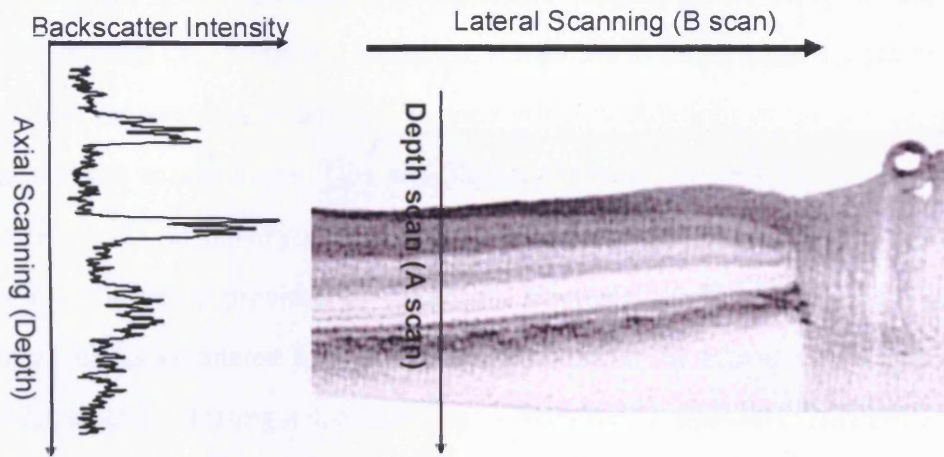


Figure 1.2 Time domain OCT, A scan and B scan

Lateral OCT resolution is governed by the focal spot size (as in conventional microscopy). Axial OCT resolution is mainly determined by the coherence length of the light source (rather than the depth of field, as in microscopy) and it is defined as [1.2]:

$$\Delta z = l_c \approx 0.44 \left( \frac{\lambda^2}{\Delta \lambda} \right) \quad (1.1)$$

where  $\lambda$  is the centre wavelength and  $\Delta \lambda$  is the bandwidth of the light source (full-width-at-half-maximum assuming a Gaussian distribution). Therefore, the specifications of the light source mainly determine the visualisation performance of OCT. Based on the same principle, two sets of the OCT system have been developed, free-space optics based OCT [1.14, 1.15] and fibre optics based OCT [1.3]. The speed of time-domain OCT is limited by the mechanical movements of the reference mirror and system sensitivity that make them unsuitable for in vivo 3-D (retinal) imaging. In recent years, frequency domain OCT (FD-OCT) [1.16, 1.17, 1.18], also referred to as spectral or Fourier domain OCT, has proven to

combine high speed and ultrahigh resolution imaging [1.19, 1.20]. In the frequency domain OCT, only the lateral OCT scan has to be performed since the total A-scan information is detected by measuring modulations of the source spectrum using a spectrometer. This significantly reduces the imaging time and increases OCT efficiency/sensitivity. The axial information (time domain data/information) is provided by an inverse Fourier Transform (FT) of the spectrum of the backscattered light [1.2]. The spectrum of the backscattered light amplitude is obtained using a spectrometer. A sketch of a state-of-the-art frequency domain OCT system is shown in Figure 1.3.

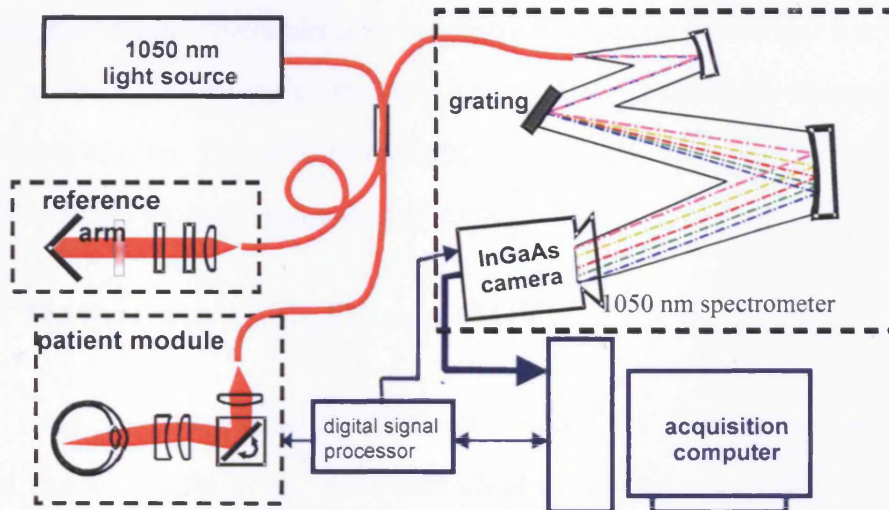


Figure 1.3 Schematics of the 1050 nm frequency domain OCT system [1.21]

The broadband source is interfaced to a fibre-optic interferometer where the first arm is sent to an adjustable reference mirror in a free-space portion including dispersion compensation and an attenuator. The patient model consists of collimation and focusing optics and a 2-D scanner. On its way back, the light from the sample arm is recombined with the reference light, producing a spectral interference pattern that is sent to an all-reflective imaging spectrometer with a reflective planar grating. The signal is detected by the InGaAs camera and post processed by a digital signal processor (DSP). The DSP controls the mechanical scanning sys-

tem in the patient module, while the image is presented on a personal computer.

There are some parameters which can affect the quality of imaging regarding resolution and penetration. Adaptive optics or digital imaging processing may improve lateral OCT image resolution (see figure 1.2) but the light source applied is the fundamental factor for improving OCT imaging quality in terms of axial resolution and contrast. As described, the axial resolution (see figure 1.2) is determined by the coherence length of the light source. The coherence length is inversely proportional to the spectral bandwidth of the light source, therefore in order to obtain a high axial OCT resolution we need a broadband light source. The penetration depth is determined by the centre wavelength of the light source and is also related to the power of the light source. These factors are discussed in the following section. The noise of the light source is also an important parameter to have optimum dynamic range in OCT tomograms.

## **1.4 Rationale of 1050 nm OCT**

Until now, three generations of commercial OCT systems have been developed and successfully used in several clinical studies [1.22, 1.23, 1.24]. So far clinical ophthalmic OCT has been performed in the 800 nm region because the eye is essentially transparent in this region. OCT penetration is mostly limited by water absorption of structures such as the cornea, lens, and vitreous – the first two intraocular elements focus light onto the retina (see figure 1.4).

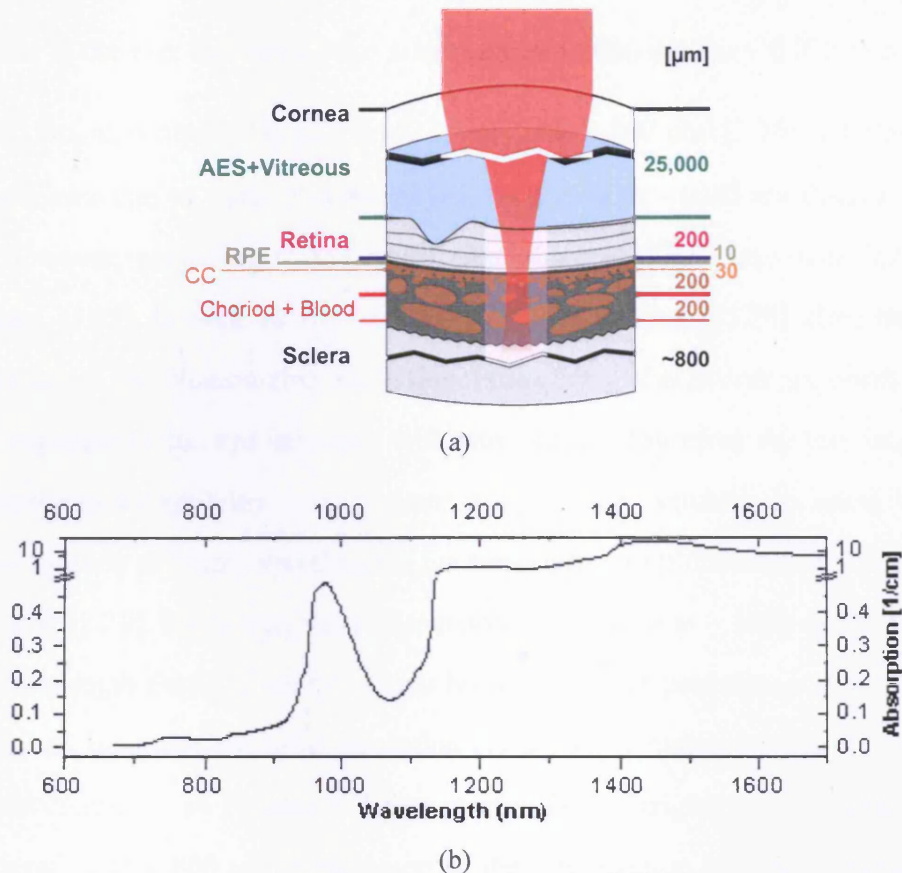


Figure 1.4 (a) simple eye model, (b) water absorption spectrum [1.25]

The absorption of intraocular media features two usable regions (see figure 1.4 (b)), separated by a water absorption peak at  $\sim 970$  nm; the lower wavelength region covers the visible and the near-range infrared up to  $\sim 950$  nm. The second window is narrower and restricted to  $\sim 100$  nm of bandwidth centred at  $\sim 1050$  nm. Clinical ophthalmic OCT, operating at a wavelength of  $\sim 800$  nm, is optimally suitable to resolve all main intraretinal layers and small morphological changes within these layers, however the penetration depth beyond the retina is limited by the highly absorbing and scattering retinal pigment epithelium (RPE), resulting mainly in visualizing the retina and superficial parts of the choriocapillaris/choroid. The absorbing and scattering of RPE decreases monotonically with increasing wavelength [1.25]; the attenuation of light is also limited by water ab-

sorption in the eye, that has a local minimum at  $\sim 1060$  nm ( $\mu_a \sim 0.015$  mm<sup>-1</sup> at  $\lambda = 1060$  nm, as compared to  $\mu_a \sim 0.0023$  mm<sup>-1</sup> at  $\lambda = 800$  nm) [1.26], meaning that power losses due to water absorption will be greater at  $\sim 1060$  nm than at  $\sim 800$  nm. However, according to the ANSI (American National Standards Institute) standard [1.27] as well as the similar ICNIRP-guidelines [1.28] (International Commission for Nonionizing Radiation Protection), the maximum permissible light exposure in the eye increases with wavelength. Therefore the loss might be compensated by applying up to 5 times more power. Actually, by using higher incident power at longer wavelengths the sensitivity of ophthalmic OCT has been improved [1.29]. Moreover, water dispersion equals zero at  $\sim 1000$  nm [1.30]. At this wavelength the OCT sample signal broadening with penetration depth is negligible and therefore the axial resolution stays approximately constant over reasonable depth. It can be assumed that in vivo OCT imaging at 1050 nm wavelength rather than 800 nm should improve the visualization of morphological features beneath the RPE as well as layers of the choroids. Several 1050 nm OCT results have already shown deeper penetration into the tissue [1.21, 1.25, 1.29]. This might significantly improve the early diagnosing and treatments of retinal diseases that are the worldwide leading causes for blindness.

## 1.5 State of the art OCT light sources at 1050 nm

As discussed, the performance of OCT imaging is mainly governed by the light source applied. OCT light sources can be characterized mainly by central wavelength, bandwidth and power. In addition, optical noise, spectral shape, power stability, user friendliness as well as compactness are all critical parameters. Several different types of light source have been used for OCT applications so far including: solid state lasers, photonic crystal fibre (PCF) based super continuum

generation light sources, amplified spontaneous emission (ASE) fibre lasers, and super luminescent diodes (SLDs). Solid state titanium sapphire lasers have successfully enabled ultrahigh resolution of OCT. Operating at  $\sim 800$  nm; a high axial resolution of up to  $\sim 3$   $\mu\text{m}$  in vivo has been achieved [1.31, 1.32]. The drawback of this kind of laser is the requirement of an expensive pump laser, making the whole light source bulky and expensive. Recently, PCF based super continuum generation has shown spectral broadening due to nonlinear optical effects [1.33]. Using a Ti:sapphire laser to pump PCF, B. Považay et al [1.29] has generated a super continuum spanning from 400 to 1200 nm. The smooth Gaussian shaped spectrum with 325 nm bandwidth at full width at half maximum (FWHM) centred at 700 nm with 10 mW average output power could be used for OCT. However, this kind of external broadening often results in significant power fluctuations, spectral modulations and excess noise (in addition to the noise of the pump source) [1.34]. Super continuum generation often produces intensity noise of many tens of decibels above the pump noise [1.35], which introduces difficulties for OCT imaging. Furthermore, the setup is large, complicated and expensive, making it inadequate for practical OCT. NP photonics<sup>1</sup> offers Ytterbium-doped fibre ASE broadband light sources in the wavelength range of 1000 nm to 1100 nm. OCT experiments using this kind of light source have shown enhanced penetration depth [1.21, 1.25]. The drawback of this source is that it is expensive and still bulky to interface it to a compact OCT system. SLDs have the advantages of being inexpensive, compact and easy to operate. Hence, several OCT studies have been performed with SLD sources [1.36, 1.37]. The reported results are obtained by using an SLD in the  $\sim 800 - 900$  nm region, or in the 1300 nm region. Using SLDs for the 1050 nm OCT region remains relatively unexplored. This is mainly due to the limited number of available SLD sources with proper specifications for

---

<sup>1</sup> <http://www.npphotonics.com>

OCT. However, Superlum Diodes Ltd<sup>2</sup> provides SLDs centred at 1060 nm with a bandwidth at FWHM of 35 nm and 30 mW single mode fibre output. Qphotonics LLC<sup>3</sup> offers SLD centred at 1050 nm with a bandwidth (FWHM) of 60 nm and free space output power of 5 mW, while also offering a fibre coupled SLD with output from a fibre pigtail of 1.5 mW. Other major light source suppliers NP Photonics, Multiwave<sup>4</sup>, Exalos<sup>5</sup> and Inphenix<sup>6</sup> do not offer SLDs working in the 1050 nm region. The drawbacks of these SLD sources are their low power output and insufficient bandwidth. Recently, scientists have shown that quantum dots (QDs) enable semiconductor diode lasers to emit a broad spectrum of light [1.38, 1.39]. Hence, this work focuses on studying and fabricating a broadband laser diode at ~ 1050 nm for OCT applications.

## 1.6 Laser diode basics and quantum dots

In this section, the basic principles of laser diode and quantum dots are introduced. The optical transitions that take place in a general two level system are first discussed.

### 1.6.1 Optical transitions

There are three possible optical transitions that can occur between two energy states. These are absorption, spontaneous emission and stimulated emission (see figure 1.5). In an absorption event an electron is initially occupying a lower energy state ( $E_1$ ), and an incoming photon with an energy equal to the band gap ( $h\nu$ ) is ‘absorbed’ by the electron, causing the electron to undergo a transition

---

<sup>2</sup> <http://www.superlumdiodes.com>

<sup>3</sup> <http://www.qphotonics.com>

<sup>4</sup> <http://www.multiwavephotonics.com>

<sup>5</sup> <http://www.exalos.com>

<sup>6</sup> <http://www.inphenix.com>

to a higher energy state (E2). Similarly a spontaneous emission event occurs when an electron with higher energy (E2) spontaneously “falls” to the lower energy level (E1) releasing a photon in the process. The energy of this photon is again equal to the energy difference between the two states, where:

$$E_2 - E_1 = h\nu \quad (1.2)$$

A stimulated emission event occurs when an incoming photon (with energy equal to the difference between the two states) perturbs an electron in the upper state (E2). This results in the electron falling down to the lower state (E1) releasing another photon in the process. As well as having the same energy as the first photon the second photon is coherent with the first (has the same polarization, phase and direction).

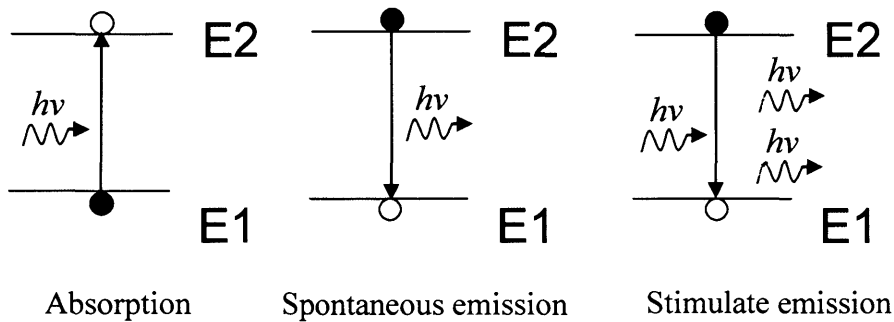


Figure 1.5 optical transitions in 2 level system

The rate of the transitions in a two level system is described using Einstein coefficients [1.40]. The downwards transition rate due to spontaneous emission is proportional to the number density of electrons in this state  $N_2$  and the Einstein coefficient  $A_{21}$ :

$$R_{spon} = A_{21}N_2 \quad (1.3)$$

The upward transition rate due to absorption is proportional to the number density of electrons in this state  $N_1$ , the Einstein coefficient  $B_{12}$  and to the density of photons in the optical field with energy equal to the difference between the two

states  $P(h\nu)$ .

$$R_{abs} = B_{12}N_1P(h\nu) \quad (1.4)$$

The downward transition rate due to stimulated emission is proportion to the number density of electrons in this state  $N_2$ , the Einstein coefficient  $B_{21}$  and the photon density.

$$R_{stim} = B_{21}N_2P(h\nu) \quad (1.5)$$

Under equilibrium conditions the upward and downwards transition rates must balance so,

$$R_{abs} = R_{spont} + R_{stim} \quad (1.6)$$

$$B_{12}N_1P(h\nu) = A_{21}N_2 + B_{21}N_2P(h\nu) \quad (1.7)$$

$$\text{where } B_{12} = B_{21} \quad (1.8)$$

$$A_{21} = \frac{8\pi n^3}{h^3 c^3} (h\nu)^2 B_{21} \quad (1.9)$$

The unit of  $A_{21}$  is related to the spontaneous lifetime of a transition by:

$$A_{21} = \frac{1}{\tau_s} \quad (1.10)$$

For a system containing closely spaced states, the behaviour of the system as a whole is related to the properties of the particles within the system and can be determined using statistical physics. The number of particles per unit volume with energy between  $E$  and  $E + \Delta E$  in each energy states depends upon the density of available energy states (number of energy states per unit volume in the interval  $\Delta E$ ) and the probability that a particle is in the energy state  $E$ .

$$n(E)\Delta E = \rho(E)f(E)\Delta E \quad (1.11)$$

In semiconductors, electrons are Fermions with half integer spin which obey the

Pauli exclusion principle, the probability an electron occupying a state of energy  $E$  can be described by a Fermi-Dirac distribution for the conduction and valence bands as:

$$f_c = \frac{1}{1 + \exp\left(\frac{E_c - E_{f_c}}{kT}\right)} \quad (1.12)$$

$$f_v = \frac{1}{1 + \exp\left(\frac{E_v - E_{f_v}}{kT}\right)} \quad (1.13)$$

where  $k$  is the Boltzmann constant,  $T$  is the temperature.  $E_{f_c}$ ,  $E_{f_v}$  are the quasi Fermi levels for the electrons in the conduction and valence bands respectively.  $E_c$ ,  $E_v$  represents an energy state in the conduction or valence band. Thus, in semiconductors, the rates for absorption, spontaneous emission, and stimulated emission are described by:

$$R_{abs} = B_{12} \rho_{red} f_v (1 - f_c) P(h\nu) \quad (1.14)$$

$$R_{spont} = A_{21} \rho_{red} f_c (1 - f_v) \quad (1.15)$$

$$R_{stim} = B_{21} \rho_{red} f_c (1 - f_v) P(h\nu) \quad (1.16)$$

Here the availability of electron/hole pairs is given by the reduced density of states [1.41] of the material with the occupation probability of electrons in the conduction and valence bands. A comparison of the stimulated emission and absorption, once the occupation probabilities have been substituted for, gives the expression in equation (1.17):

$$\frac{R_{stim}}{R_{abs}} = \exp\left(\frac{\Delta E_f - (E_c - E_v)}{kT}\right) \quad (1.17)$$

This expression demonstrates that the stimulated emission rate will exceed the absorption rate in a semiconductor when:

$$\Delta E_f > E_c - E_v \geq E_g \tag{1.18}$$

where  $\Delta E_f$  is the quasi-Fermi level separation. This means that for optical gain to occur in a semiconductor laser, the quasi-Fermi level separation must be greater than the photon energy of interest, or at least equal to the band gap of the material. This can be realized by forward biasing a p-n junction.

### 1.6.2 Laser diode threshold gain

As an acronym, LASER stands for Light Amplification by Stimulated Emission of Radiation. For this to occur, stimulated emission must dominate over absorption and spontaneous emission. This can be achieved by optical pumping or electronic pumping. In laser diodes, electrons in the active layer are excited electrically into non-equilibrium higher energy states by injecting the carriers through a p-n junction. The electrons can then relax back into an equilibrium state releasing a photon through spontaneous emission. The end facets of laser diode chips consist of partially reflecting mirrors formed by an air/semiconductor interface. This forms a laser cavity (see figure 1.6) and as the photon travels back and forth within the cavity it grows in intensity due to stimulated emission. Finally, the diode starts to lase.

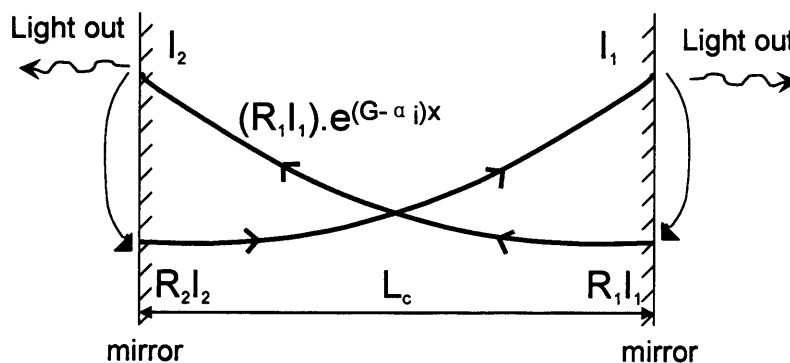


Figure 1.6 Laser round trip condition

Laser action can be sustained when the round-trip amplification replaces light lost from the laser cavity. The gain required to achieve this threshold is given by:

$$G = \alpha_i + \frac{1}{2L_c} \ln\left(\frac{1}{R_1 R_2}\right) \quad (1.19)$$

Where  $\alpha_i$  is the intrinsic scattering loss of the cavity and the second term in the equation are the mirror losses.  $L_c$  is the cavity length;  $R_1$  and  $R_2$  are the intensity reflectivity of the two mirrors.

### 1.6.3 Quantum dots and density of states

Quantum dots are materials with dimensions of the order of nanometres. There are mainly two kinds of quantum dots: colloidal quantum dots and self-assembled quantum dots. Colloidal quantum dots are semiconductor nanocrystals, dispersed in a solvent, with the size of 2-10 nanometres. Self-assembled quantum dots are typically between 10 and 50 nm in size.

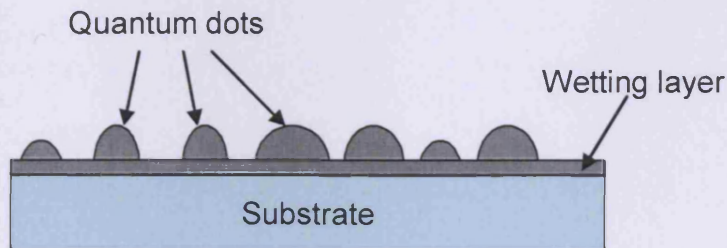


Figure 1.7 Self-assembled quantum dots

The self assembled quantum dots used in this work were grown by molecular beam epitaxial growth methods [1.42] (other methods like Metal Organic Vapor Phase Epitaxial Growth [1.43, 1.44] can also be used). When a material (e.g. In-

GaAs) is grown on a substrate to which it is not lattice matched (e.g. GaAs), the material initially forms a thin film, known as the wetting layer, the resulting strain then produces coherently strained islands on top of the wetting layer (See figure 1.7). This growth mode is known as Stranski-Krastanov growth mode [1.45, 1.46]. The properties of the islands formed including size, shape, density, uniformity are all very sensitive to the growth conditions and can lead to difficulties in trying to obtain reproducible structures.

The density of states (DOS) of a system describes the number of states at each energy level that are available to be occupied. The function depends on the size of the crystal. When the size of the crystal is reduced to a nanometer scale in one direction and the crystal is surrounded by other crystals acting as potential barriers, the freedom of electron movement is lost in that direction. It is well known that quantum dots system has quantized density of states function. This results from the small size of dot, which confines the movement of conduction band electrons and valence band holes in all three spatial directions. Figure 1.8 demonstrates how the reduced size of the confinement system affects the density of states.

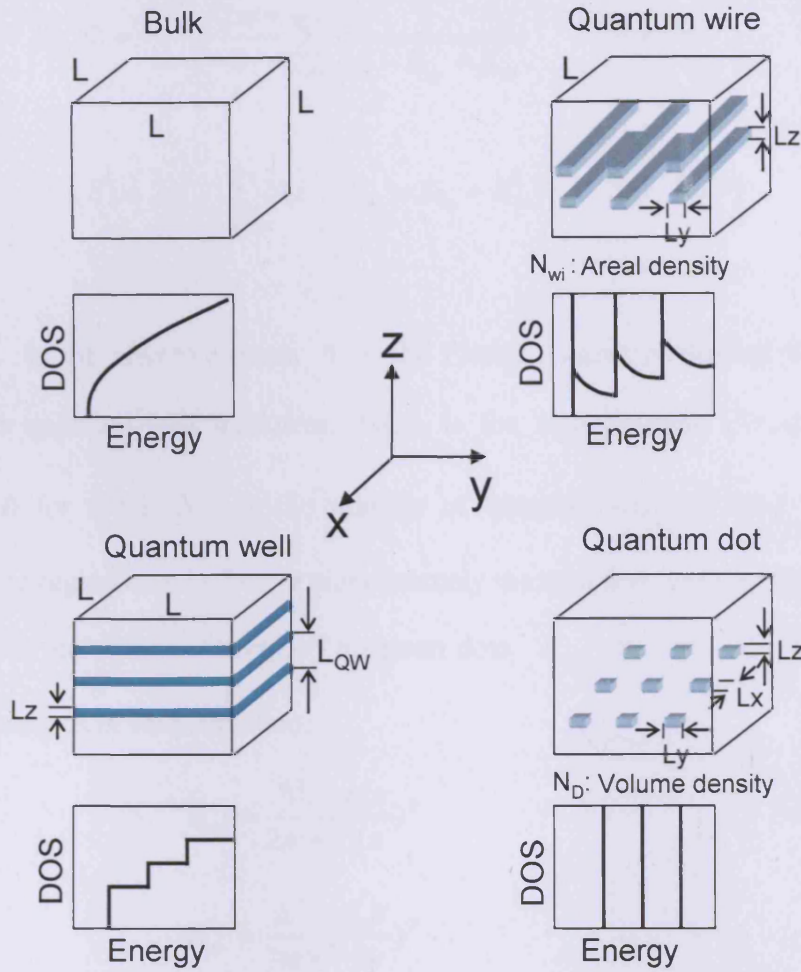


Figure 1.8 Schematic of quantum nano-structures and their density of states [1.47]

Electrons in bulk move freely in all three directions. Electrons in the quantum well move in the x-y plane; those in the quantum wire move in the x direction; and those in the quantum dot are completely localized. The density of states functions can be derived as [1.47]:

$$\text{Bulk: } D(E) = \frac{1}{2\pi^2} \left( \frac{2m^*}{\hbar^2} \right)^{\frac{3}{2}} E^{\frac{1}{2}} \quad [eV^{-1}m^{-3}] \quad (1.20)$$

$$\text{Well: } D(E) = \frac{m^*}{\pi\hbar^2 L_{QW}} \sum_{n_z} \Theta(E - E_{n_z}) \quad [eV^{-1}m^{-3}] \quad (1.21)$$

$$\text{Wire: } D(E) = \frac{N_{wi}}{\pi} \frac{\sqrt{2m^*}}{\hbar} \sum_{ny,nz} \frac{1}{\sqrt{E - E_{ny} - E_{nz}}} \quad [eV^{-1}m^{-3}] \quad (1.22)$$

$$\text{Dots: } D(E) = 2N_D \sum_{nx,ny,nz} \delta(E - E_{nx} - E_{ny} - E_{nz}) \quad [eV^{-1}m^{-3}] \quad (1.23)$$

where,  $m^*$  is the effective mass;  $\hbar$  is the Planck's constant divided by  $2\pi$ ,  $L_{QW}$  is the quantum-well thickness.  $\Theta(x)$  is the step function ( $\Theta(x)=1$  for  $x \geq 0$  and 0 for  $x < 0$ ).  $N_{wi}$  is the number of quantum wires divided by the quantum-wire region area in the y-z plane, namely the area density of the quantum wires.  $N_D$  is the volume density of quantum dots.  $E_{nx}$ ,  $E_{ny}$ , and  $E_{nz}$  are the quantized energies in each direction:

$$E_{nx} = \frac{\hbar^2}{2m^*} \left( \frac{n_x \pi}{Lx} \right)^2 \quad (1.24)$$

$$E_{ny} = \frac{\hbar^2}{2m^*} \left( \frac{n_y \pi}{Ly} \right)^2 \quad (1.25)$$

$$E_{nz} = \frac{\hbar^2}{2m^*} \left( \frac{n_z \pi}{Lz} \right)^2 \quad (1.26)$$

where  $n_x, n_y, n_z = 1, 2, 3 \dots$ ,  $Lx, Ly, Lz$  are the dimensions describing well width, wire area or dot size respectively.

The density of states function for bulk has a parabolic shape, the density of states for quantum well is step like, and the density of quantum dots is a series of delta functions. Many of the predicted improvements in performance in quantum dots systems originate from the three dimensional confinement of carriers. These discrete energy levels are similar to the energy levels within an atom. The ideal dots will have well separated energy levels so only the ground state is populated

(See figure 1.9).

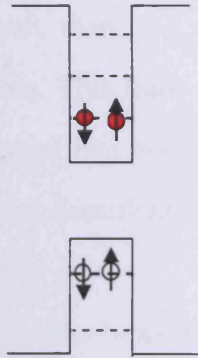


Figure 1.9 Energy diagram of an ideal dot [1.48]

The recombination only occurs between a single pair of discrete states. This requires every dot to have identical size, composition through out the whole ensemble. Thus, dots having same energy states can provide narrow spectral emission lines and reduced threshold current. However, real self-assembled dots often have different size (see figure 1.7), shape and composition due to the growth method itself. This leads to the broadening of the spectral line/gain band width which is considered one of the main “problems” for developing single mode QD laser diode. This however makes the broadband laser (as distinct from the conventional high coherent narrow line width laser) a suitable application for QD laser diodes.

### 1.6.4 Broadening in quantum dots

The self-assembly process leads to typical dot densities of  $10^{10} - 10^{11} \text{ cm}^{-2}$ , with dimensions 5 nm high and base dimensions  $20 \text{ nm} \times 20 \text{ nm}$  [1.49]. According to this, a 2 mm long ridge waveguide laser (ridge width  $2 \mu\text{m}$ ) with one dot layer will contain  $4 \times 10^5 - 4 \times 10^6$  quantum dots. There are fluctuations in the

size, shape, composition and distribution. These could arise from fluctuations in surface roughness, surface temperature or the ion concentrations within the growth chamber [1.50]. As a result, there is a variation in the energy level configuration throughout the ensemble. This leads to an inhomogeneous broadening of the gain spectrum and the spectral line width typically  $\geq 20\text{meV}$  [1.49]. The inhomogeneous broadening can be described by a Gaussian function in energy over the ensemble.

Another type of broadening is the homogeneous broadening from each dot itself. This broadening comes from the uncertainty in the energy of the confined electron and interaction of the confined state with the high frequency lattice vibrations [1.51]. This type of broadening is normally described by a Lorentzian function. The broadening in InGaAs QDs has been estimated to be  $6\text{meV}$  at  $300\text{K}$  [1.52]. Figure 1.10 illustrates the spectral broadening caused by Inhomogeneous and homogeneous broadening.

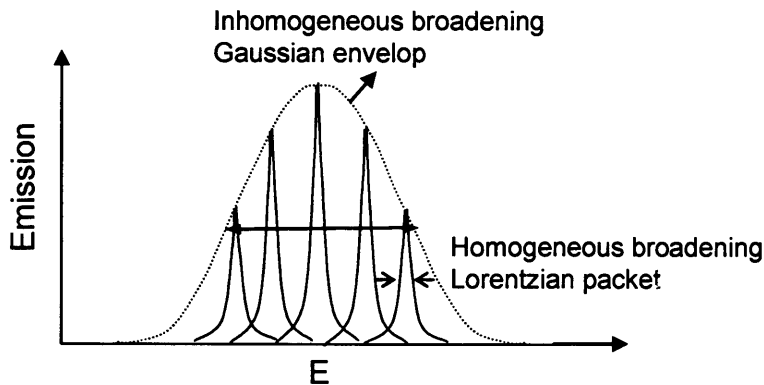


Figure 1.10 Illustration of inhomogeneous and homogeneous broadening in QDs

Recently, quantum dot lasers with a  $75\text{ nm}$  broad spectrum of emission have been reported [1.39]. This is achieved by means of intentional inhomogeneous broadening of the quantum dot energy levels.

## **1.7 Description and rationale of self pulsation QD laser**

Self-pulsation is a technique by which a laser can be forced to produce a pulsed output beam. The technique allows the production of light pulses with extremely high peak power, much higher as compared to the same laser when operating in a continuous wave mode. The pulsed operation can be used to generate broadband emission. The spectral increase can be thought of in terms of Fourier functions. Any signal with a very short time span but an oscillating nature, such as a pulse of light, will have many frequency components when Fourier transformed. If the pulse duration can be made very small, the bandwidth of the laser pulses will be sufficiently broad. Self-pulsation can be realised by introducing a saturable absorber in the cavity of laser diodes. In this way, one could perform Q-switching and/or mode-locking.

### **1.7.1 Introduction to Q-switching and mode-locking**

Q-switching and mode locking are two techniques in optics by which a laser can be made to produce pulses of light. Q-switching is obtained by altering the quality factor (Q-factor) of the laser cavity. Mode locking can be obtained by fixing the phase relationship between the modes of the laser's resonant cavity.

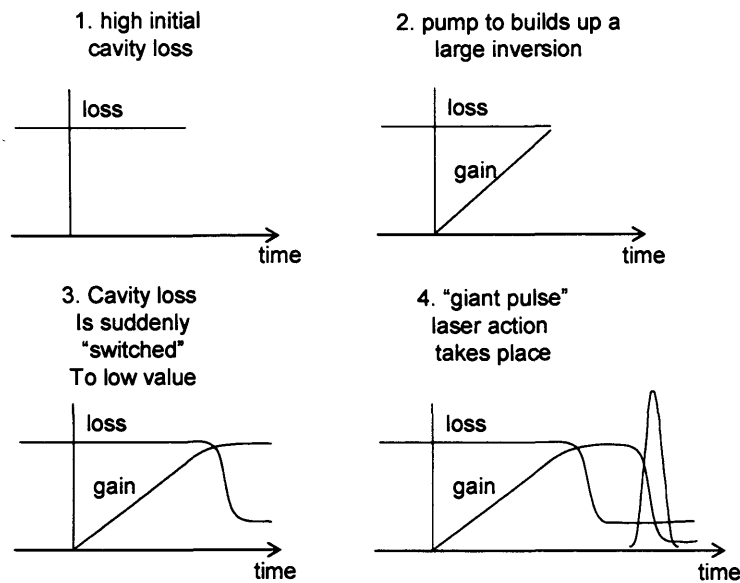


Figure 1.11 Laser Q-switching, step-by-step [1.51]

Figure 1.11 illustrates the steps in the Q-switching technique. The losses of the laser cavity initially are kept at a high level (low Q-factor), thus allowing a laser pumping process to build up a much larger than the usual population inversion inside a laser cavity. Once a large inversion has been developed, the losses are restored to the usual value (switched to high Q-factor). The result is a very short, intense burst of laser output or "giant pulse" which dumps all the accumulated population inversion in a single short laser pulse. Repetitive Q-switching can be achieved by repetitively altering the cavity losses. The Q-switching technique can be applied to different laser systems such as gas, solid state, molecular and semiconductor lasers.

The losses of the cavity can be altered by either active or passive methods. The common active methods are: rotating mirror Q-switching, electro-optic Q-switching, and acousto-optic Q-switching. These methods use different active modulation mechanism to alter the laser cavity losses (see reference [1.51] for details). The first experimental Q-switching demonstrations were performed in 1962

by R.W. Hellwarth and F.J. McClung using actively electrically switched Kerr cell shutters in a ruby laser [1.53].

The passive method is generally simple and convenient and it requires a minimum of optical elements inside the laser. A passively Q-switched laser contains a saturable absorber instead of the modulator. The cavity losses are automatically modulated by the saturable absorber. The commonly used saturable absorbers are: semiconductor saturable absorber mirrors for passive Q-switching or mode locking of solid-state lasers [1.54], ion-doped crystals for passive Q-switching of solid-state lasers [1.55], and organic dye for passive Q-switching [1.56].

The output of the laser is not of a single, pure frequency or wavelength. All lasers produce light over some natural bandwidth of frequencies known as laser line width [1.57]. The range of frequencies that a laser may operate over is known as the gain bandwidth. In a laser cavity, the interference between the light itself generates cavity longitudinal modes. In a CW operated lasers, many of these modes will oscillate independently, with no fixed phase relationship between each other. The interference effects tend to average to a near-constant output intensity (CW output). If the phases of these modes are fixed, instead of constant output intensity, the modes of the laser will periodically all constructively interfere with one another, producing train of light pulses. Such a laser is said to be mode-locked or phase-locked. The larger the number of frequency components involved, the shorter the duration of the generated pulses can be.

Mode-locking can be obtained by active or passive methods. Active mode locking uses a variety of intracavity electro-optic or acousto-optic modulators. Passive mode-locking does not require external signal modulators. The modulation is performed automatically by the saturable absorber element or cell placed inside the laser cavity. As figure 1.12 shows, the fundamental passive

mode-locking methods are: slow saturable absorber mode-locking with a dynamic gain saturation [1.58], fast saturable absorber mode-locking [1.59], and soliton mode-locking [1.60].

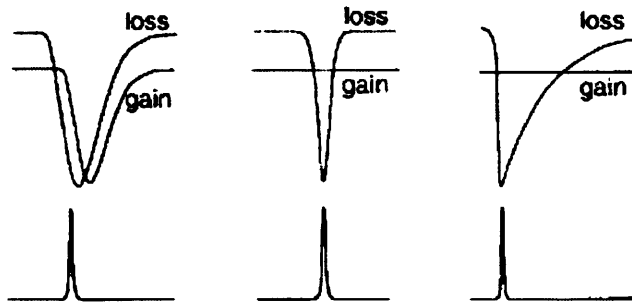


Figure 1.12 after ref [1.54]. The three fundamental passive mode-locking models: (a) passive mode-locking with a slow saturable absorber and dynamic gain saturation, (b) fast absorber mode-locking, and (c) soliton mode-locking

For solid-state laser mode locking mainly operates in the last two models, because no significant dynamic gain saturation is taking place. One successful example of mode locking using a faster absorber is the Kerr lens mode-locking [1.61], where strong self-focusing of the laser beam combined with either a hard aperture or a “soft” gain aperture is used to produce a self amplitude modulation, i.e., an equivalent fast saturable absorber [1.54].

## 1.7.2 Self-pulsation in semiconductor lasers

Self pulsation was seen in many types of gain-guided semiconductor lasers in the early laser development. It occurred after sufficient ageing or even under certain operating conditions [1.62], and was considered a nuisance. Controlled self-pulsation has however found use in CD laser sources to make the laser insensitive to optical feedback [1.63]. The mechanism of self pulsation is equivalent to passive Q switching. The self-regenerative process results from the optical feedback provided by the saturable absorber integrated within the laser device. As

discussed above, this configuration may also be used to passively mode lock the laser device. In either case, the laser will emit short pulses of light. Light pulses will have many frequency (wavelength) components when Fourier transformed. If the bandwidth of the laser pulse is sufficiently broad we can make the pulse duration very small. The saturable absorber can be integrated with the semiconductor laser in several different ways. The use of epitaxial absorbing layers in AlGaInP has been proposed [1.64], and the split-contact devices, where one section of the device is used as a saturable absorber, have become an attractive method for attaining self pulsation [1.65] [1.66] in semiconductor lasers. Devices based on QD structures are becoming of interest in the generation of ultra fast pulses, because of the spectral broadening associated with the distribution of dot sizes [1.67] [1.68]. These structures also exhibit ultrafast carrier dynamics [1.69] [1.70]. The presence of both fast carrier dynamics and broadband gain in QD structures facilitates the QD structure as a broadband gain medium and as a fast saturable absorber that allows the generation of broadband ultra short pulses. Recently, self-pulsation due to Q-switching and mode locking have both been demonstrated in quantum dot lasers using split-contact (or multi-section) design [1.66] [1.71].

In this work, multi section quantum dot lasers which have emission around 1  $\mu\text{m}$  have been fabricated and used to realise self pulsation. Self pulsation technique has used to broaden the emission spectra.

## 1.8 The aim of the thesis

The aim of the thesis is to study self-assembled quantum dot lasers as a broadband light source for  $\sim 1050$  nm OCT application and comparing it with other possible light sources. This includes finding dot material that emits at the  $\sim 1050$  nm region with broad bandwidth, realizing and examining self pulsation to broaden the output bandwidth and study the mechanism of broadening.

The ideal light source should be centred at  $\sim 1050$  nm with more than 70 nm bandwidth at FWHM. The power out of a single mode fibre should be at least 5-10 mW with less than 2 dB spectral modulation. The noise of the source should be lower than -90 dB [1.72].

## 1.9 Summary

In this chapter a brief introduction of OCT technology has been given. The importance of 1050 nm OCT and the available light sources at this region have been discussed. The basic principles of laser diode and quantum dots have been presented. Self pulsation technique has been introduced and proposed as a means of generating broadband emission.

## 1.10 References

- [1.1] Wolfgang Drexler, "Ultrahigh-resolution optical coherence tomography", *Journal of Biomedical Optics*, Vol. 9, No. 1, pp. 47-74, (2004).
- [1.2] A. F. Fercher, W. Drexler, C. K. Hitzenberger, and T. Lasser, "Optical coherence tomography – principles and applications", *Reports on progress in physics*, Vol. 66, No. 2, pp. 239-303, (2003).
- [1.3] D.Huang, E.A.Swanson, C.P.Lin, J.S.Schuman, W.G. Stinson, W. Chang, M.R. Hee, T. Flotte, K. Gregory, C.A. Puliafito, and J.G.Fujimoto, "Optical coherence tomography", *Science*, Vol. 254, pp. 1178-1181, (1991).
- [1.4] Guillermo J. Tearney, Mark E. Brezinski, Brett E. Bouma, Stephen A. Boppart, Costas Pitris, James F. Southern, and James G. Fujimoto, "In Vivo endoscopic optical biopsy with optical coherence tomography", *Science*, Vol. 276, pp. 2037-2039, (1997).
- [1.5] Adrian F Low, Guillermo J Tearney, Brett E Bouma and Ik-Kyung Jang,

- “Technology Insight: optical coherence tomography-current status and future development”, *Nature clinical practice*, Vol. 3, No. 3, pp. 154-162, (2006).
- [1.6] P. Singh, A. Chak, J. Willis, A. Rollins, M. Sivak and Jr. “In vivo optical coherence tomography imaging of the pancreatic and biliary ductal system”, *Gastrointestinal Endoscopy*, Vol. 62, No. 6, pp. 970-974, (2005).
- [1.7] J. Poneros, “Optical coherence tomography and the detection of dysplasia in Barrett's esophagus”, *Gastrointestinal Endoscopy*, Vol. 62, No. 6, pp. 832-833, (2005).
- [1.8] Bennett T. Amaechi, Adrian Podoleanu, Susan M. Higham, and David A. Jackson, “Correlation of quantitative light-induced fluorescence and optical coherence tomography applied for detection and quantification of early dental caries”, *Journal of Biomedical Optics*, Vol. 8, No. 4, pp. 642-647, (2003).
- [1.9] Jesse Weissman, Tom Hancewicz, and Peter Kaplan, “Optical coherence tomography of skin for measurement of epidermal thickness by shapelet-based image analysis”, *Optics Express*, Vol. 12, No. 23, pp. 5760-5769, (2004).
- [1.10] T. Seiler, “Magnetic resonance imaging of the eye and orbit”, in *Noninvasive Diagnostic Techniques in Ophthalmology*, B.R.Masters, Ed., pp. 17-31, Springer-Verlag, New York, (1990).
- [1.11] J. Powley, *Handbook of Biological Confocal Microscopy*, Plenum, New York, (1995).
- [1.12] J. Ambrose and J. Hounsfield, “Computerized transverse axial tomography”, *The British journal of radiology*, Vol.46, pp. 148-149, (1972).
- [1.13] M. Born and E. Wolf, *Principles of Optics: Electromagnetic Theory of Propagation, Interference and Diffraction of Light*, Cambridge Univer-

sity Press, Cambridge, 1999.

- [1.14] A.F.Fercher and E.Roth , “Ophthalmic laser interferometry”, *Proceedings SPIE*, Vol. 658, pp. 48-51, (1986).
- [1.15] A.F.Fercher, C.K.Hitzenberger, W.Drexler, G.Kamp, and H.Sattmann, “In vivo optical coherence tomography”, *American Journal of Ophthalmology*, Vol. 116, pp. 113-114, (1993).
- [1.16] A. F. Fercher, C. K. Hitzenberger, G. Kamp, S. Y. El-Zaiat, K. Seta, and B. K. Ward, “Measurement of intraocular distances by backscattering spectral interferometry: interferometric absolute distance measurement utilizing a mode-jump region of a laser diode”, *Optics communications*, 117, pp. 43-48, (1995).
- [1.17] G. Häusler and M. W. Lindner, “‘Coherence radar’ and ‘Spectral Radar’—new tools for dermatological diagnosis”, *Journal of biomedical optics*, Vol 3, No. 1, pp. 21-31, (1998).
- [1.18] R. Leitgeb, C. K. Hitzenberger, and A. F. Fercher, “Performance of Fourier domain vs. time domain optical coherence tomography”, *Optics express*, Vol. 11, No. 8, pp. 889-894, (2003).
- [1.19] R. A. Leitgeb, W. Drexler, A. Unterhuber, B. Hermann, T. Bajraszewski, T. Le, A. Stingl, and A. F. Fercher, “Ultrahigh resolution Fourier domain optical coherence tomography”, *Optics express*, Vol.12, No. 10, pp. 2156–2165, (2004).
- [1.20] M. Wojtkowski, V. J. Srinivasan, T. H. Ko, J. G. Fujimoto, A. Kowalczyk, and J. S. Duker, “Ultrahigh-resolution, high-speed, Fourier domain optical coherence tomography and methods for dispersion compensation”, *Optics express*, Vol. 12, No.11, pp. 2404–2422, (2004).
- [1.21] Boris Povazay, Boris Hermann, Angelika Unterhuber, Bernd Hofer, Harald Sattmann, Florian Zeiler, James E.Morgan, Christiane Falkner-Radier,

- Carl Glittenberg, Susanne Blinder, Wolfgang Dresler, “Three-dimensional optical coherence tomography at 1050nm versus 800nm in retinal pathologies: enhanced performance and choroidal penetration in cataract patients”, *Journal of Biomedical Optics*, Vol. 12 (4), (2007).
- [1.22] S.Muscat, S.Parks, E.Kemp, and D.Keating, “Repeatability and reproducibility of macular thickness measurements with the Humphrey OCT system”, *Investigative Ophthalmology & Visual Science*, Vol. 43, No. 2, pp. 490-495, (2002).
- [1.23] C.Sanchez-Galeana, C.Bowd, E.Z.Blumenthal, P.A.Gokhale, L.M.Zangwill, and R.N.Weinreb, “Using optical imaging summary data to detect glaucoma”, *Ophthalmology*, Vol. 108, No. 10, pp. 1812-1818, (2001).
- [1.24] P.Massin, C.Allouch, B.Haouchine et al., “Optical coherence tomography of idiopathic macular epiretinal membranes before and after surgery”, *American Journal of Ophthalmology*, Vol. 130, No. 6, pp. 732-739, (2000).
- [1.25] A.Unterhuber, B.Povazay, B.Hermann, H.Sattmann, A.Chavez-Pirson, and W.Drexler, “In vivo retinal optical coherence tomography at 1040nm-enhanced penetration into the choroids”, *Optics express*, Vol. 13, No. 9, (2005).
- [1.26] M.Hammer, A.Roggan, D.Schweitzer and G.Muller, “Optical properties of ocular fundus tissues-an in vitro study using the double-integrating-sphere technique and inverse Monte Carlo Simulation”, *Physics in Medicine and Biology*, Vol. 40, pp. 963-978, (1995).
- [1.27] American National Standards Institute, “American National Standard for Safe Use of Lasers”, ANSI Z 136-1, (2000).

- [1.28] International Commission of Non-Ionizing Radiation Protection, "Revision of guidelines on limits of exposure to laser radiation of wavelengths between 400nm and 1.4 $\mu$ m", *Health Physics*, Vol. 79, No. 4, pp. 431-440, (2000).
- [1.29] B. Považay, K. Bizheva, B. Hermann, A. Unterhuber, H. Sattmann, A.F. Fercher, W. Drexler, C. Schubert, P.K. Ahnelt, M. Mei, R. Holzwarth, W. J. Wadsworth, J.C. Knight, and P. St. J. Russel, "Enhanced visualization of choroidal vessels using ultrahigh resolution ophthalmic OCT at 1050 nm", *Optics express*, Vol. 11, No. 17, (2003).
- [1.30] G.M.Hale, and M.R.Querry, "Optical constants of water in the 200 nm to 200  $\mu$ m wavelength region", *Applied Optics*, Vol.12, No.3, pp. 555-563 (1973).
- [1.31] A. Unterhuber, B.Povazy, B.hermann, H.Sattmann,W.Drexler, V.Yakovlev, G.Tempea, C.Schubert, E.M.Anger, P.K.Ahnelt, M.Stur, J.E.Morgan, A.Cowey, G.Jung, T.Le, and A.Stingl, "Compact, low-cost Ti:Al<sub>2</sub>O<sub>3</sub> laser for in vivo ultrahigh-resolution optical coherence tomography", *Optics letters*, Vol. 28, No. 11, pp. 905-907, (2003).
- [1.32] Ursula Schmidt-Erfurth, Rainer A.Leitgeb, Stepban Michels, Boris Povazay, Stefan Sacu, Boris Hermann, Cbristian Ablers, Harald Sattmann, Christoph Scholda, Adold F.Fercher, and Wolfgang Drexler, " Three-Dimensional Ultrahigh-Resolution Optical Coherence Tomography of Macular Diseases", *Investigative Ophthalmology & Visual Science*, Vol. 46, No. 9, pp. 3393-3402, (2005).
- [1.33] Birks T A , Wadsworth.W. J and Russel. P.St, "Supercontinuum generation in tapered fibers", *Optics letters*, Vol. 25, No. 19, pp. 1415-1417, (2000).
- [1.34] Newbury.N.R, Washburn.B.R, Windeler.R.S, and Corwin.K.L, "Noise amplification during supercontinuum generation in microstructure fiber",

*Optics letters*, Vol. 28, No. 11, pp. 944-946, (2003).

- [1.35] K.L. Corwin, N.R. Newbury, J.M. Dudley, S. Coen, S.A. Diddams, K. Weber, R.S. Windeler, "Fundamental noise limitations to supercontinuum generation in microstructure fiber", *Physical review letters*, Vol. 90, No. 11, (2003).
- [1.36] Barry Cense, Nader A. Nassif, Teresa C. Chen, Mark C. Pierce, Seok-Hyun Yun, B. Hyle Park, Brett E. Bouma, Guillermo J. Tearney, Johannes F. de Boer, "Ultrahigh-resolution high-speed retinal imaging using spectral-domain optical coherence tomography", *Optics express*, Vol. 12, No. 11, pp. 2435-2447, (2004).
- [1.37] Tony H. Ko, Desmond C. Adler, James G. Fujimoto, Dmitry Mamedov, Viatcheslav Prokhorov, Vladimir Shidlovski, and Sergei Yakubovich, "Ultrahigh resolution optical coherence tomography imaging with a broadband superluminescent diode light source", *Optics express*, Vol. 12, No. 10, pp. 2112-2119, (2004).
- [1.38] H.S. Djie and B.S. Ooi, X.-M. Fang, Y. Wu, J. M. Fastenau, W. K. Liu, and M. Hopkinson, "Room-temperature broadband emission of an InGaAs/GaAs quantum dots laser", *Optics letters*, Vol. 32, No. 1, pp. 44-46, (2007).
- [1.39] A. Kovsh, I. Krestnikov, D. Livshits, S. Mikhlin, and J. Weimert, "Quantum dot laser with 75 nm broad spectrum of emission", *Optics letter*, Vol. 32, No. 7, pp. 793-795, (2007).
- [1.40] Einstein A, "On the Quantum theory of radiation", *Physikalische Zeitschrift*, Vol. 18, No. 121, (1917). Translated in: Haar D T, "The old quantum theory", *Pergamon Press*, (1967).
- [1.41] Coldren, L.A. and Corzine, S.W., *Diode Lasers and Photonic Integrated Circuits*, Wiley Series in Microwave and Optical Engineering, John

- Wiley and Sons, p.113, (1995).
- [1.42] MA Herman, H Sitter, *Molecular Beam Epitaxy: Fundamentals and Current Status*, Springer-Verlag, (1989).
- [1.43] Mukai, K., Ohtsuka, N., Sugawara, M., and Yamazaki, S., “ Self-formed  $\text{In}_{0.5}\text{Ga}_{0.5}\text{As}$  quantum dots on GaAs substrates emitting at  $1.3 \mu\text{m}$ ”, *Japanese journal of applied physics*, Vol. 33, pp. L1710-L1712, (1994).
- [1.44] Gerald B. Stringfellow, *Organometallic vapor-phase epitaxy: theory and practice*, 2<sup>nd</sup> edition, *Academic Press*, (1999).
- [1.45] C. Ratsch and A. Zangwill, “ Equilibrium theory of the Stran-ski-Krastanov epitaxial morphology”, *Surface science*, Vol.293, pp. 123-131, (1993).
- [1.46] T.Walther, A.G.Cullis, D.J.Norris, and M.Hopkinson, “Nature of the Stran-ski-Krastanow Transition during expitaxy of InGaAs on GaAs”, *Physical review letters*, Vol. 86, No. 11, pp. 2381-2384, (2001).
- [1.47] Mitsuru Sugawara, “Theoretical bases of the optical properties of semi-conductor quantum nano-structures”, in *Semiconductors and semimetals*, Vol. 60, Ed. Mitsuru Sugawara, London, Academic press, p.5., (1999)
- [1.48] Peter Blood, postgraduate lecture notes, Cardiff university, (2007).
- [1.49] Mowbray D J, Skolnick M S, “New physics and devices based on self-assembled semiconductor quantum dots”, *Journal of Physics D: Applied Physics*, Vol. 38, No. 13, pp. 2059-2076, (2005).
- [1.50] Ustinov V M, Zhukov A E, Egorov A Y, Maleev N A, *Quantum dot lasers*, Oxford, Oxford university press, (2003).
- [1.51] Siegman A E, *Lasers*, University Science Books, (1986).
- [1.52] Borri P, Langbein W, Schneider S, Woggon U, Sellin R L, Ouyang D, and Bimberg D, “Ultralong Dephasing Time in InGaAs Quantum Dots”, *Physical Review Letters*, Vol. 87, No. 15, 157401 (2001).

- [1.53] F. J. McClung and R. W. Hellwarth, “Giant optical pulsations from ruby”, *Journal of applied physics*, Vol. 33, No. 3, pp. 828 -830, (1962).
- [1.54] Ursula Keller, Kurt J. Weingarten, Franz X. Kartner, Daniel Kopf, Bernd Braun, Isabella D. Jung, Regula Fluck, Clemens Honninger, Nicolai Matuscheck, and Juerg Aus der Au, “Semiconductor saturable absorber mirrors (SESAMs) for femtosecond to nanosecond pulse generation in solid-state lasers”, *IEEE Journal of selected topics in quantum electronics*, Vol. 2, No. 3, pp. 435- 453, (1996).
- [1.55] Heiko Ridderbusch and Thomas Graf, “Saturation of 1047- and 1064-nm absorption in Cr<sup>4+</sup>:YAG crystals”, *IEEE Journal of Quantum Electronics*, Vol. 43, No. 2, pp.168 – 173, (2007).
- [1.56] J. Katzenstein, G. Magyar and A. C. Selden, “Laser Q-switching by organic solvents”, *Optical and Quantum Electronics*, Vol. 1, No. 1, pp. 13-19, (1969).
- [1.57] A. L. Schawlow and C. H. Townes, “Infrared and optical masers”, *Physical review*, Vol. 112, No. 6, pp 1940 -1949, (1958).
- [1.58] Hermann A. Haus, “Theory of mode locking with a slow saturable absorber” *IEEE Journal of Quantum Electronics*, Vol. 11, No. 9, pp. 736–746, (1975).
- [1.59] Hermann A. Haus, “Theory of modelocking with a fast saturable absorber”, *Journal of Applied Physics*, Vol. 46, No. 7, pp 3049 -3059, (1975).
- [1.60] F. X. Kartner, I. D. Jung, and U. Keller, “Soliton mode-locking with saturable absorbers”, *IEEE Journal of selected topics in quantum electronics*, Vol. 2, No. 3, pp. 540–556, (1996).
- [1.61] U. Keller, G. W. 'tHooft, W. H. Knox, and J. E. Cunningham, “Femto-second pulses from a continuously self-starting passively mode-locked

- Ti:sapphire laser”, *Optics letters*, Vol. 16, No.13, pp. 1022–1024, (1991).
- [1.62] Thomas L. Paoli, “Changes in the Optical properties of CW (AlGa)As Junction Lasers during Accelerated Ageing”, *IEEE journal of Quantum Electronics*, Vol.13, No. 5, pp.351 - 355, (1977).
- [1.63] S. Matsui, H. Takiguchi, H. Hayashi, S. Yamamoto, S. Yano, and T. Hijikata, “Suppression of feedback-induced noise in short-cavity V-channeled substrate inner stripe lasers with self-oscillation”, *Applied physics letter*, Vol. 43, No. 3, pp. 219 - 221, (1983).
- [1.64] H. D. Summers, C.H. Molloy, P. M. Snowton, P. Rees, I. Pierce, “Experimental Analysis of Self-pulsation in 650 nm wavelength AlGaInP Laser Diodes with Epitaxial Absorbing Layers”, *IEEE Selected Topics in Quantum Electronics*, Vol 5, No. 3, pp.745 – 749, (1999).
- [1.65] Dennis J. Derickson, Roger J. Helkey, Alan Mar, Judy R. Karin, John G. Wasserbauer, and John E. Bowers, “ Short Pulse Generation using Multisegment Mode-locked Semiconductor Lasers”, *IEEE Journal of Quantum Electronics*, Vol 28, No. 10, pp.2186 – 2201, (1992).
- [1.66] E. U. Rafailov, M. A. Cataluna, W. Sibbett, N. D. Inskaya, Yu. M. Zadiranov, A. E. Zhukov, V. M. Ustinov, D. A. Livshits, A . R. Kovsh, and N. N. Ledentsov, “High-power picosecond and femtosecond pulse generation from a two-section mode-locked quantum-dot laser”, *Applied Physics Letters*, Vol. 87, 081107, (2005).
- [1.67] P.Borri, W.Langbein, J.M.Hvam, F.Heinrichsdorff, M.-H.Mao, D.Bimberg, “Spectral hole-burning and carrier-heating dynamics in InGaAs quantum-dot amplifiers”, *IEEE Journal of selected topics in quantum electronics*, Vol. 6, No. 3, pp. 544 - 551, (2000).
- [1.68] E.U.Rafailov, P.Loza-Alvarez, W.Sibbett, G.S.Sokolovskii, D.A.Livshits, A.E.Zhukov, V.M.Ustinov, “Amplification of femtosecond pulses over by

- 18 dB in quantum dot semiconductor optical amplifier”, *IEEE Photonics technology letters*, Vol. 15, No. 8, pp. 1023 - 1025, (2003).
- [1.69] P. Borri , W. Langbein, J. M. Hvam, M.-H. Mao, F. Heinrichsdorff, and D. Bimberg, “Ultrafast gain and index dynamics in InGaAs quantum dot amplifiers”, *IEEE Photonics technology letters*, Vol. 12, No. 6, pp 594 -596, (2000).
- [1.70] E.U.Rafailov, E.U. Rafailov, S.J. White, A.A. Lagatsky, A. Miller, W. Sibbett , D.A. Livshits , A.E. Zhukov, and V.M. Ustinov, “Fast quantum-dot saturable absorber for passive mode-locking of solid-state lasers”, *IEEE photonics technology letters*, Vol. 16, No. 11, pp. 2439-2441, (2004).
- [1.71] Huw D.Summers, Daniel R. Matthews, Peter M. Snowton, Paul Rees, and Mark Hopkinson, “Laser dynamics in self-pulsating quantum dot systems”, *Journal of applied physics*, Vol. 95, No. 3, pp. 1036-1041, (2004).
- [1.72] James Fergusson, “Understanding, developing and characterizing quantum dot lasers for use in 1050nm optical coherence tomography”, MSc thesis, Cardiff University, (2007).

# Chapter 2 Experimental techniques

## 2.1 Introduction

As discussed in chapter 1, the central lasing wavelength is critical for the OCT application. In this chapter, details of the selected quantum dot materials which emit at around 1  $\mu\text{m}$  region are presented. The examined devices including stripe lasers, ridge waveguide lasers and multisection devices are introduced. Experimental setups for measuring such as optical spectra, optical power, modal gain and etc have been described.

## 2.2 Material description

All the quantum dot materials studied in this project were InGaAs/GaAs multi layer quantum dot based structures. These materials were designed for emissions around the 1  $\mu\text{m}$  region. The materials were fabricated by the EPSRC National Centre for III-V Technologies at Sheffield University. Four different dot wafer designs have been studied during the project. The materials studied namely M1961, M1963, M1964 and M1965 are described below.

The active region of wafer M1961 consists of seven layers of InGaAs quantum dots layers capped with GaAs layers and separated by  $\text{Al}_{0.15}\text{Ga}_{0.85}\text{As}$  barriers (see Table 2.1). The cladding layers are p and n doped  $\text{Al}_{0.15}\text{Ga}_{0.85}\text{As}$ . The contact layer is p doped GaAs and the buffer layer is n doped GaAs.

Repeats	Thickness(A)	Material	Dopant
1	3000	GaAs	Beryllium
1	12000	$Al_{0.5}Ga_{0.5}As$	Beryllium
1	430	$Al_{0.15}Ga_{0.85}As$	
x 7	70	$Al_{0.15}Ga_{0.85}As$	
	50	GaAs	
	21	InGaAs-7ML	
	50	GaAs	
1	500	$Al_{0.15}Ga_{0.85}As$	
1	12000	$Al_{0.5}Ga_{0.5}As$	Silicon
1	5000	GaAs	Silicon

Table 2.1 M1961 quantum dot wafer layer structure

Repeats	Thickness(A)	Material	Dopant
1	3000	GaAs	Beryllium
1	12000	$Al_{0.5}Ga_{0.5}As$	Beryllium
1	430	$Al_{0.15}Ga_{0.85}As$	
1	70	GaAs	
x 5	21	InGaAs-7ML	
	70	GaAs	
1	500	$Al_{0.15}Ga_{0.85}As$	
1	12000	$Al_{0.5}Ga_{0.5}As$	Silicon
1	5000	GaAs	Silicon

Table 2.2 M1963 quantum dot wafer layer structure

The active region of wafer M1963 consists of five repeat layers of InGaAs quantum dot layers capped with GaAs layers (see Table 2.2). These are sandwiched by  $\text{Al}_x\text{Ga}_{1-x}\text{As}$  barrier. The contact and buffer layer are p and n doped GaAs. These dot layers are closely stacked InGaAs/GaAs multi layer quantum dots [2.1]. Each InGaAs dots layer is separated by a thin (7nm) GaAs intermediate layer. Because the barrier layer between each dot layer is very thin, the upper layer of dots may self-align just on the lower layer of dots. The perpendicular alignment of dots is due to the strain fields induced by the lower layer of dots. An analytical description of the correlated dot formation in the growth direction under strain fields has been provided by reference [2.2]. The dots will perpendicularly align when the intermediate GaAs layer thickness is below a critical intermediate layer thickness (i.e.  $< 10\text{nm}$ ). The alignment of dots in the perpendicular direction will make it possible to couple the dots electrically in the vertical direction as the intermediate GaAs thickness is reduced to the extent that the electron wave functions of the neighbouring dots are overlapped. A schematic of the profiles of the band gap energy and the corresponding refractive index of the laser made from this material is shown in figure 2.1.

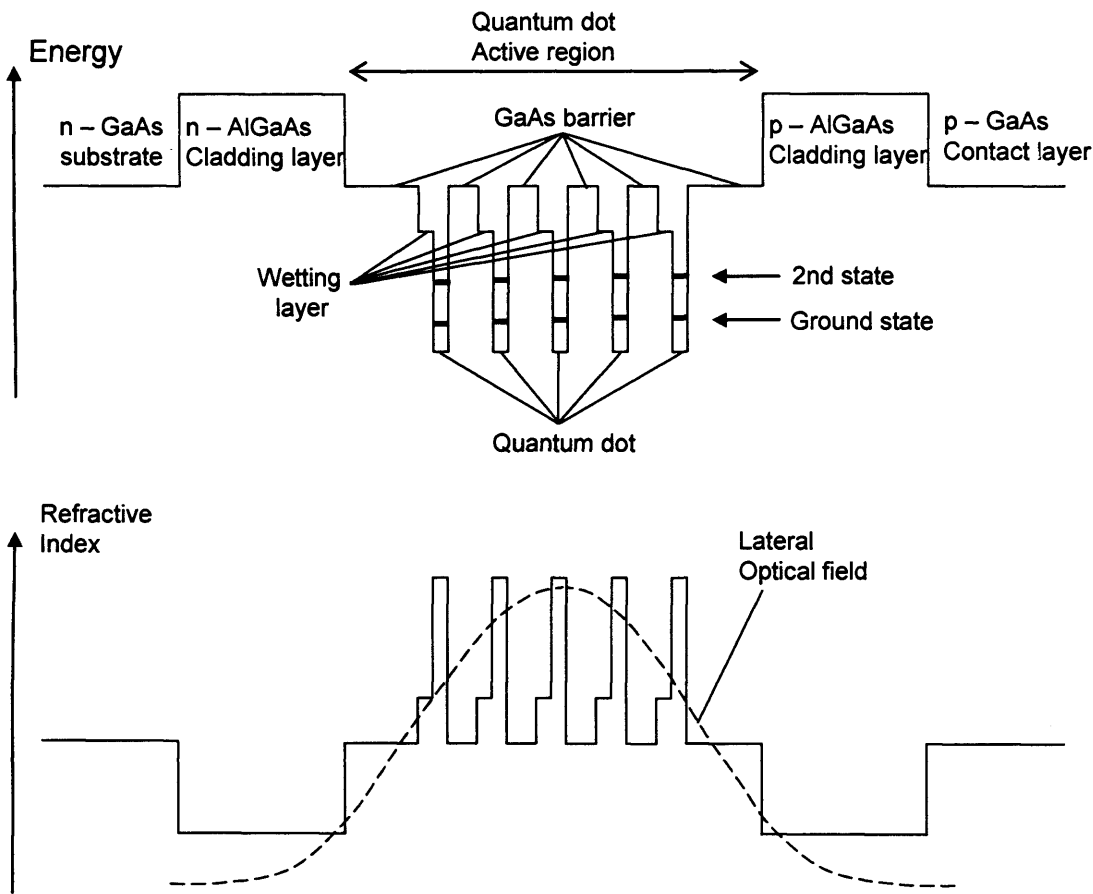


Figure 2.1 Schematic of M1963 quantum dot laser

Each quantum dot layer (undoped) is surrounded by a pair of higher band gap barriers (undoped) to effectively confine injected carriers. The active region is sandwiched by cladding layers (doped) with a higher band gap energy (smaller refractive index), resulting in the formation of an optical waveguide. Thus, the structure is similar to that of conventional double heterostructure lasers.

The wafer M1964 has similar structure to M1963 but the active region contains seven repeat layers of InGaAs quantum dots layers capped with GaAs layers (see Table 2.3).

Repeats	Thickness(A)	Material	Dopant
1	3000	GaAs	Beryllium
1	12000	$Al_{0.5}Ga_{0.5}As$	Beryllium
1	430	$Al_{0.15}Ga_{0.85}As$	
1	70	GaAs	
x 7	21	InGaAs-7ML	
	70	GaAs	
1	500	$Al_{0.15}Ga_{0.85}As$	
1	12000	$Al_{0.5}Ga_{0.5}As$	Silicon
1	5000	GaAs	Silicon

Table 2.3 M1964 quantum dot wafer layer structure

Repeats	Thickness(A)	Material
1	3000	GaAs
1	12000	$Al_{0.6}Ga_{0.4}As$
1	930	$Al_{0.15}Ga_{0.85}As$
x 3	70	$Al_{0.15}Ga_{0.85}As$
	21	InGaAs-7ML
1	1000	$Al_{0.15}Ga_{0.85}As$
1	12000	$Al_{0.6}Ga_{0.4}As$
1	5000	GaAs

Table 2.4 M1965 quantum dot wafer layer structure

The active region of wafer M1965 consists of three repeat layers of InGaAs quantum dots layers capped with  $\text{Al}_{0.15}\text{Ga}_{0.85}\text{As}$  layers (see Table 2.4). These are sandwiched by  $\text{Al}_x\text{Ga}_{1-x}\text{As}$  barrier. The contact and buffer layer are p and n doped GaAs.

## 2.3 The devices

### 2.3.1 Stripe laser

The materials have been processed to make stripe laser diodes. The oxide film is deposited over the material surface, and then the oxide from centre of the structure is removed to leave a 50  $\mu\text{m}$  stripe of semiconductor to which a metal contact can be applied. This is achieved by using photoresist and wet etching. After that, the photoresist is removed and a Au-Zn layer is thermally evaporated and then annealed to make the p-type ohmic contact. The ohmic contact is only made along the 50  $\mu\text{m}$  stripe. The sample is then thinned by lapping and polishing the piece of semiconductor. Finally, a Au-Ge-Ni-Au metal layer is thermally evaporated and annealed to form the n-type contact. The device processing was performed by the trained staff in the cleanroom at Cardiff University. A schematic diagram of a typical oxide stripe laser is shown in Figure 2.2.

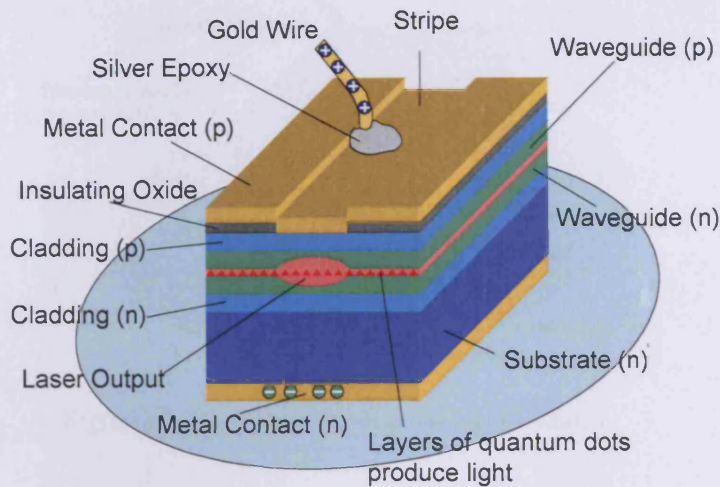


Figure 2.2 Schematic of an oxide stripe laser

This type of laser diode is a gain guided device. In the vertical direction, the generated light is guided by the different refractive index step between the different layers. In the horizontal direction, the light is controlled by the presence of gain realized by localized pumping in the  $50\ \mu\text{m}$  stripe area. After the fabrication process, wafers were cleaved to different length chips: 0.5 mm, 1 mm and 2 mm. Chips then were mounted to a header and connected to gold wires to form practical laser diodes.

### 2.3.2 Ridge waveguide laser

OCT application requires single transverse mode light source and the ridge-waveguide geometry is expected to offer better optical and current confinement as well as improved heat dissipation. In order to have single transverse mode output, we have fabricated ridge-waveguide lasers using material M1963. The ridge devices of width  $2\ \mu\text{m}$  and height  $1.54\ \mu\text{m}$  were fabricated. A schematic diagram of a typical ridge laser is shown in Figure 2.3.

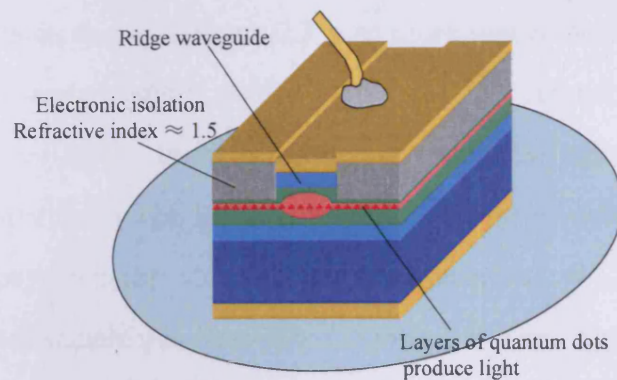


Figure 2.3 Schematic of a ridge waveguide laser

A brief description of the fabrication process is provided as follows. The positive e-beam resist is first spun on to the sample, and then the ridge pattern is written by electronic beam lithography. The resist of the exposed ridge part is removed by the developer and the unexposed part remains. The sample is then deposited with a Ni film, and this is followed by removing the unwanted resist and Ni. This is achieved by immersing the sample into a bath of hot acetone, so the resist dissolves and concomitantly the Ni lifted-off. After this process, the Ni is used as an etching mask for ridge pattern. The ridge is formed by inductively coupled plasma (ICP) etching. This process involves physical ion bombardment and chemical reactions to remove the unmasked material. A balance of these processes will provide a good (vertical and smooth) sidewall profile. The Ni mask is removed after the etching and an electronically insulating material (Benzocyclobutene) is spun on. The insulating layer is then etched back to expose the top surface of the ridge. After that, an Au-Zn layer is thermally evaporated and then annealed to make the p-type ohmic contact. The ohmic contact is only made along the top surface of the ridge. The sample is then thinned by lapping and polishing the piece of semiconductor. Finally, an Au-Ge-Ni-Au metal layer is thermally evaporated and annealed to form the n-type contact. The devices were processed by the trained staff in the cleanroom at Cardiff University.

The laser diode shown in figure 2.3 is an index guided device. In the vertical direction, the generated light is guided by the different refractive index step between the different layers. In the horizontal direction, the light is guided by the different refractive index step between the ridge and the electronically insulating material (Benzocyclobutene which has a refractive index  $\approx 1.5$ ). After processing, the fabricated sample was cleaved to 0.5 mm, 1 mm and 2 mm long chips.

### 2.3.3 The multisection devices

The multisection device (segmented p-type contact) can be used to measure modal gain/loss. It can also be configured to perform self pulsation. The stripe/ridge device can be patterned with segmented p-type contact. This is achieved by using photolithography/e-beam lithography and wet etching. The photoresist/e-beam resist is spun on the top surface. The pattern of the intersection breaks are defined in the resist by either using a photomask or e-beam lithography. The patterned resist is then used as a wet etching mask. The top contact metal is etched to form the segmented p-type contact. Finally the residual resist is removed to leave the top segmented p-type contact clear for wire bonding. The device processing was performed by the trained staff in the cleanroom at Cardiff University. A schematic diagram of the multisection device for gain/absorption measurement is shown in figure 2.4.

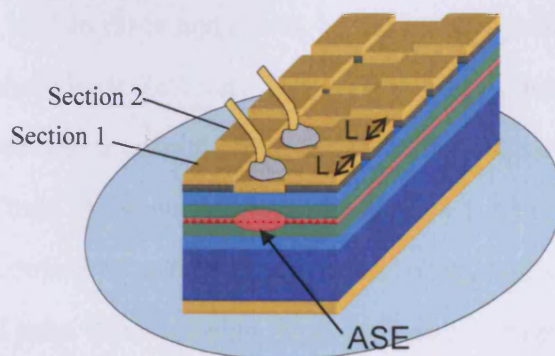


Figure 2.4 A schematic of a multisection device for gain/loss measurement

## 2.4 Light-current measurements

In order to investigate the properties of the laser diode, the Light-Current (L-I) characteristics have to be investigated. The current-voltage-light (IVL) measurement is performed using a pulsed driven current to avoid any self heating effects. The pulses are typically 1  $\mu$ s in duration and occur at a rate of 5 kHz. For the pulsed measurement, the data is obtained using the setup shown in figure 2.5.

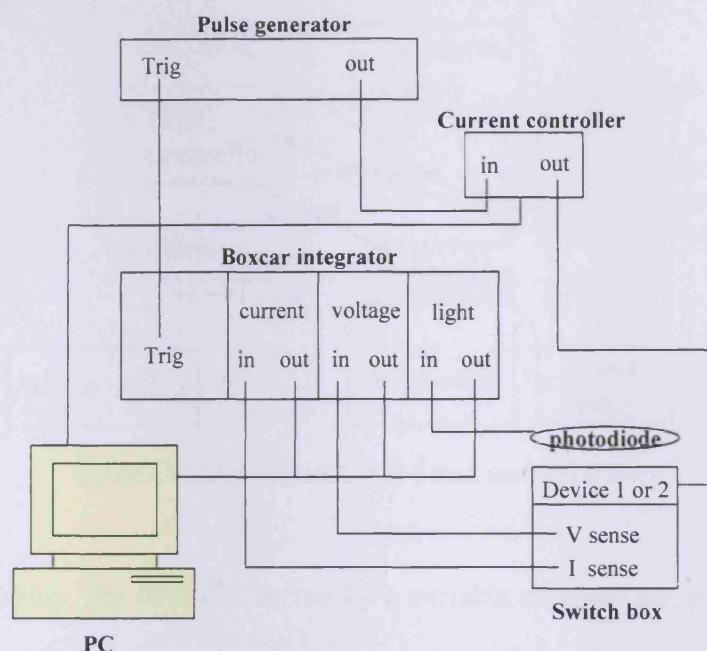


Figure 2.5 Schematic of pulsed IVL measurement system

The device is held in place and driven by the current pulse. The emitted light is detected by a photodiode detector. The current pulses produced by the pulse generator are passed into a current controller, which is controlled by a computer allowing the amplitude of the current pulse to be varied. The voltage, current and light signals are acquired by a PC via the boxcar integrator, which integrates the signal over a fixed time window using triggered gates. Using this setup, the current/voltage and the current/light characteristics of the device can be measured

under pulsed conditions.

For OCT applications, an ideal device should be operated under continuous drive current condition. This requires a constant drive current through the device. The L-I may be different to that obtained using the pulsed condition due to the heating effect. In order to measure the L-I under continuous drive current, a different setup has been built (See figure 2.6).

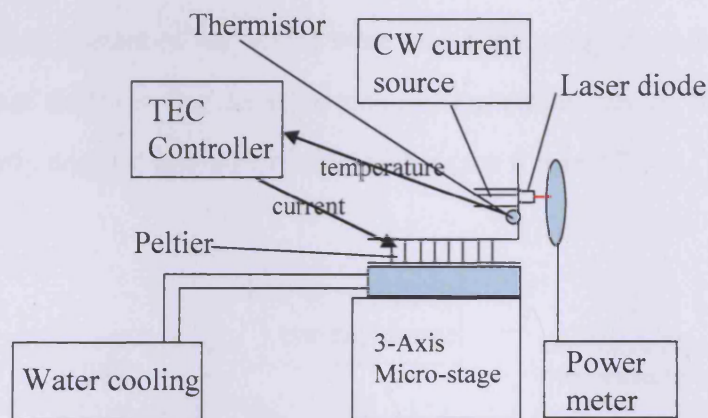


Figure 2.6 Schematic of CW L-I measurement system

In this setup, the device is driven by a variable constant current source. The device is mounted on the sub-mount to be constantly cooled. The sub-mount is cooled by a Peltier (thermal electric cooler: TEC). The hot side of the Peltier is then cooled by a water cooled heat sink. A thermistor placed close to the device senses the instantaneous temperature and provides feedback to the TEC controller and the controller then varies the current applied to the Peltier. Thus, the device can be operated at a relatively fixed temperature under continuous drive current. The current is manually changed and the output power is measured by a power meter.

## 2.5 Far field measurement

The far field of the light output of the device was measured by placing the laser diode at the centre of a rotating stage and the detector  $\sim 10$  cm from the laser. By taking measurement at each angle, an intensity profile vs angle can be plotted.

## 2.6 Spectra measurements

The lasing spectra of the device were measured using an Ando AQ6317 optical spectrum analyzer. For the wide area ( $50 \mu\text{m}$  stripe) device, the output light can be directly coupled into a multi-mode fibre (see figure 2.7).

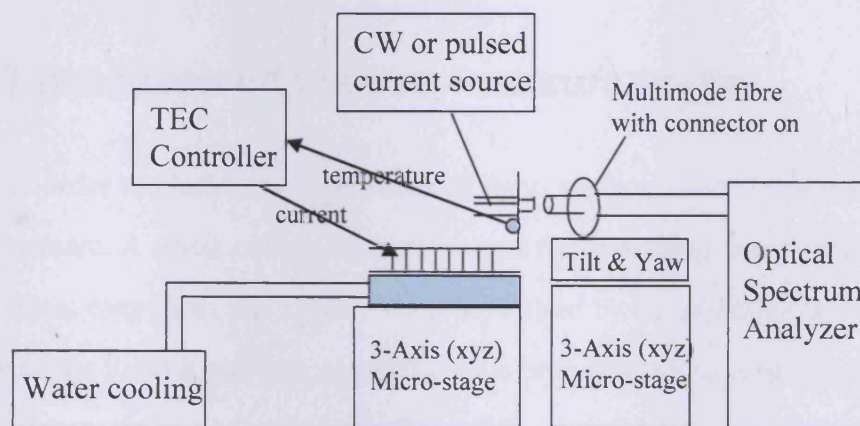


Figure 2.7 Schematic of spectra measurement for wide area device

The cooling setup described above allows the device to be operated at a set temperature. The multi-mode fibre is mounted on a 5-directional micro stage (3-axis plus tilt and yaw).

For the ridge waveguide device, the output light is coupled into the spectrum analyzer by using a lensed single mode fibre. Because the aperture of the ridge ( $2 \mu\text{m}$ ) and the single mode fibre core is very small, a microscope was used for coupling. A schematic of the setup is shown in figure 2.8.

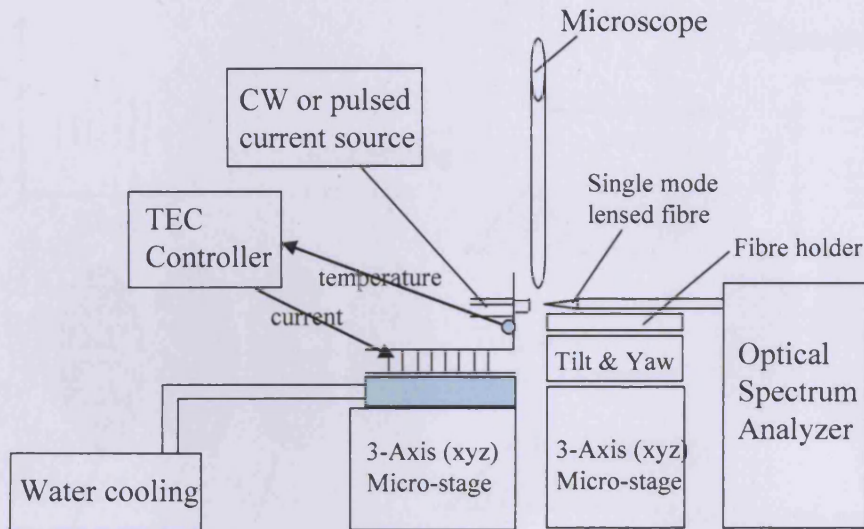


Figure 2.8 Schematic of spectra measurement for ridge waveguide device

## 2.7 Time-resolved spectra measurements

In order to observe the fast pulses of light, we examined the devices with a streak camera. A streak camera is an instrument for measuring fast variation of the input signal over time. The measurement is realised by transforming the temporal profile of the input signal into a spatial profile on a detector. A schematic of a basic streak camera system is shown in figure 2.9.

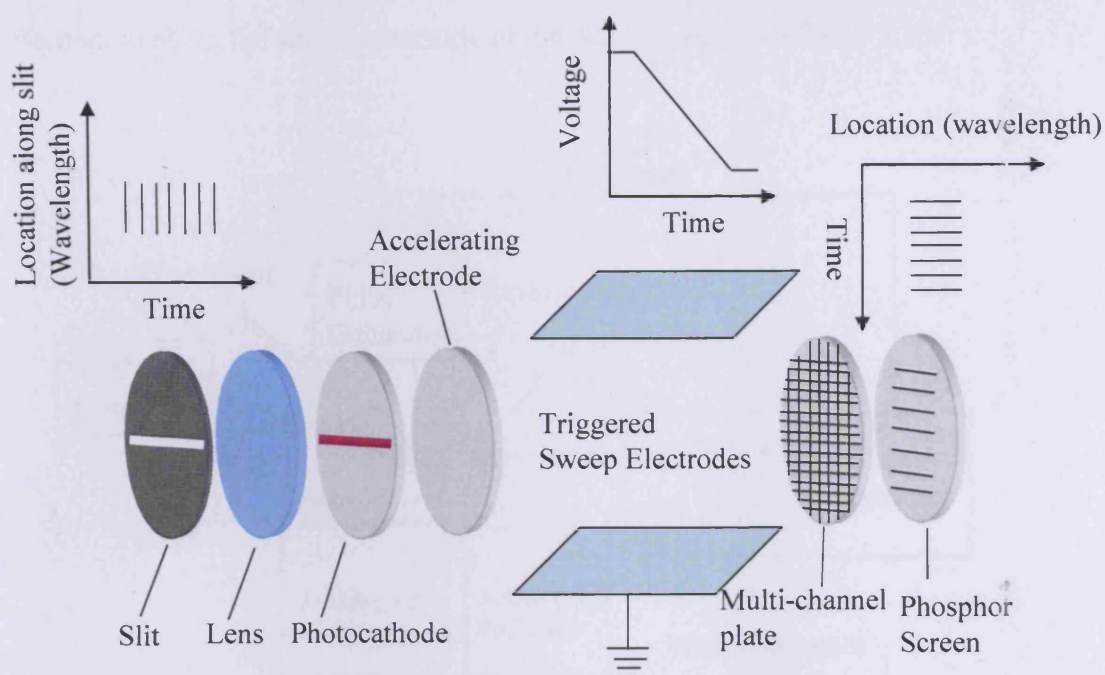


Figure 2.9 Schematic of a streak camera's principle

The light enters through a slit and is focused on the photocathode, the corresponding photoelectrons generated by the photocathode are accelerated by the accelerating electrode then pass between the pair of triggered sweep electrodes, the applied sweep voltage steers the electron paths away from the horizontal direction at different angles, depending upon their arrival time at the electrodes. The amplified electrons reach the phosphor screen and form an image oriented in the vertical direction according to the arrival time at the sweep electrodes. The earliest pulse is arranged in the uppermost position and the latest pulse is in the bottom most portion of the phosphor image. The resulting streak image has location as one axis and time as another axis.

In order to observe the self pulsation and the spectral information at the same time the streak camera is operated in conjunction with a 0.3 m spectrometer that provides spectral information with a bandwidth of 27 nm. The output of the spectrometer is aligned to the input slit of the streak camera. This provides wavelength

information along the slit. A schematic of the setup is shown in figure 2.10.

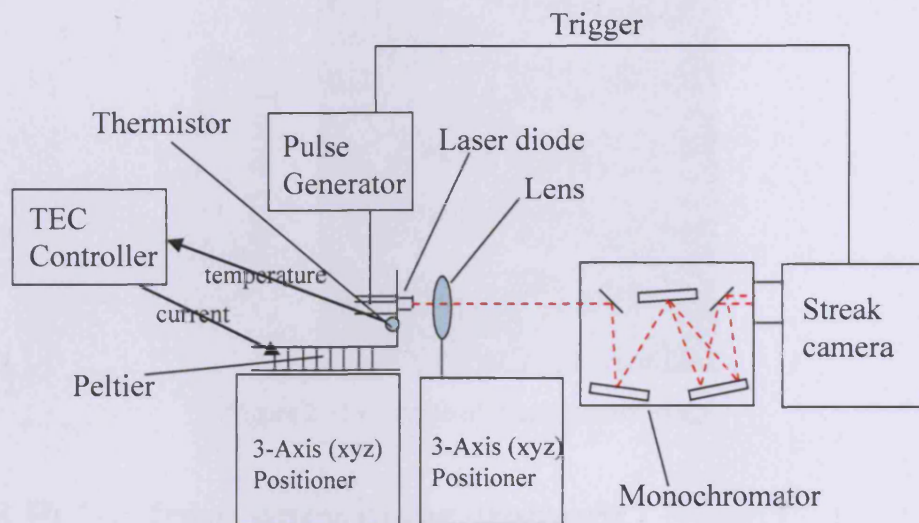


Figure 2.10 Schematic of time resolved spectra measurement

To facilitate this, the lasers are driven pulsed with a current source at a frequency of 5 kHz and a pulse length of 1  $\mu\text{s}$ . This provides an injection regime of sufficient duration for the carrier-photon dynamics to evolve beyond the transients induced by the pulse turn-on and to establish repetitive pulsation. The pulse generator triggers the streak camera system. By using this method, we can observe the pulsation and optical spectrum at the same time. An example of the measurement is shown in figure 2.11. The horizontal axis represents wavelength while the vertical axis represents time. The relative density is shown by the colour where blue represents a low intensity while red represents a high intensity of light. The wavelength resolution is  $\sim 0.04$  nm, and the time resolution is  $\sim 8$  ps in a 5 ns time window.

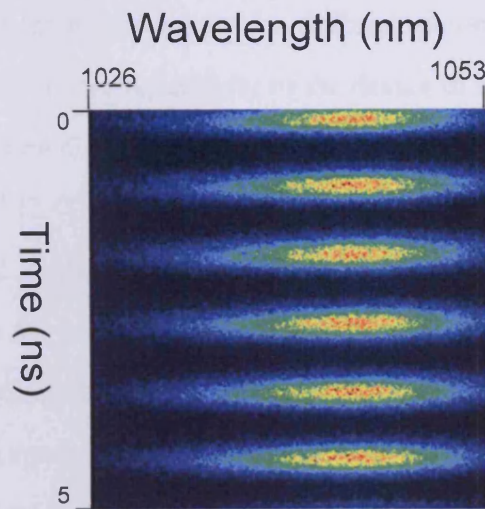


Figure 2.11 Example of streak camera image

## 2.8 Pulse frequency measurement

An electronic spectrum analyzer (FSP30 from Rhode and Schwarz) was used with a high speed photodetector (model 1437 from New focus) to measure the frequency of the light pulses from the self pulsed device. The frequency range that the spectrum analyzer can detect is 9 kHz – 30 GHz. The wavelength the photodetector can detect is 400 nm – 1650 nm. Because the size of the photodetector is very small (25  $\mu\text{m}$  diameter), the light output from the self pulsed device was aligned to the photodetector using two lenses. By varying the operating parameters such as the driving current or the temperature, a change of the self pulsation frequency was recorded.

## 2.9 The segmented contact method

There are a few methods that can be used for experimentally studying the gain of a laser diode lasing material. The conventional method described in [2.3] also known as “threshold current as a function of cavity length” can be performed quickly to get information about the peak gain/current relationship. However this

method requires identical mirror losses for different device lengths. It also requires knowledge of the mirror reflectivity of the device in advance. Furthermore, it can not provide information on the gain spectrum. Another method known as “Hakki-Paoli method” [2.4] obtains the net modal gain by comparing the longitudinal modes observed in the end emission of a laser structure below threshold. This method requires very high resolution spectra and it can only measure the gain spectrum for currents below the threshold. One may also measure the true spontaneous emission spectrum to calculate the gain spectrum [2.5, 2.6]. However, this assumes the carriers in the gain medium are in quasi equilibrium defined by Fermi Dirac statistics. It also requires that the spontaneous emission spectrum is measured in real units. Single pass techniques have the advantages of being independent of round trip amplification or laser action and amplification during transmission through a known length of the gain medium. Shaklee and Leheny [2.7] proposed a variable stripe method where different lengths of stripes were optically pumped. By measuring the single pass amplified spontaneous emission (ASE) from different lengths of stripes, the gain spectrum may be found. Their method was extended to allow electrical injection by Oster [2.8]. In this work, a modified method was used that has been developed in our group: the segmented contact method [2.9, 2.10] to measure the gain/loss spectrum of the studied material.

### 2.9.1 The principle

As is illustrated in figure 2.12, after a point source spontaneous emission ( $I_{se}$ ) experiences a single pass amplification in a length  $\Delta L$ , the intensity at the facet can be written as:

$$I(\Delta L) = I_{se} \exp(G\Delta L) \quad (2.1)$$

where  $G$  is the net modal gain

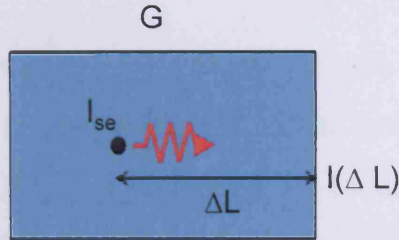


Figure 2.12 Single pass ASE in a gain medium

By integrating over the length “ $L$ ” of the pumped region, we can obtain the total ASE observed from the edge:

$$I(L) = \int_0^L I_{se} \exp(G\Delta L) = \frac{I_{se}}{G} (\exp(GL) - 1) \quad (2.2)$$

If we pump a length of “ $2L$ ”, we will have:

$$I(2L) = \frac{I_{se}}{G} (\exp(2GL) - 1) \quad (2.3)$$

By comparing equation (2.2) and (2.3), we will have an analytic solution for both the net mode gain  $G$  and internal spontaneous emission:

$$G = \frac{1}{L} \ln \left[ \frac{I(2L)}{I(L)} - 1 \right] \quad (2.4)$$

$$I_{spont} = \frac{1}{L} \ln \left[ \frac{I(2L)}{I(L)} - 1 \right] \frac{I^2(L)}{I(2L) - 2I(L)} \quad (2.5)$$

If we substitute the net modal gain  $G$  with modal gain  $G_{mod}$  minus internal loss  $\alpha_i$ , we will have:

$$G_{mod} - \alpha_i = \frac{1}{L} \ln \left[ \frac{I(2L)}{I(L)} - 1 \right] \quad (2.6)$$

## 2.9.2 The device

A schematic of a standard segmented contact device (multisection) for gain/loss measurement is shown in figure 2.4. The device usually is 50  $\mu\text{m}$  stripe (different structure like ridge waveguide can also be used). The top electrical contacts are divided into 300  $\mu\text{m}$  long, electronically isolated sections. The first two sections are used for measurement, while the rest (usually  $\geq 600$   $\mu\text{m}$  long in total) are not pumped, so they absorb any light going to the end mirror, thus ensure the single pass amplification of the light measured. The end facet can also be deliberately damaged to prevent feedback.

The intersection resistance of the multisection device needs to be checked before the gain/loss measurement. It should not be too small (normally  $> 100 \Omega$ ) in order to prevent any current leakage between sections. The I-Vs of section 1 and section 2 need to be the same. The near field of the front mirror emission also needs to have a uniform distribution and be the same shape when pumping section 1 and section 2.

## 2.9.3 Modal gain

For a particular polarization (TE or TM), the modal gain can be obtained by measuring the ASE from section 1 alone and section 1 and section 2 together under the same current density. From equation (2.6), we have:

$$G_{\text{mod}} - \alpha_i = \frac{1}{L} \ln \left( \frac{I_{\text{ASE } 12}}{I_{\text{ASE } 1}} - 1 \right) \quad (2.7)$$

Figure 2.13 shows an example of measured ASE1, ASE12 from a quantum dot sample used in this work. Figure 2.14 shows the calculated gain for this measurement (measured at 10 mA).

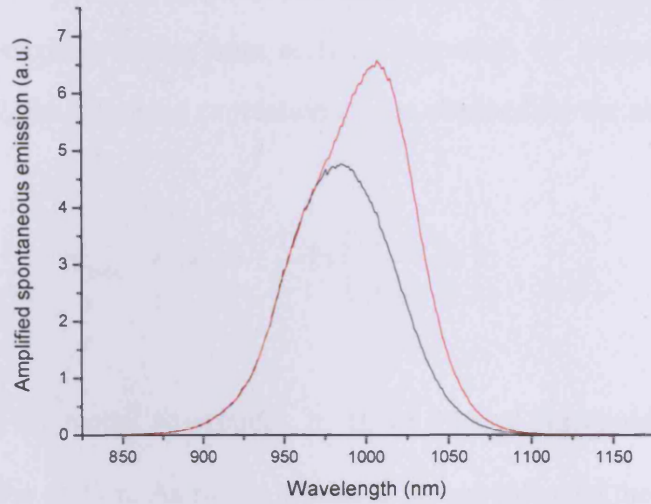


Figure 2.13 An example of measured ASE, red: ASE12, black: ASE1

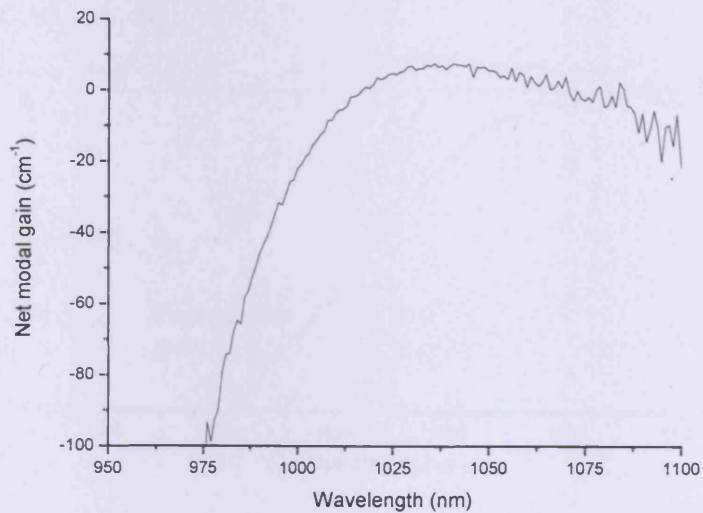


Figure 2.14 An example of measured gain spectrum at 10 mA

### 2.9.4 Modal loss and internal optical loss

For a particular polarization (TE or TM), the modal loss can be obtained by measuring the ASE when just the front section is pumped (ASE1) and when the

second section is pumped (ASE2). The difference between ASE2 and ASE1 is due to the absorption of the front section. Therefore, by comparing measured ASE1 to ASE2, the following expression can be obtained for the absorption:

$$\alpha_{\text{mod}} + \alpha_i = \frac{1}{L} \ln \left( \frac{I_{\text{ASE } 2}}{I_{\text{ASE } 1}} \right) \quad (2.8)$$

where  $\alpha_{\text{mod}}$  is the modal absorption,  $\alpha_i$  is the internal waveguide loss and L is the length of the section. As this is a passive measurement of the modal absorption in the unpumped section, the spectrum obtained is independent of the current used to generate the light.

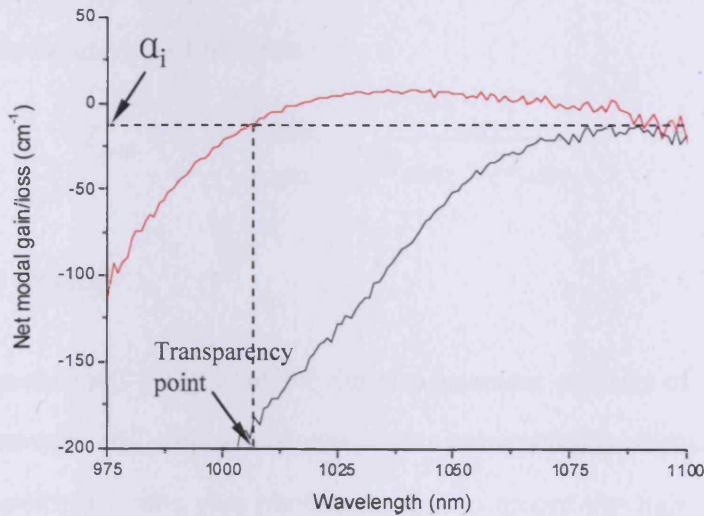


Figure 2.15 Measured gain/absorption spectrum red: gain; black: absorption spectrum

The measured net modal gain and net modal loss are plotted together in figure 2.15. As we can see they have the same value at the long wavelength (low photon energies), these photon energies are smaller than the band gap energy of the material and as such experience no gain or absorption. The only loss measured

here is the internal loss  $\alpha_i$ , so a value of  $\alpha_i$  ( $\sim 15 \text{ cm}^{-1}$  for this measurement) can be determined. The transparency point is defined as the point where the material goes from being an absorbing to gain medium (i.e.  $G_{\text{mod}}=0$ ). This can be determined from the point where the gain curves cross the value of  $\alpha_i$  at short wavelength (high energy). From this we can also determine the quasi-Fermi level separation. If the system is in thermal equilibrium, the transparency point in energy is the quasi-Fermi level separation.

### 2.9.5 Spontaneous emission

We can also find the unamplified spontaneous emission in arbitrary units for a certain polarization from the measurement. As equation (2.5) illustrated, the unamplified spontaneous emission is:

$$I_{\text{spont}} = \frac{1}{L} \ln \left( \frac{I_{\text{ASE12}}}{I_{\text{ASE1}}} - 1 \right) \frac{I_{\text{ASE1}}^2}{I_{\text{ASE12}} - 2I_{\text{ASE1}}} \quad (2.9)$$

### 2.9.6 The setup

The experimental setup used for the measurement consists of a number of optical components and a system of electronics automatically driving the device and a photomultiplier tube plus photon counter to record the light emission. A computer is used to control the apparatus and measure the light signals. A schematic diagram of the setup is shown in figure 2.16.

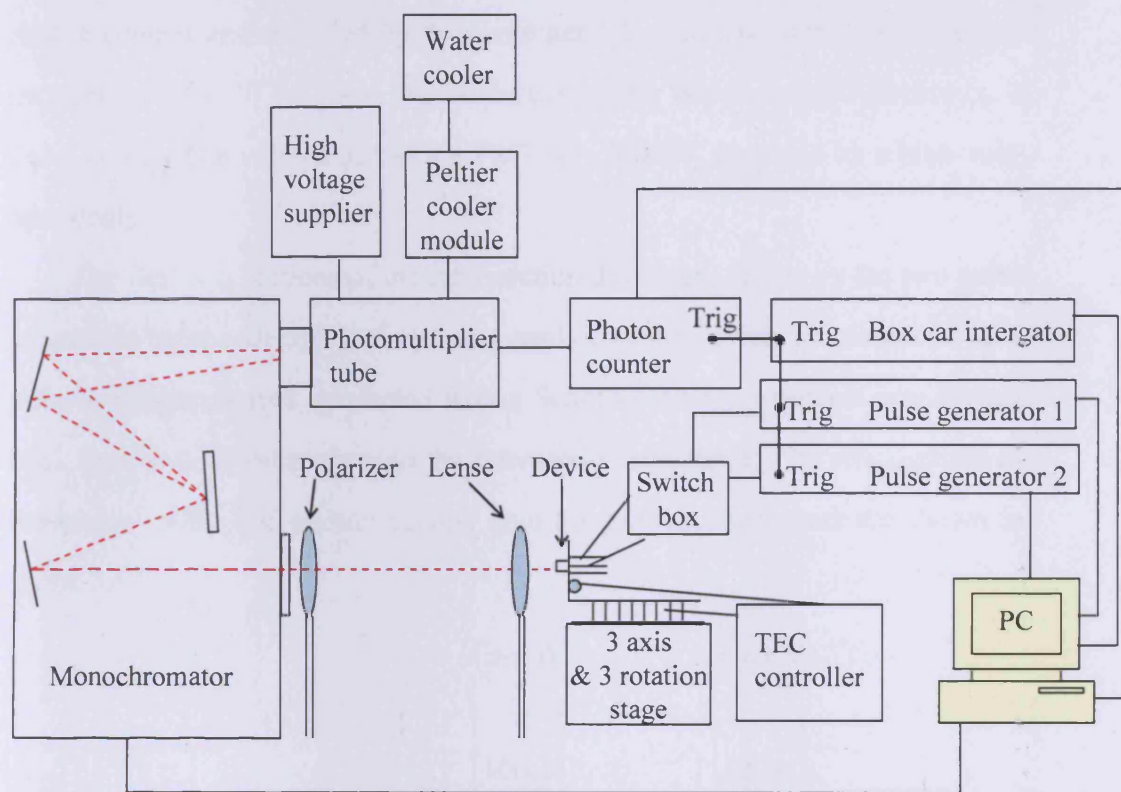


Figure 2.16 schematic diagram of the setup for gain/loss measurement

The device is mounted on the same sub-mount (mount with Peltier cooler) described previously. The current pulses produced by the pulse generators are applied to the different sections of the device through a switch box. The pulse generators are controlled by a computer allowing the amplitude of the current to be automatically varied. The current signals are acquired by a PC connected to a two channel boxcar integrator. The polarized (TE or TM) light output from the device is focused onto the entrance slit of the monochromator through the lens and polarizer using moveable stages. The monochromator is controlled by the PC, so the central output wavelength can be automatically altered during the measurement. The light from the output slit of the monochromator is collected by the photomultiplier tube (PMT). The PMT converts an optical signal to an electrical signal. The output electrical signal is then measured by the triggered

photon counter and recorded by the computer. The PMT is cooled at a constant temperature of  $-30\text{ }^{\circ}\text{C}$  by a thermoelectric cooler which is itself cooled by a water cooler. The voltage across the PMT is  $-3000\text{ V}$ , provided by a high voltage supply.

The first two sections of the multisection device are driven by the two pulse generators independently. Before being applied to the device, the output of each pulse generator is first connected with a Schottky diode to prevent any current back flow to each other through the intersection resistance. The arrangement of the current pulse and photon counter gate for gain measurements are shown in figure 2.17.

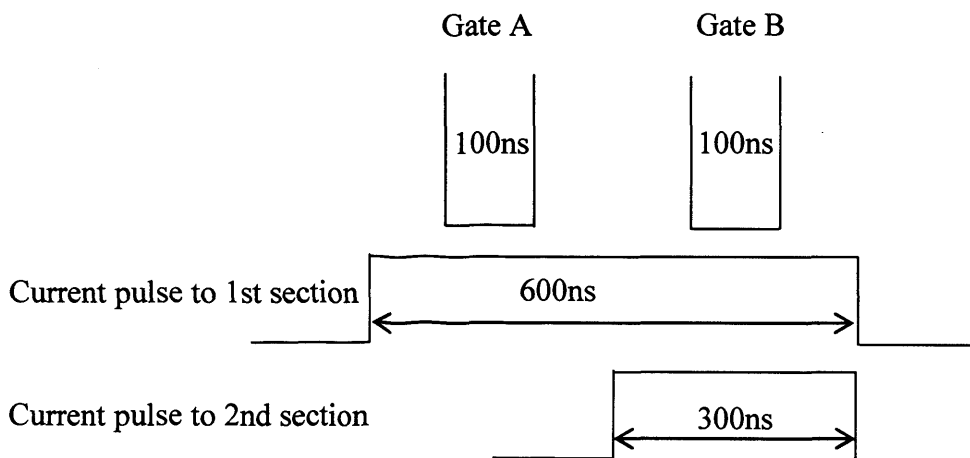


Figure 2.17 current pulse and photon counter gate for gain measurement

The current pulses are overlapped in time; the current pulse in section 1 is two times longer than the current pulse in section 2. To measure the ASE from section 1 only ( $ASE_1$ ), the photon counter gate A is set at the time when only current 1 is applied. To measure the ASE from both section 1 and section 2 ( $ASE_{12}$ ), the photon counter gate B is set at the time when both current 1 and current 2 are applied. This arrangement allows the  $ASE_1$  and  $ASE_{12}$  at a certain wavelength to

be measured in a very short time span. This means any slight variations in alignment, temperature, etc. will be present in both  $ASE_1$  and  $ASE_{12}$ . Because the gain expression involves the ratio of the ASE, these inconsistencies will cancel out. The measurement of gain is therefore more accurate than recording  $ASE_1$  and  $ASE_{12}$  separately (as if the  $ASE_1$  and  $ASE_{12}$  are measured at different time, the variation may present at some point in  $ASE_1$  but not  $ASE_{12}$ , and this will cause an inaccurate gain measurement to be obtained).

The arrangement of the current pulse and photon counter gate for loss measurements are shown in figure 2.18.

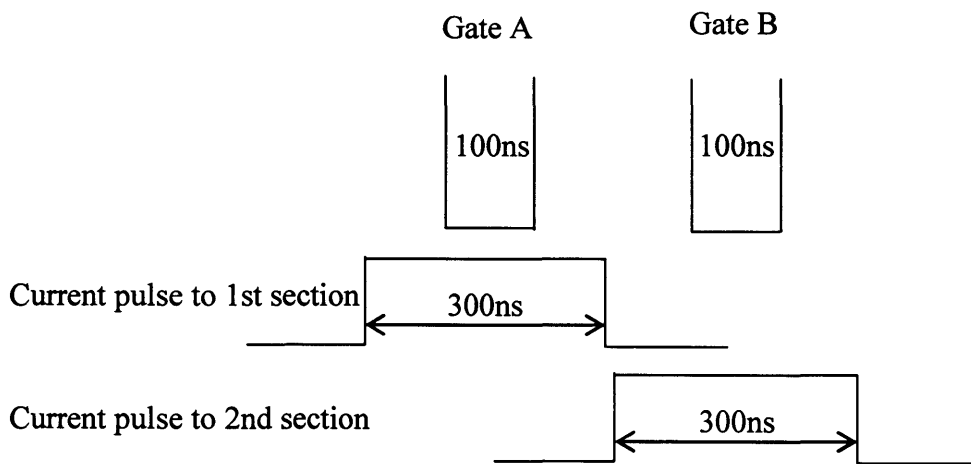


Figure 2.18 current pulse and photon counter gate for loss measurement

The current pulses are not overlapped in time. To measure the ASE from section 1 only ( $ASE_1$ ), the photon counter gate A is set at the time when only current 1 is applied. To measure the ASE from section 2 only ( $ASE_2$ ), the photon counter gate B is set at the time when only current 2 is applied. This arrangement again allows the  $ASE_1$  and  $ASE_2$  at a certain wavelength to be measured in a very short time span. As discussed above, the loss expression also involves only

the ratio of the ASE; the measurement of loss is therefore more accurate than recording ASE<sub>1</sub> and ASE<sub>12</sub> separately.

## 2.10 Noise measurement

For OCT applications, the noise of the system is very important for the quality of the acquired image. The noise at the receiver output can result from the noise of the light source, the vibration of the alignment system and the noise of the detector. To measure the noise of the quantum dot laser device investigated in this project, the setup described in figure 2.7 or figure 2.8 may be used. The relative intensity noise (RIN) is defined as [2.11]:

$$RIN = \frac{\langle \Delta P \rangle^2}{\langle P_0 \rangle} \quad (2.10)$$

where  $\langle \Delta P \rangle^2$  is the mean square optical intensity fluctuation and  $\langle P_0 \rangle$  is the average light output power. This can be measured over the whole emission wavelength range to build a RIN spectrum. The measurement can be obtained by taking repeated sweeps over the emission wavelength using the optical spectrum analyzer. Alternatively, the measurement at one wavelength can be repeated many times before moving to the next wavelength. Details of the RIN measurement can be found in [2.12]. Although the measured RIN in the setup is the system RIN (including current variation applied to the device, operating temperature variation, alignment variation and detector noise), comparison with a commercial ASE light source still provides valuable information. Results shown for the self pulsed quantum dot lasers studied in this project have a RIN level of -90 dB compared to -100 dB for a commercial ASE light source. This small difference may not arise from our laser device itself but from the electronic noise (variation of the current pulse), thermal noise (variation in operating temperature) and vibration of the

alignment in the measurement. The commercial ASE light source was well packaged with a fibre output and therefore may have less electronic noise, thermal noise and vibration.

## 2.11 Superluminescent diode measurement

During the project, SLDs provided by Exalos have also been tested. The measurement setup is similar to the one described in figure 2.8, except the mounting of the chip and the application of current are different. The SLD chip was mounted on the sub-mount which has separated pads for the anode and cathode. The chip's cathode was already mounted with one pad. The chip's anode was carefully bonded with another pad on the sub-mount with a 50  $\mu\text{m}$  gold wire. By using two probe stages and the microscope, the current may be applied. The chip was fixed on the stage using a vacuum force. A schematic of the cross section view of these components are shown in figure 2.19. The experimental results for these devices are shown in chapter 5.

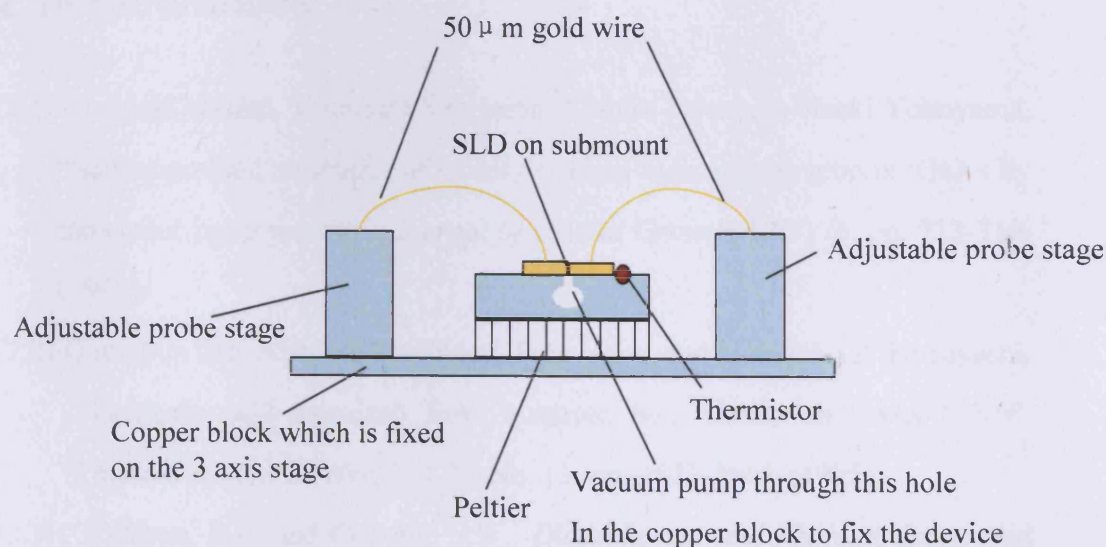


Figure 2.19 The mount for the SLD chip

## 2.12 NANOUB device measurements

The SLD source from a FP6 European commission project: NANOUB can also be implemented in the system described in figure 2.8. By carefully configuring the cooling condition and the current applied to the device, the spectra output of the device was measured and interfaced with an existing OCT system. The measurement results and the OCT image obtained are presented in Chapter 5.

## 2.13 Summary

In this chapter, the structures of selected quantum dot materials are discussed. The fabrication process and the structures of examined devices including stripe laser, ridge waveguide laser and multisection device are presented. Experiment setups and methods including optical spectra measurement, optical power measurement, time resolved spectra measurement, noise measurement, modal gain/loss measurement and etc are described.

## 2.14 References

- [2.1] Yoshiaki Nakata, Yoshihiro Sugiyama, Toshiro Futatsugi, Naoki Yokoyama, “Self-assembled structures of closely stacked InAs islands grown on GaAs by molecular beam epitaxy”, *Journal of Crystal Growth*, 175/176, pp. 713-719, (1997).
- [2.2] Qianghua Xie, Anupam Madhukar, Ping Chen, and Nobuhiko P. Kobayashi, “Vertically self-organized InAs quantum box islands on GaAs (100)”, *Physical Review Letters*, Vol 75, No. 13, pp. 2542-2545, (1995).
- [2.3] Coldren, L.A. and Corzine, S.W., *Diode Lasers and Photonic Integrated Circuits*, Wiley Series in Microwave and Optical Engineering, John Wiley

and Sons, p.53, (1995).

- [2.4] Hakki, Basil w. and Paoli, Thomas L., “Gain spectra in GaAs double-heterostructure injection lasers”, *Journal of applied physics*, Vol. 46, No. 3, pp. 1299-1306, (1975).
- [2.5] C.H.Henry, R.A.Logan, and F.R.Merritt, “Measurement of gain and absorption spectra in AlGaAs buried heterostructure lasers”, *Journal of applied physics*, Vol. 51, p. 3042, (1980).
- [2.6] P. Blood, A. I. Kucharska, J. P. Jacobs, and K. Griffiths, “Measurement and calculation of spontaneous recombination current and optical gain in GaAs - AlGaAs quantum - well structures”, *Journal of applied physics*, Vol. 70, p.1144, (1991).
- [2.7] K.L.Shanklee and R.F.Lehaney, “Direct determination of optical gain in semiconductor crystals”, *Applied Physics Letters*, Vol. 18, No. p. 475, (1971).
- [2.8] A.Oster, G.Erbert and H.Wenzel, “Gain spectra measurements by a variable stripe length method with current injection”, *Electronics letters*, Vol. 33, No. 10, p. 864, (1997).
- [2.9] J.D. Thomson, H.D. Summers, P.J. Hulyer, P.M. Snowton and P. Blood, “Determination of single-pass optical gain and internal loss using a multisection device”, *Applied Physics Letters*, Vol. 75, pp. 2527-2529, (1999).
- [2.10] Blood, P.; Lewis, G.M.; Snowton, P.M.; Summers, H.; Thomson, J.; Lutti, J.; “Characterization of semiconductor laser gain media by the segmented contact method”, *IEEE Journal of Selected Topics in Quantum Electronics*, Vol. 9, No. 5, pp. 1275-1282, (2003).
- [2.11] K. Y. Lau and A. Yariv, “Ultra-High Speed Semiconductor Lasers”, *IEEE Journal of Quantum Electronics*, Vol. 21, No. 2, pp. 121–136, (1985).

- [2.12] James Fergusson, “Understanding, developing and characterizing quantum dot lasers for use in 1050nm optical coherence tomography”, MSc thesis, Physics, Cardiff University, (2007).

# **Chapter 3 Optical properties of InGaAs quantum dot lasers**

## **3.1 Introduction**

To find the materials which have the broadband lasing emission at  $\sim 1050$  nm, stripe lasers have been fabricated using the quantum dot materials described in chapter 2. The light current characterisations and spectra measurements are shown in section 3.2. Because OCT application requires single transverse mode light source, ridge waveguide lasers have been fabricated using the selected quantum dot material: M1963. The optical spectra and power measurements of the ridge waveguide laser are shown in section 3.3. The modal gain/loss spectra for the ridge wave guide made from wafer M1963 have also been measured and shown in section 3.4.

## **3.2 Measurement of stripe Laser**

### **3.2.1 Light-current characterization**

The light current (L-I) characterization has been measured at room temperature for the fabricated standard stripe laser diodes without segmented contacts. All devices lase at room temperature. Figure 3.1, 3.2 and 3.3 shows the measured room temperature light-current curves for devices made from the M1961, M1963 and M1964 wafer respectively under pulsed current. The pulse length is  $1 \mu\text{s}$  and the pulse rate is 5 kHz.

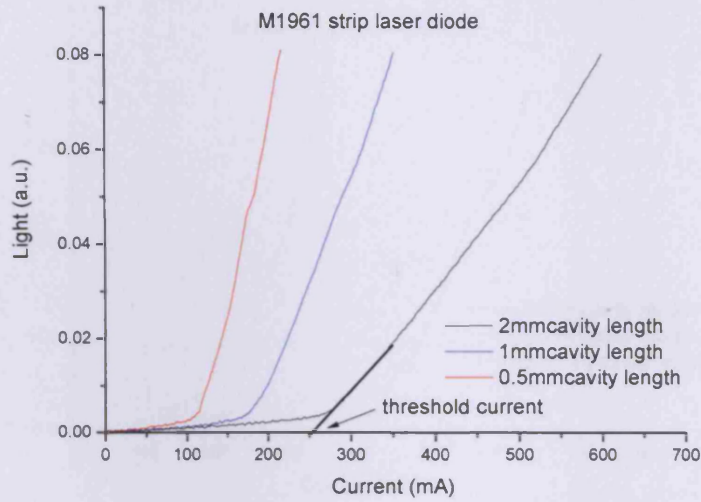


Figure 3.1 Room temperature L-I measured for stripe laser diode made of M1961 when the device is drive pulsed: pulse rate 5 kHz, pulse length 1  $\mu$ s

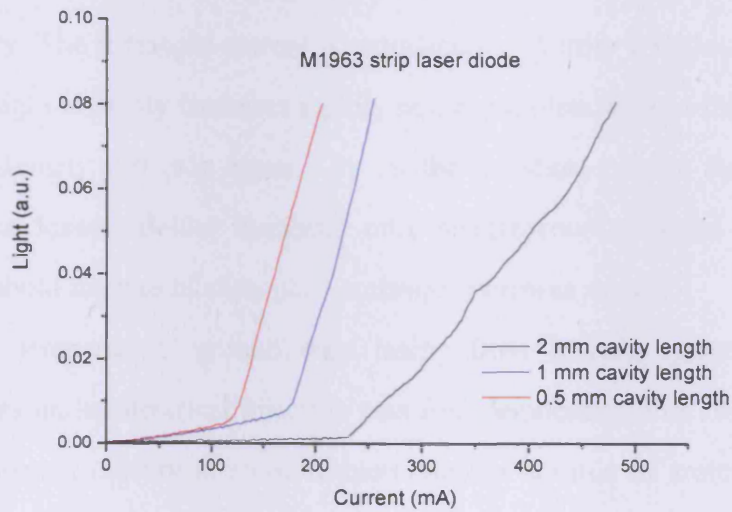


Figure 3.2 Room temperature L-I measured for stripe laser diode made of M1963 when the device is driven pulsed: pulse rate 5 kHz, pulse length 1  $\mu$ s

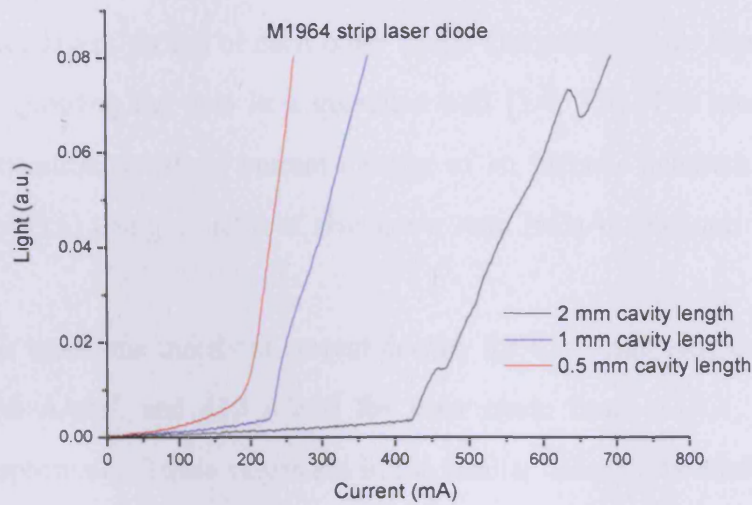


Figure 3.3 Room temperature L-I measured for stripe laser diode made of M1964 when the device is driven pulsed: pulse rate 5 kHz, pulse length 1  $\mu$ s

The X-axis represents the drive current to the laser diode and the units are in mA. The Y-axis represents the light output power from the device, and the units are arbitrary. The threshold current is extracted by identify a region of the curve where the light intensity increases rapidly and extrapolate back to the point where the light intensity = 0 (see figure 3.1). At the threshold current the modal gain matches the losses. Below threshold only spontaneous emission is observed; above threshold the rate of stimulated emission increases rapidly.

Room temperature, ground state lasing from InGaAs quantum dot heterostructures under electrical injection was first demonstrated in 1994 [3.1]. The threshold current density at room temperature has a value of around 1 kA/cm<sup>2</sup>. Since then, several approaches have been investigated to increase the modal gain in quantum dots devices. These include using wider bandgap materials for the barrier regions to decrease the leakage of carriers to these layers and using tunneling injection structures [3.2], which use quantum mechanical tunnelling to inject carriers from a quantum well directly into the dots. The total number of dots and

hence the number of states available can also be increased by stacking multiple quantum dot layers on top of each other [3.3]. The performance can also be improved by growing the dots in a quantum well [3.4, 3.5]. The lowest reported room temperature threshold current density of an InGaAs quantum dot laser is  $10.4 \text{ A/cm}^2$  [3.6] being a factor of five lower than InGaAs quantum well devices [3.7, 3.8].

In this work, the threshold current density for the 2 mm long device is:  $250 \text{ A/cm}^2$ ,  $230 \text{ A/cm}^2$ , and  $410 \text{ A/cm}^2$  for laser made from M1961, M1963 and M1964 respectively. These values are in the similar order to the multi layer InAs quantum dot lasers investigated by Ian Sandall [3.9] and the tunnel injection lasers investigated by Adrian George [3.10].

### **3.2.2 Optical spectra measurements**

As discussed in chapter 1, it is important to make sure that the central emission wavelength is around 1050 nm. After testing the fabricated devices by L-I measurements, the lasing spectrum of stripe laser device was measured using the setup described in section 2.6. The measured emission spectrum of a 2 mm stripe laser device made from the wafer M1965 is shown in figure 3.4. The spectral resolution of the measurement is 0.1 nm for all subsequent measurements.

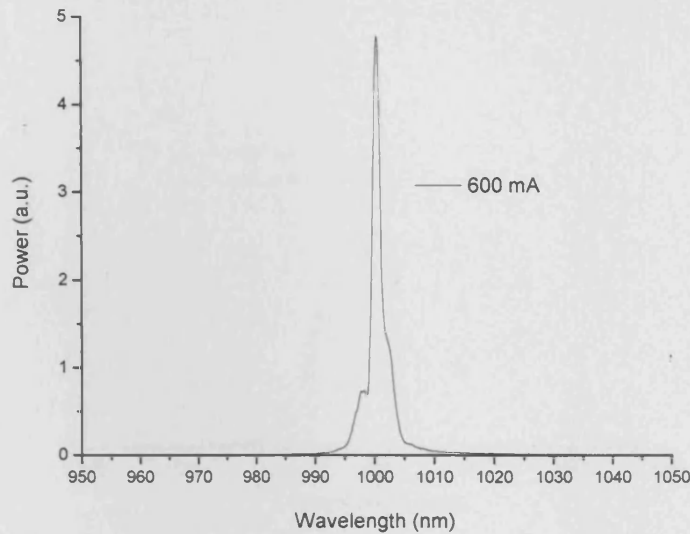


Figure 3.4 Room temperature lasing spectrum of 2 mm long stripe laser device made from the wafer M1965 when the device is driven pulsed: pulse rate 5 kHz, pulse length  $1\mu\text{s}$

As we can see from the figure, the central lasing wavelength is approximately 50 nm away from 1050 nm. This shows the material M1965 is not suitable for further development of 1050 nm light source.

The lasing spectra under different driving currents for 2 mm device made from wafers M1963, M1964 and M1961 are shown in figure 3.5, figure 3.6 and figure 3.7 respectively. The threshold currents for the M1963, M1964 and M1961 device are 230 mA, 410 mA and 250 mA respectively. The cavity mode spacing for 2 mm long device is  $\sim 0.07$  nm; the resolution is not high enough to see the individual longitudinal modes.

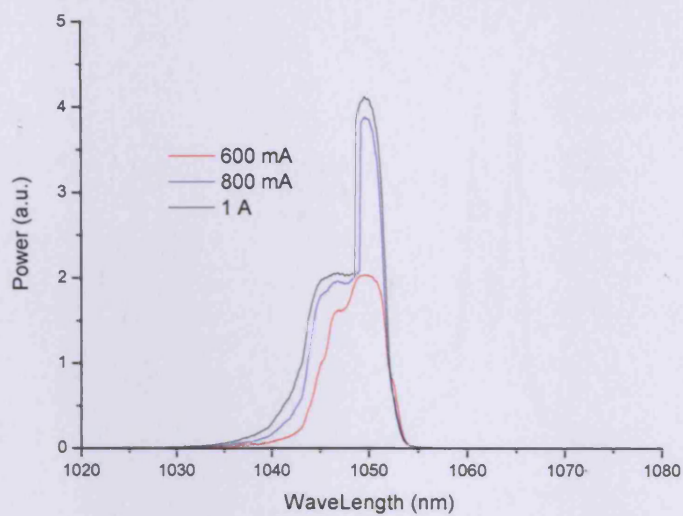


Figure 3.5 Room temperature lasing spectra of 2 mm long stripe laser device made from wafer M1963 when the device is driven pulsed: pulse rate 5 kHz, pulse length 1  $\mu$ s

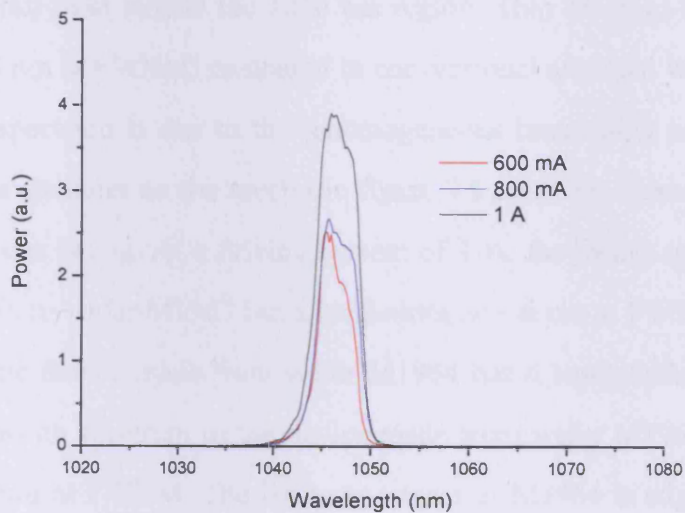


Figure 3.6 Room temperature lasing spectra of 2 mm long stripe laser device made from wafer M1964 when the device is driven pulsed: pulse rate 5 kHz, pulse length 1  $\mu$ s

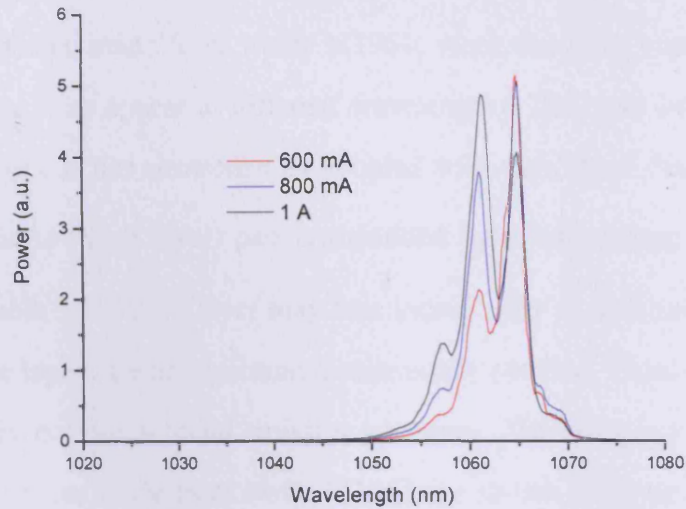


Figure 3.7 Room temperature lasing spectra of 2 mm long stripe laser device made from wafer M1961 when the device is driven pulsed: pulse rate 5 kHz, pulse length  $1\mu\text{s}$

As we can see from the results, devices made from wafers M1963, M1964 and M1961 emit light around the 1050 nm region. They all have a broad lasing spectrum ( $> 5$  nm at FWHM) compared to conventional quantum well lasers. The broad lasing spectrum is due to the inhomogeneous broadening as discussed in chapter 1. The shoulder on the spectra in figure 3.5 could be caused by the multi transverse modes lasing. At a driving current of 1 A, the lasing spectrum of the device made from wafer M1963 has a bandwidth of  $\sim 6$  nm at FWHM, the lasing spectrum of the device made from wafer M1964 has a bandwidth of  $\sim 5$  nm at FWHM, the lasing spectrum of the device made from wafer M1961 has a bandwidth of  $\sim 6$  nm at FWHM. The lasing spectrum of M1964 is slightly narrower than that of M1963. The narrowed emission spectrum of M1964 may due to the effect of size averaging during the stacking process (M1964 has seven repeat layers of dots while M1963 has five layers). Because the thickness of the GaAs layer between the dots layer is very thin (7nm), the upper layer dots are grown on seed potentials formed by lower layer dots, which results in size averaging in the lateral

direction [3.11]. Therefore, the inhomogeneous broadening is reduced.

For the device made from wafer M1961, when the drive current increases, lasing emission lines appear at different wavelengths. This may be because each InGaAs dot layer is not electronically coupled with each other since the InGaAs (dot layer) /GaAs (Well layer) pair is separated by a high energy  $\text{Al}_{0.15}\text{Ga}_{0.85}\text{As}$  barrier (see table 3.1). Each layer may lase individually at different wavelengths [3.12] because layers are not quantum mechanically coupled. Thus, all the dot layers collectively provide a broad emission spectrum. The lasing spectra for 1 mm and 0.5 mm devices made from wafer M1961 are shown in figure 3.8 and figure 3.9. The mode spacing for a 0.5 mm cavity at  $1 \mu\text{m}$  is  $\sim 0.287 \text{ nm}$ , the spectral resolution ( $0.1 \text{ nm}$ ) is high enough to see the individual mode, but we can not see the separate longitudinal modes in the emission spectra. This is because the multi transverse modes and multi longitudes modes are merged together. Both emissions have broad bandwidth:  $\sim 10 \text{ nm}$  at FWHM for the 1 mm device and  $\sim 15 \text{ nm}$  at FWHM for the 0.5 mm device when driven at 1 A.

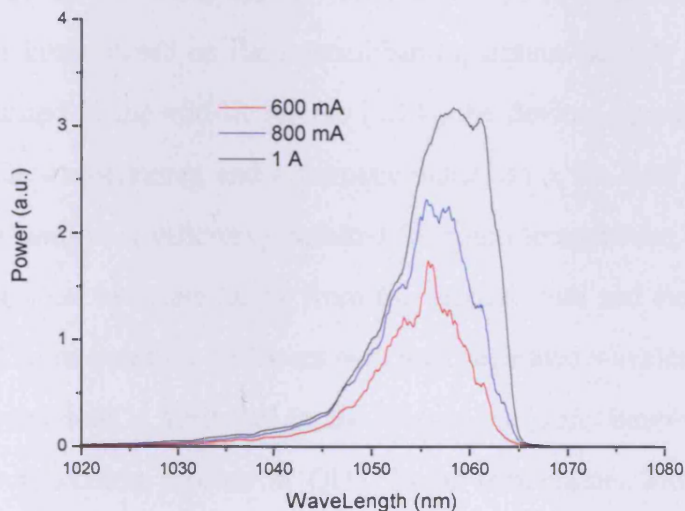


Figure 3.8 Room temperature lasing spectra of a 1 mm long stripe laser device made from wafer M1961 when the device is driven pulsed: pulse rate 5 kHz, pulse length  $1 \mu\text{s}$

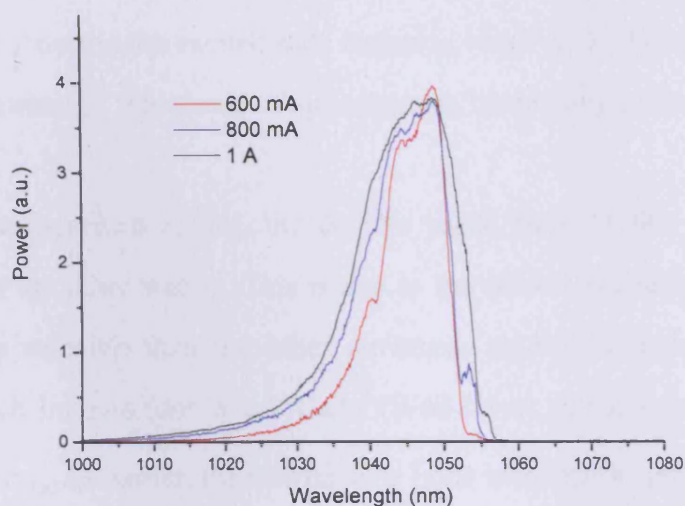


Figure 3.9 Room temperature lasing spectra of a 0.5 mm long stripe laser device made from wafer M1961 when the device is driven pulsed: pulse rate 5 kHz, pulse length  $1\mu\text{s}$

A conventional quantum-well laser generally produces a narrow spectrum with a spectral width in the subnanometer order for a single-frequency laser to a few nanometres for multilongitudinal mode lasers [3.13]. Although broadband semiconductor lasers based on the intersubband quantum-cascade principle have been demonstrated in the mid-IR regime [3.14], the devices operated effectively under cryogenic temperatures, and a dramatic reduction in the laser line width and extremely low wall-plug efficiency resulted for room temperature operation. Recently simultaneous two-state lasing from the ground state and excited state has been observed from quantum-dot lasers with well separated wavelength emissions [3.15]. This behaviour is attributed to the incomplete gain clamping and the retarded carrier relaxation process in QDs. Room-temperature broadband lasing emission covers a bandwidth of  $\sim 40$  nm from an InGaAs/GaAs quantum dots laser has been reported in 2006 [3.13]. The broadband emission results from the superposition of quantized lasing states from highly inhomogeneous dots. Quan-

tum dot lasers with a 75 nm broad spectrum of emission have been reported by another group in 2007 [3.16]. A significant overlap and approximate equalization of the ground-state and the excited state emission bands in the laser's spectrum is achieved by means of intentional inhomogeneous broadening of the quantum dot energy levels.

From the measured results, the devices made from M1961 have broader emission than the other wafers. This is due to the M1961 wafer has more inhomogeneous broadening than the other structures studied. Comparing to other structures, each InGaAs (dot layer) /GaAs (Well layer) pair is separated by high energy  $\text{Al}_{0.15}\text{Ga}_{0.85}\text{As}$  barrier, the intermediate layer is thicker than that used in the other structures and this may lead the dots to form more independently between layers, hence more inhomogeneous broadening [3.17].

### 3.2.3 Power measurements

The room temperature output power of a 0.5 mm long chip made from the M1961 wafer has been measured by using a laser power meter (model AN12 from OPHIR). The threshold current for this device is 110 mA. The detector was placed close to the diode output. The measured light average power over the pulses was 0.48 mW at 600 mA, 0.76 mW at 800 mA and 1.05 mW at 1 A for pulsed operation. The current pulse width was 500 ns, the frequency was 5 KHz, and so the duty cycle of the system is 0.25%.

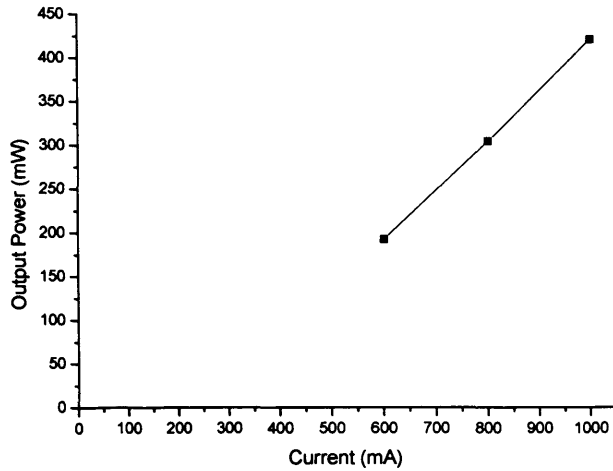


Figure 3.10 Calculated quasi-CW output power for a 0.5 mm stripe laser diode made from M1961

The equivalent calculated quasi-CW power (averaged power over the pulses divided by the duty cycle) is shown in figure 3.10. The output power is in the region of hundreds mW and this indicates the power is large enough for OCT applications.

### 3.3 Ridge waveguide laser

Because the limited amount of quantum dot material M1961 available, only ridge devices of width 2  $\mu\text{m}$  and height 1.54  $\mu\text{m}$  were fabricated using wafer M1963. After fabrication, the ridge devices were tested as follows.

#### 3.3.1 Light-current characterization

For OCT applications, the ideal device will work under continuous drive current operation. The ridge devices were tested under continuous current operation using the setup described in chapter 2. Results show that the devices lase under continuous drive current operation. The measured L-I curves for different length

devices under continuous drive current operation are shown in Figure 3.11. The X-axis represents the drive current to the device and the unit is in mA. The Y-axis represents the measured output power from one facet of the ridge laser in real units, the units are in mW.

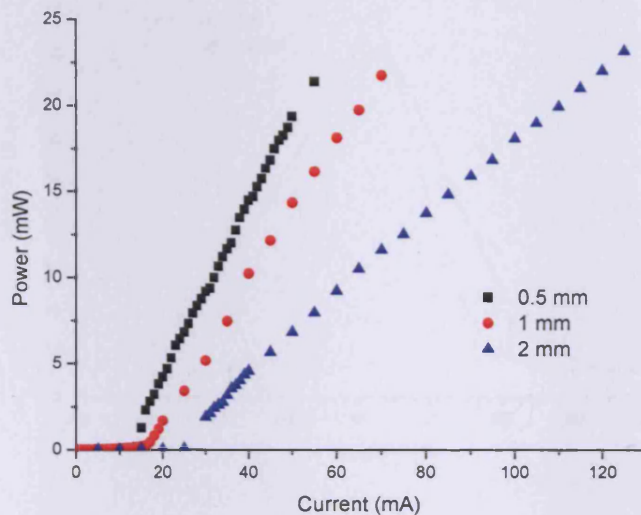


Figure 3.11 L-I characteristics at 15 °C for the ridge-waveguide lasers under continuous drive current operation

### 3.3.2 Far field measurement

In order to check the single transverse-mode operation, the far-field patterns of the ridge waveguide lasers were measured. Figure 3.12 shows the far field pattern of both the horizontal and vertical direction for a 1 mm long ridge waveguide laser. Gaussian-like transverse mode profiles show fundamental transverse-mode operation for the ridge waveguide laser. The FWHM of the vertical field pattern is  $\sim 50^\circ$  and the FWHM of the horizontal field pattern is  $\sim 30^\circ$ . To improve the coupling efficiency from the light output into a single mode fibre, the vertical field pattern and the horizontal field pattern ideally need to be the same. By enlarging

the confinement structure, we can decrease the divergence of the beam therefore narrow the far field pattern. The vertical profile can be narrowed by increasing the active region thickness. More dot layers will also provide more gain. The horizontal field can also be narrowed by increasing the ridge width.

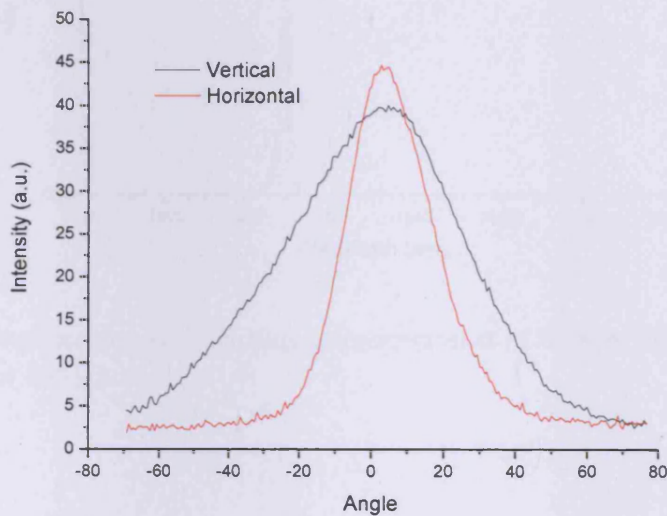


Figure 3.12 Far field patterns for a 1mm long ridge device

### 3.3.3 Optical spectra measurement

The optical spectra of the ridge laser devices have been measured using the setup described in chapter 2. The typical spectra for 1 mm and 2 mm device are shown in figure 3.13 and figure 3.14 respectively. The spectral resolution is 0.1 nm for both measurements.

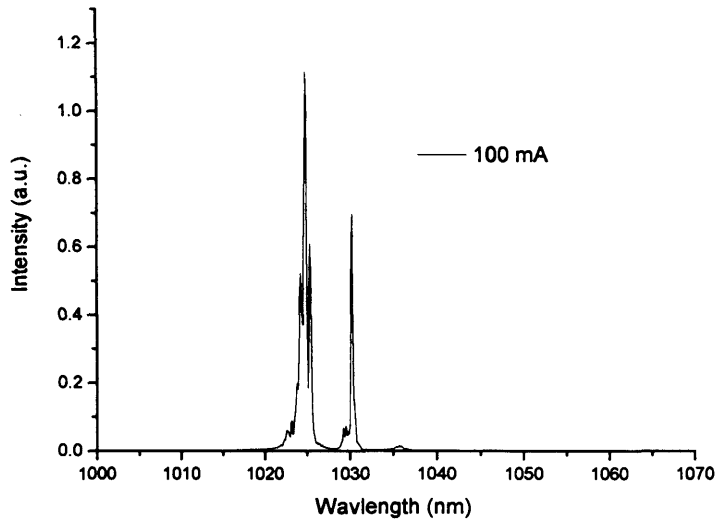


Figure 3.13 Lasing spectrum for 1 mm ridge laser operated at 15 °C when driven at a continuous current of 100 mA

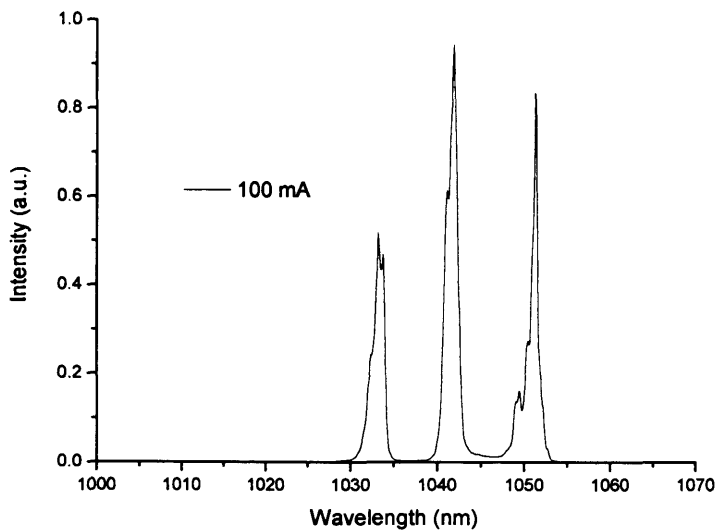


Figure 3.14 Lasing spectrum for 2 mm ridge laser operated at 15 °C when driven at a continuous current of 100 mA

As we can see from the results, the lasing wavelength moves toward the shorter wavelength as the device length is decreased. The lasing spectrum of the 2 mm ridge laser is at longer wavelength and closer to 1050 nm than the lasing

spectrum of the 1 mm ridge laser. This is because of the increased threshold gain for the shorter device (see equation 1.19). As shown in the measured gain spectra (figure 3.15), the peak gain wavelength shifts to shorter wavelength when the drive current increases. Both lasing spectra are broad but contain multiple peaks. The lasing spectrum of the 2 mm device covers a range of  $\sim 25$  nm. We could not see discrete peaks in the lasing spectra of 2 mm stripe device in figure 3.5; this could be because the multi transverse modes and multi longitudinal modes are merged together for stripe laser. The discrete lasing peaks are groups of modes originating from the substrate leakage and reflection effect [3.18]. These separated modes will produce secondary sub peaks in the temporal coherence function, which can be detrimental to clear image formation in OCT [3.19]. By applying the self pulsation technique to the device, the discrete modes merge to form a broad continuous lasing spectrum. The changing of the spectrum is observed instantaneously using the streak camera. The experimental results are shown in the next chapter.

### 3.4 Gain and loss measurement

The net modal gain, net modal loss and the internal optical loss of the ridge laser made from wafer M1963 have been measured using the method described in chapter 2.

The measured net modal gain and net modal loss spectra at 15 °C are shown in figure 3.15. Colour labels indicated the current applied on a 300  $\mu\text{m}$  long ridge (2  $\mu\text{m}$  wide). The results demonstrate the general features of this particular quantum dot system. The gain spectra are broad and continuous over the whole wavelength range, within which the ground and excited states of the dots cannot be distinguished. This may be explained by the large amount of inhomogeneous broadening present in the dots ensemble. When there are a large number of dots with

varying size present in the sample, there will be a large variation in the energy of the confined states. This variation causes large inhomogeneous broadening which results in a wide gain spectrum. The shape of the gain spectra are flat so the adjacent wavelengths see almost same gain as the peak, this contributes to the broadband nature of the output of the lasing device made of M1963. The internal optical loss was measured to be  $\sim 15 \text{ cm}^{-1}$ . One may also see the effect where the peak of the modal gain moves to shorter wavelength as the drive current increases.

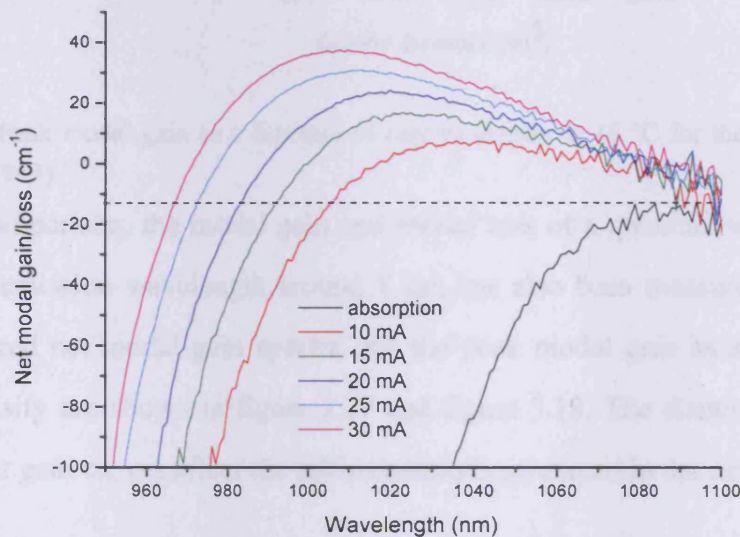


Figure 3.15 Net modal gain and Net loss measured at 15 °C for the quantum dot material M1963

The peak modal gain as a function of current density is shown in figure 3.16. The loss values are taken at the 1050 nm. As we can see, the differential change in absorption region is greater than that in the gain. This is one important requirement for making a self pulsing device. The details are discussed in the next chapter.

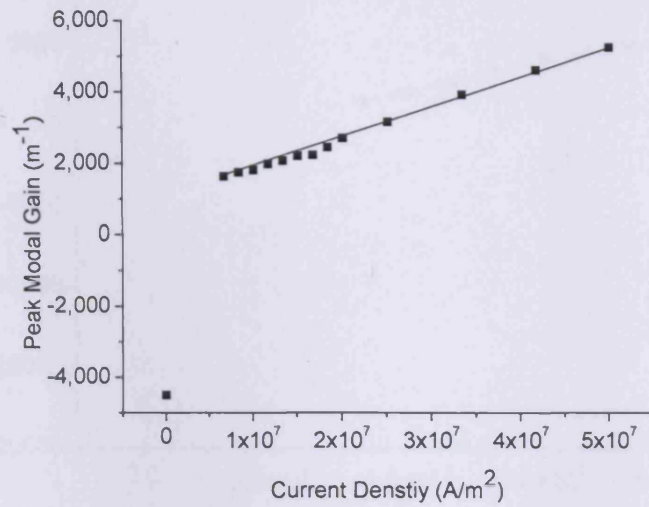


Figure 3.16 Peak modal gain as a function of current density at 15 °C for the quantum dot material (M1963)

For comparison, the modal gain and modal loss of a quantum well material which has emission wavelength around 1  $\mu\text{m}$  has also been measured at 15 °C. The measured net modal gain spectra and the peak modal gain as a function of current density are shown in figure 3.17 and figure 3.18. The discussion of how the different gain curves affect the self pulsation is presented in the next chapter.

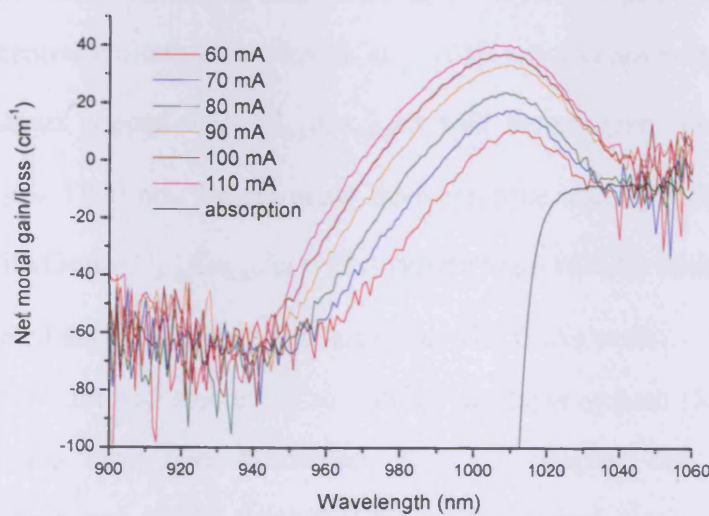


Figure 3.17 Net modal gain/loss spectra measured at 15 °C for the quantum well material

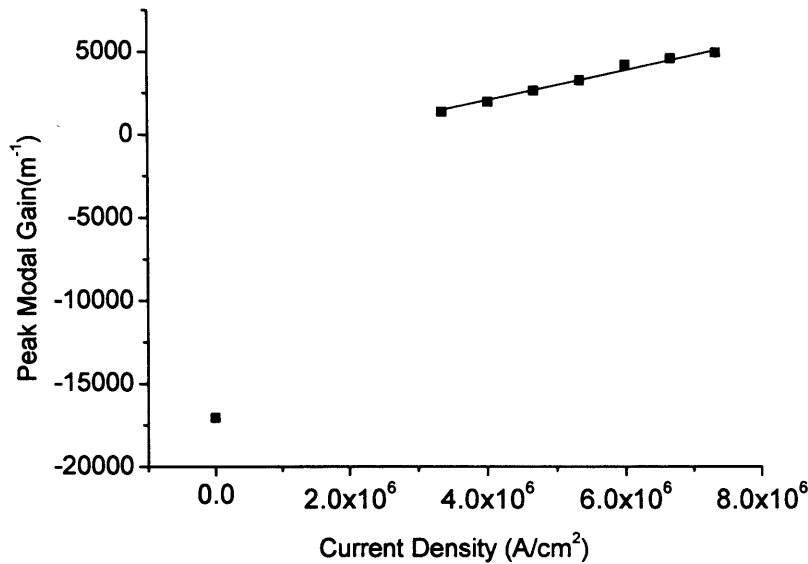


Figure 3.18 Peak modal gain as a function of current density at 15 °C for the quantum well material

### 3.5 Summary

Measured lasing spectra of stripe lasers made from different quantum dot materials show that lasers made from InGaAs dot layers capped with GaAs well layers have central emission wavelength at  $\sim 1050$  nm and lasers made from InGaAs dots layers capped with  $\text{Al}_{0.15}\text{Ga}_{0.85}\text{As}$  well layers have central emission wavelength at  $\sim 1000$  nm. Lasers made from multiple uncoupled dot layer (InGaAs dots with GaAs/ $\text{Al}_{0.15}\text{Ga}_{0.85}\text{As}$  wells) system has a broader emission than the multiple coupled dot layer system (InGaAs dots with GaAs wells).

Because the limited amount of uncoupled dot layer system (M1961), ridge waveguide lasers have been fabricated using the coupled dot layer system (M1963). Experiments results show that the central emission wavelength of the device can be controlled over a small range ( $\sim 10$  nm) by varying the device length.

Shorter devices have emission at shorter wavelengths while longer devices have emission at longer wavelengths. The lasing spectra contain discrete peaks, which are groups of modes originating from the substrate leakage and reflection effect [3.18]. The lasing spectra were broadened using the self pulsation technique and the results are shown in the next chapter.

### 3.6 References

- [3.1] N. Kirstaedter, N. N. Ledentsov, M. Grundmann, D. Bimberg, V. M. Ustinov, S.S. Ruvimov, M. V. Maximov, P. S. Kopev, Z. I. Alferov, U. Richter, P. Werner, U. Gosele, and J. Heydenreich, "Low threshold, large  $T_0$  injection laser emission from (InGa)As quantum dots", *Electronics Letters*, Vol. 30, No.17, pp. 1416-1417 (1994).
- [3.2] P. Bhattacharya, S. Ghosh, S. Pradhan, J. Singh, Z. K. Wu, J. Urayama, K. Kim, and T. B. Norris, "Carrier dynamics and high-speed modulation properties of tunnel injection InGaAs-GaAs quantum-dot lasers", *IEEE Journal of Quantum Electronics*, Vol. 39, No.8, pp. 952-962, (2003).
- [3.3] V. M. Ustinov, A. Y. Egorov, A. R. Kovsh, A. E. Zhukov, M. V. Maximov, A.F. Tsatsulnikov, N. Y. Gordeev, S. V. Zaitsev, Y. M. Shernyakov, N. A. Bert, P.S. Kopev, Z. I. Alferov, N. N. Ledentsov, J. Bohrer, D. Bimberg, A. O.Kosogov, P. Werner, and U. Gosele, "Low-threshold injection lasers based on vertically coupled quantum dots", *Journal of Crystal Growth*, 175/176, pp. 689-695, (1997).
- [3.4] A. E. Zhukov, A. R. Kovsh, N. A. Maleev, S. S. Mikhrin, V. M. Ustinov, A. F. Tsatsul'nikov, M. V. Maximov, B. V. Volovik, D. A. Bedarev, Y. M. Shernyakov, P. S. Kopev, Z. I. Alferov, N. N. Ledentsov, and D. Bimberg, "Long-wavelength lasing from multiply stacked InAs/InGaAs quantum dots

- on GaAs substrates”, *Applied Physics Letters*, Vol. 75, No.13, pp. 1926-1928, (1999).
- [3.5] L. F. Lester, A. Stintz, H. Li, T. C. Newell, E. A. Pease, B. A. Fuchs, and K. J. Malloy, “Optical Characteristics of 1.24- $\mu\text{m}$  InAs quantum-dot Laser diodes”, *IEEE Photonics Technology Letters*, Vol. 11, No. 8, pp. 931-933, (1999).
- [3.6] D.G.Deppe, K.Shavritranuruk, G. Ozgur, H. Chen and S. Freisem, “ Quantum dot laser diode with low threshold and low internal loss”, *Electronics Letters*, Vol. 45, No. 1, (2009).
- [3.7] N. Chand, E. E. Becker, J. P. Van der Ziel, S. N. G. Chu, and N. K. Dutta, “Excellent uniformity and very low ( $<50\text{A}/\text{cm}^2$ ) threshold current density strained InGaAs quantum well diode lasers on GaAs substrate”, *Applied Physics Letters*, Vol. 58, No. 16, pp. 1704-1706, (1991).
- [3.8] G. W. Turner, H. K. Choi, and M. J. Manfra, “Ultralow-threshold ( $50\text{A}/\text{cm}^2$ ) strained single-quantum-well GaInAsSb/AlGaAsSb lasers emitting at  $2.05\mu\text{m}$ ”, *Applied Physics Letters*, Vol. 72, No. 8, pp. 876-878, (1998).
- [3.9] Ian C. Sandall, “The characterization of In(Ga)As quantum dot lasers”, PhD thesis, Cardiff university, (2006).
- [3.10] Adrian A.George, “Carrier distributions in long wavelength quantum dot laser diodes”, PhD thesis, Cardiff university, (2007).
- [3.11] H.Shoji, Y. Nakata, K.Mukai, Y. Sugiyama, M. Sugawara, N. Yokoyama, and H.Ishikawa, “Self-Formed In(Ga)As Quantum Dot Lasers”, *Lasers and Electro-Optics Society Annual Meeting*, conference proceedings., IEEE, (1997).
- [3.12] Mitsuru Sugawara, Kohki Mukai, and Yoshiaki Nakata, “Light emission spectra of columnar-shaped self-assembled InGaAs/GaAs quantum-dot

lasers: Effect of homogeneous broadening of the optical gain on lasing characteristics”, *Applied physics letters*, Vol. 74, No. 11, pp. 1561-1563, (1999).

- [3.13] H.S.Djie and B.S.Ooi, X.-M. Fang, Y. Wu, J. M. Fastenau, W. K. Liu, and M. Hopkinson, “Room-temperature broadband emission of an In-GaAs/GaAs quantum dots laser”, *Optics letters*, Vol. 32, No. 1, pp. 44-46, (2007).
- [3.14] C. Gmachl, D. L. Sivco, R. Colombelli, F. Capasso, and A. Y. Cho, “Ultra-broadband semiconductor laser”, *Nature*, Vol. 415, P883-887, (2002).
- [3.15] A. Markus, J. X. Chen, C. Paranthoen, A. Fiore, C. Platz, and O. Gauthier-Lafaye, “Simultaneous two-state lasing in quantum-dot lasers”, *Applied physics letters*, Vol. 82, No. 12, pp. 1818-1820, (2003).
- [3.16] A. Kovsh, I. Krestnikov, D. Livshits, S. Mikhrin, and J. Weimert, “Quantum dot laser with 75 nm broad spectrum of emission”, *Optics letter*, Vol. 32, No. 7, pp. 793-795, (2007).
- [3.17] Kohki Mukai and Mitsuru Sugawara, “optical characterization of quantum dots”, in *Semiconductors and semimetals*, Vol. 60, Ed. Mitsuru Sugawara, p.185, London, Academic press, (1999).
- [3.18] D. Bhattacharyya, E. A. Avrutin, A. C. Bryce, J. H. Marsh, D. Bimberg, F. Heinrichsdorff, V. M. Ustinov, S. V. Zaitsev, N. N. Ledntsov, P. S. Kop’ev, Zh. I. Alferov, A. I. Onischenko, and E. P. O’Reilly, “Spectral and dynamic properties of InAs-GaAs self-organized quantum-dot lasers”, *IEEE Journal of Selected Topics in Quantum Electronics*, Vol. 5, No. 3, pp. 648-656, (1999).
- [3.19] A. F. Fercher, W. Drexler, C. K. Hitzenberger, and T. Lasser, “Optical coherence tomography – principles and applications”, *Reports on progress*

*in physics*, Vol. 66, No. 2, pp. 239-303, (2003).

# Chapter 4 Self pulsation in quantum dot lasers

## 4.1 Introduction

Self pulsation has been examined using the multi-section stripe lasers and multi-section ridge waveguide lasers made from material M1963. The spectra broadening effects have been observed for both cases and the results are presented in section 4.2 and section 4.3. In section 4.4, the spectra broadening effects have been explained using a rate equation simulation. The effects of different parameters to the self pulsation such as the drive current to the gain section, the reverse bias on the absorber section, the device operating temperature and the gain spectra shape have also been discussed.

## 4.2 Multi-section stripe lasers

In order to test if the device self pulsates, the selected quantum dot material M1963 was fabricated into multi-section 50  $\mu\text{m}$  stripe laser structures. Figure 4.1 shows a schematic of the device. The figure only shows a device with 5 sections. The length of each section is 100  $\mu\text{m}$ . In the real case, depending on the length of the device, the device can have up to 20 sections for a 2 mm device. In between these sections, the metal contact was removed to form a 4  $\mu\text{m}$  electrically isolated region. Individual sections can be jointed by epoxy to act as one section. The section then can be forward biased to act as a gain section. The section can also be earthed or reverse biased to act as a saturable absorber. It was shown in ref [4.1] that by applying a reverse bias to the absorber section, one can effectively reduce the absorber recovery time which is important for generating ultra fast pulses.

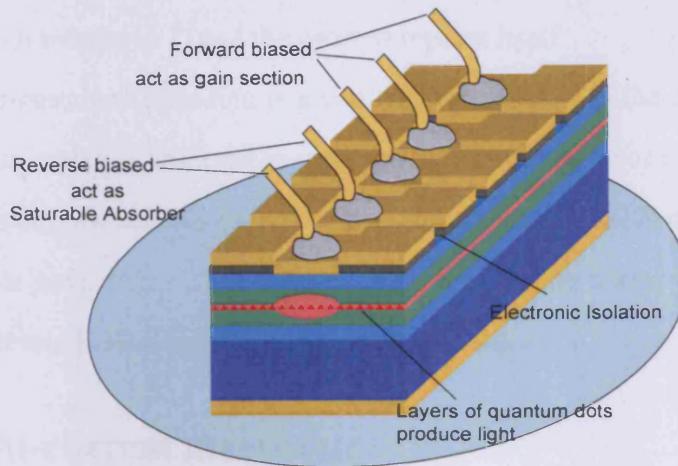


Figure 4.1 Self-pulsating stripe laser

Devices with different absorption/gain ratios can be tested using this method. The absorber can be placed at the front or at the end of the device in order to achieve self-pulsation. The absorber may also be placed at the centre of the device to form a colliding pulse setup [4.2]. For simplicity, for the devices tested in this project, the absorber was placed at either the front or at the end of the device. The mechanism of pulsation may be understood by variations of the photon densities and the electron densities [4.3]:

- 1) When the photon does not exist, the electron density in the gain region is increased by the injection current.
- 2) Approaching threshold, photons begin to generate in the gain region and are absorbed in the absorber region.
- 3) The electron density in the absorber region is increased due to the absorption.
- 4) The absorbing rate in the absorber region is reduced with the increase of electron density in the region. Subsequently the photon density increases much more due to the reduced absorption.
- 5) The electron density in the gain region is reduced due to stimulated emission of photons. The lasing operation subsides, resulting in no photon.

6) The situation returns to 1) and the process repeats itself

Thus, the self-sustained pulsation is a similar phenomenon to the damped relaxation oscillation which is observed in conventional semiconductor lasers. The principle difference between this pulsation and the relaxation oscillation is that the latter does not have terms 3) and 4) as mentioned in the above process, which means that the oscillation will relax to a constant value.

### 4.2.1 Light-current measurements

Devices with different absorption/gain ratios have been tested. The length of the absorber was 50  $\mu\text{m}$  or 100  $\mu\text{m}$  and the overall length of the devices were 2 mm, 1 mm, and 0.5 mm. L-I measurements have been taken under different reverse bias conditions. The reverse bias applied on the absorber was varied from 0 to 3 V. The room temperature L-I measurements for different devices under various reverse bias are shown in the following figures. Devices were driven pulsed with pulse width of 1  $\mu\text{s}$  and pulse rate of 5 kHz.

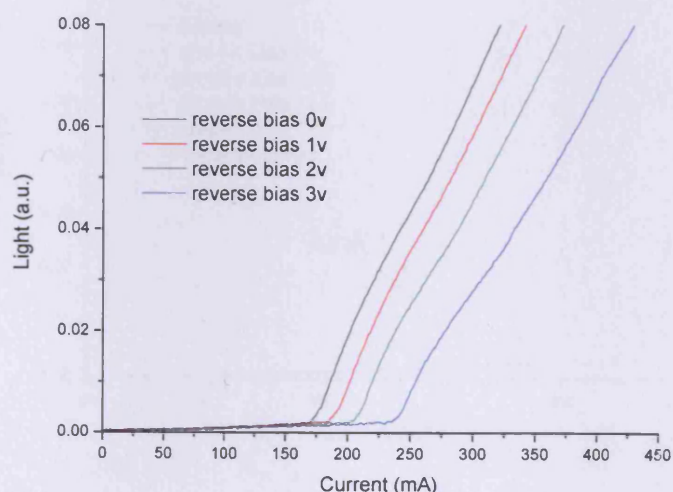


Figure 4.2 L-I characteristics for 2 mm stripe with 100  $\mu\text{m}$  absorber section with 0 – 3 V reverse bias when the device is driven pulsed: pulse rate 5 kHz, pulse length 1  $\mu\text{s}$

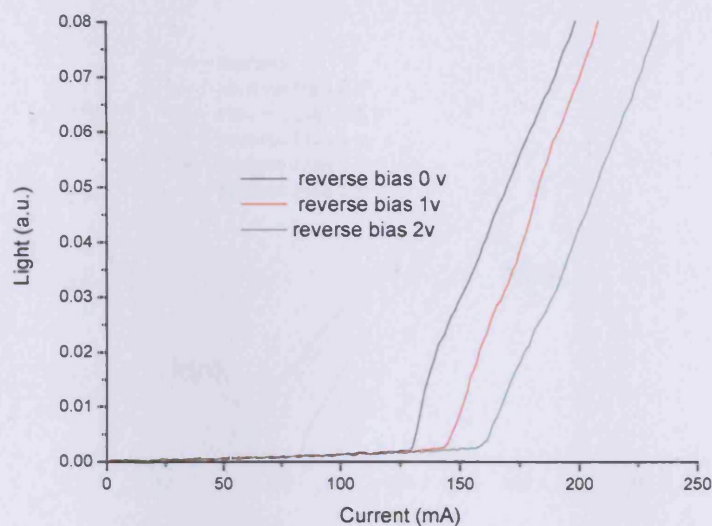


Figure 4.3 L-I characteristics for 1 mm stripe with 50  $\mu\text{m}$  absorber section with 0 – 2 V reverse bias when the device is driven pulsed: pulse rate 5 kHz, pulse length 1  $\mu\text{s}$

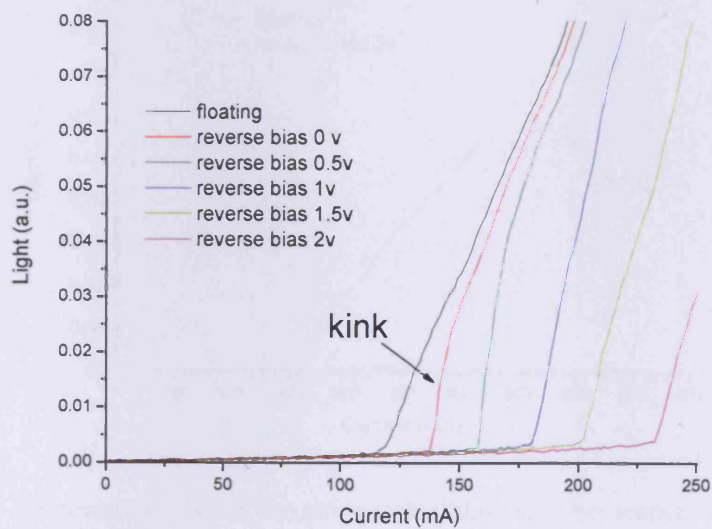


Figure 4.4 L-I characteristics for 1 mm stripe with 100  $\mu\text{m}$  absorber section with 0 – 2 V reverse bias when the device is driven pulsed: pulse rate 5 kHz, pulse length 1  $\mu\text{s}$

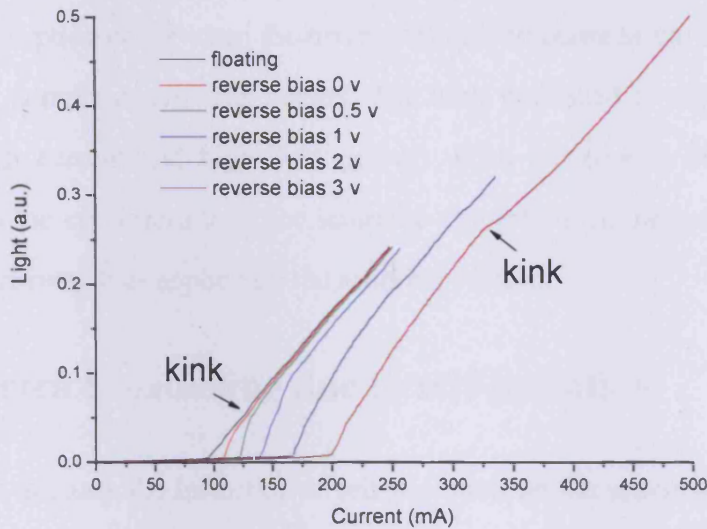


Figure 4.5 L-I characteristics for 0.5 mm stripe with 50  $\mu\text{m}$  absorber section with 0 – 3 V reverse bias when the device is driven pulsed: pulse rate 5 kHz, pulse length 1  $\mu\text{s}$

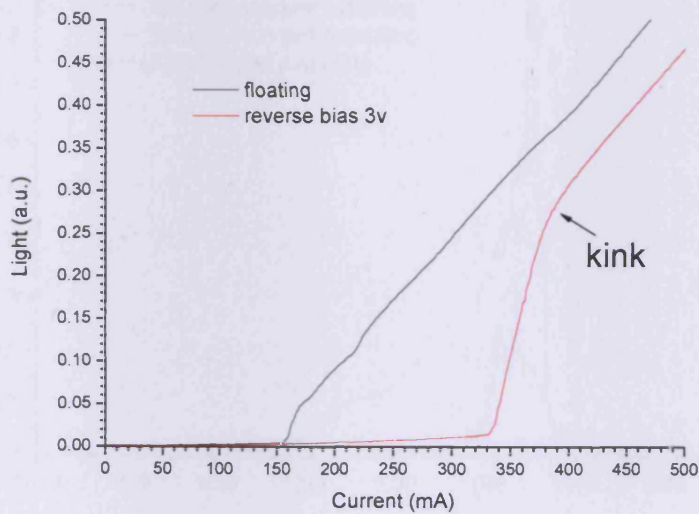


Figure 4.6 L-I characteristics for 0.5 mm stripe with 100  $\mu\text{m}$  absorber section with 3V reverse bias when the device is driven pulsed: pulse rate 5 kHz, pulse length 1  $\mu\text{s}$

As we can see from figure 4.4, figure 4.5 and figure 4.6, when the absorber/gain ratio is equal or larger than 1/10, there are kinks on the L-I curves.

These kinks (the change of slope) indicate the presence of saturable absorption. Saturable absorption occurs when the drive current is in between the threshold current and the current where kink occurs. The kink is pushed to the higher level (towards high current and high light power) when the reverse bias increases. This means the upper current limit for saturable absorption can be increased by increasing the reverse bias applied on the absorber section.

### 4.2.2 Spectra broadening due to self-pulsation

In order to study the influence of self-pulsation on the spectrum, the spectra have been measured under self-pulsing and non self-pulsing conditions. Figure 4.7 shows the room temperature spectra measured under these conditions.

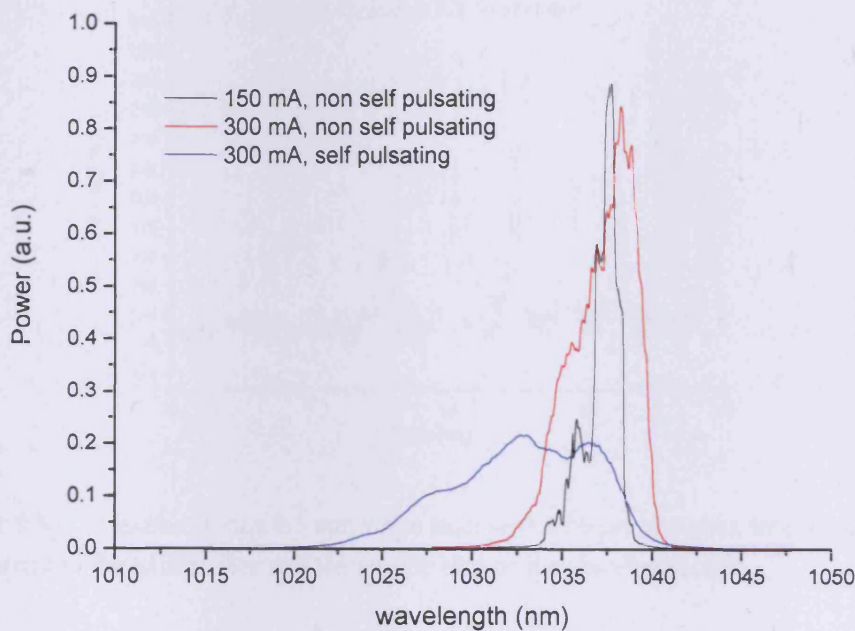


Figure 4.7 Spectra of a 0.5 mm stripe with 50  $\mu\text{m}$  absorber when the device is driven pulsed: pulse rate 5 kHz, pulse length 1  $\mu\text{s}$

We can see the blue curve (self pulsed by applying 3 V reverse bias on the absorber) shows a broader spectrum than the black and red curves (non self pulsating). More devices have been measured to confirm the broadening effect. Results show the same trends.

### 4.2.3 Streak camera measurements

In order to ensure that the broadening is due to the self pulsation, the output of the laser device has been coupled to a streak camera setup as described in chapter 2. Figure 4.8 and Figure 4.9 show the measured results for a 0.5 mm device with 50  $\mu\text{m}$  absorber section under various driving conditions.

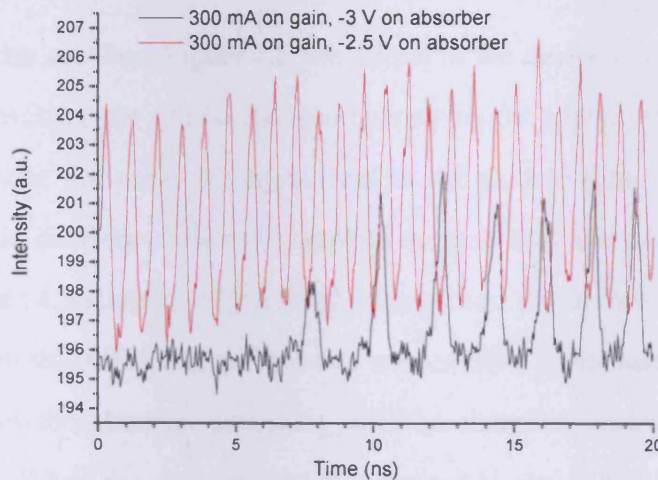


Figure 4.8 Self pulsation from a 0.5 mm stripe laser with a 50  $\mu\text{m}$  absorber, labels indicate the drive current to the gain section and the reverse bias on the absorber section



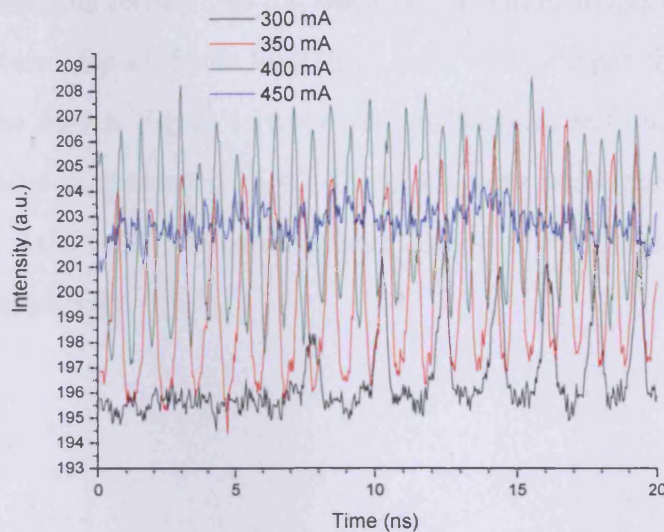


Figure 4.9 Self pulsation from a 0.5 mm stripe laser with a 50  $\mu\text{m}$  absorber, the absorber is reverses biased by  $-3$  V. Labels indicate different drive current to the gain section.

As we can see from Figure 4.8, the output of the device is self pulsed and the pulsation repetition rate can be changed by varying the applied reverse bias on the absorber. Under the same driving current to the gain section, the self pulsation repetition rate decreases when the applied reverse bias increases. On the other hand, as figure 4.9 shows, under a fixed reverse bias, for an increasing in injection current, an increase in the repetition rate occurs. This is because a high injection current makes the absorber saturating quickly, therefore leading to shorter and faster pulses. When the drive current is increased to above 400 mA, no clear self pulsation can be observed. This is because the absorber is not recovering fast enough to maintain the self pulsation. These effects were confirmed with the measurement from multi-section ridge lasers and explained in a rate equation model presented in section 4.4.

#### 4.2.4 Pulse frequency measurement

The change of the self pulsation frequency due to the changing of different

parameters has been recorded by the electronic spectrum analyzer together with a fast photodetector for a 0.5 mm long stripe laser with a 50  $\mu\text{m}$  absorber section at the end of the device. Figure 4.10 shows the change in self pulsation frequency when the device is operated at 15  $^{\circ}\text{C}$ . The black curve shows the frequency when the absorber is 0 V. The red curve and blue curves are for reverse biases of  $-2$  V and  $-3$  V respectively.

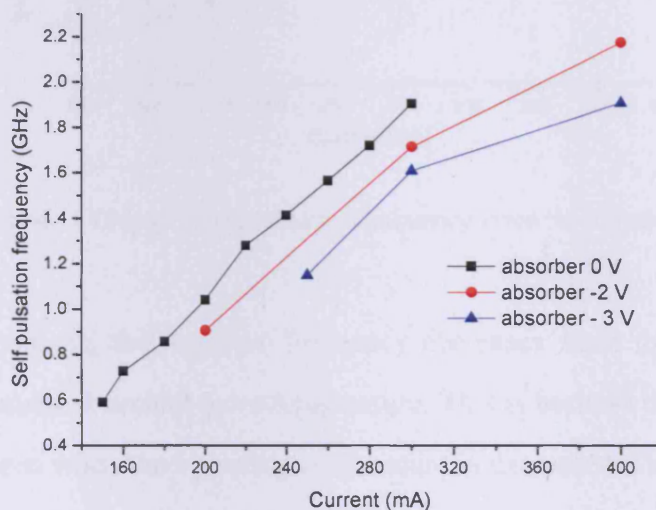


Figure 4.10 Change of self pulsation frequency when the device is operated at 15  $^{\circ}\text{C}$

As we can see, when 0 V is applied on the absorber, the self pulsation rate changes from 0.6 GHz to 1.9 GHz when the drive current to the gain section is increased. Above 1.9 GHz, the self pulsation can not be maintained. When the reverse bias is increased to  $-2$  V, for the same drive current, the self pulsation frequency is decreased. For increasing reverse bias, the range of frequencies for self pulsation is shifted to higher frequencies.

Figure 4.11 shows the range of frequencies obtained when the absorber section is at 0 V and the device is operated at slightly different temperatures.

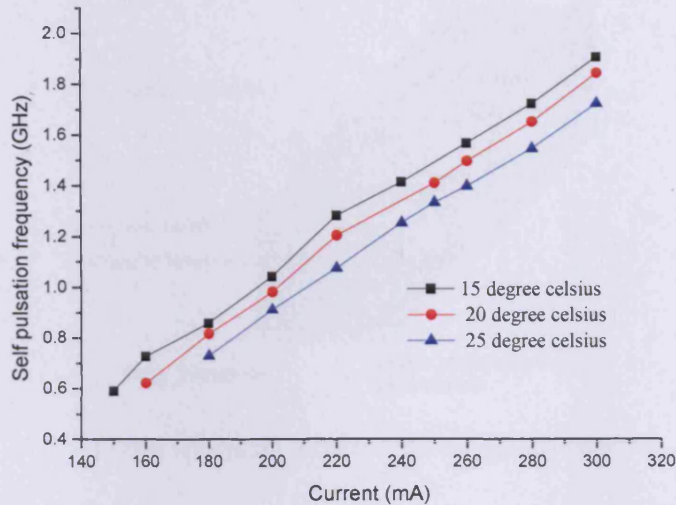


Figure 4.11 Change of self pulsation frequency when the absorber is 0 V

As we can see, the pulsation frequency decreases when the operating temperature increases at around room temperature. This is because the radiative coefficient increases when the operating temperature is decreased. Thus, the pulsation rate at the same drive current is increased.

### 4.3 Multi-section ridge lasers

After successfully testing the principle of operation, multi section ridge waveguide lasers have been fabricated using the material M1963. Figure 4.12 shows the schematic of a multi section ridge waveguide laser (here showing a device with 6 sections). The length of each section is 100  $\mu\text{m}$ . Depending on the length of the device, the device may have 10 sections (for 1 mm device) or 20 sections (for 2 mm device). Sections can be connected by epoxy to make a bigger section and it act as an absorber or gain section.

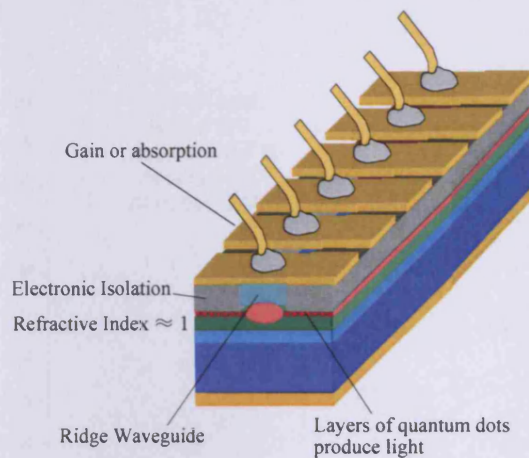


Figure 4.12 Multi section ridge waveguide laser

The ridge has width of  $2\ \mu\text{m}$  and height of  $1.54\ \mu\text{m}$ . Each section has a length of  $100\ \mu\text{m}$  and can be driven individually by either forward or reverse bias. The devices have been tested for different absorber locations and L-I measurement results show no significant differences by varying the absorber location. Results show only the absorber size and the reverse bias applied on the absorber affect the pulsation and lasing spectra. For ease of operation, we would prefer the devices to self-pulsate when the front absorber section is simply grounded rather than reverse biased and by varying the ratios of gain and absorber sections we find the balance of gain: absorption for a  $2\ \text{mm}$  total length device is 17:3. The results shown below are for a  $2\ \text{mm}$  long device with the front three sections ( $0.3\ \text{mm}$ ) operated as an absorber section.

### 4.3.1 Spectra broadening due to self pulsation

In figure 4.13 a plot of the output power versus current is shown for a typical device operated with a pulsed current source, mounted p-side up and with a Peltier controlled heat sink temperature of  $15\ ^\circ\text{C}$  using the setup described in chapter 2. The repetition rate of the current pulse was  $5\ \text{kHz}$  and the pulse length was  $1\ \mu\text{s}$ .

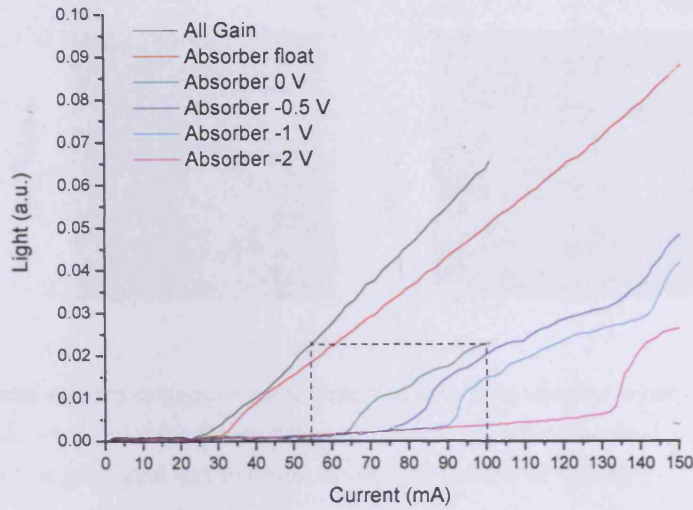


Figure 4.13 Light-current characteristics when the device is driven by pulsed current

In order to observe the self-pulsation and the spectral broadening simultaneously, the laser output was coupled into a streak camera system as described in chapter 2. Figure 4.14 shows the streak camera image of light observed in a 5 ns window when (a) the device is operated with all sections under forward bias of 55 mA, (b) when the device is operated with the absorber section grounded and a current to the gain section of 100 mA. As indicated on figure 4.13, the light outputs under these two operations have the same optical power. When all sections are forward biased, there are two main discrete modes and one lesser intensity mode. However when the device is operated with the absorber section earthed, a single, broader and continuous lasing spectrum is observed. On the time axis we observe continuous emission when the device is operated with all sections under forward bias that becomes self pulsating with the absorber under reverse bias.

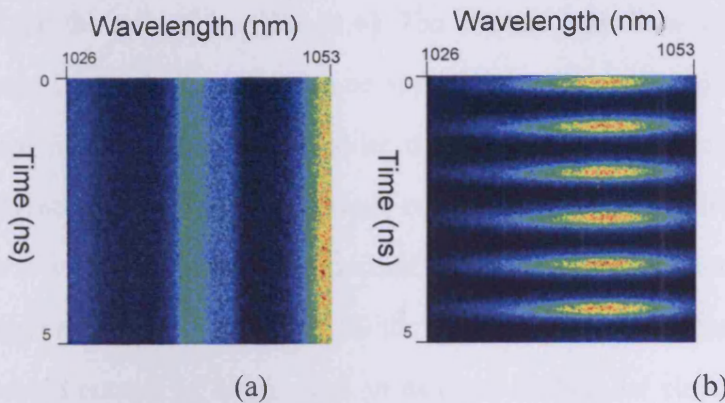


Figure 4.14 streak camera images of light observed in a 5 ns window when (a) the device is operated with all sections under forward bias of 55 mA, (b) when the device is operated with the absorber section grounded and a current to the gain section of 100 mA.

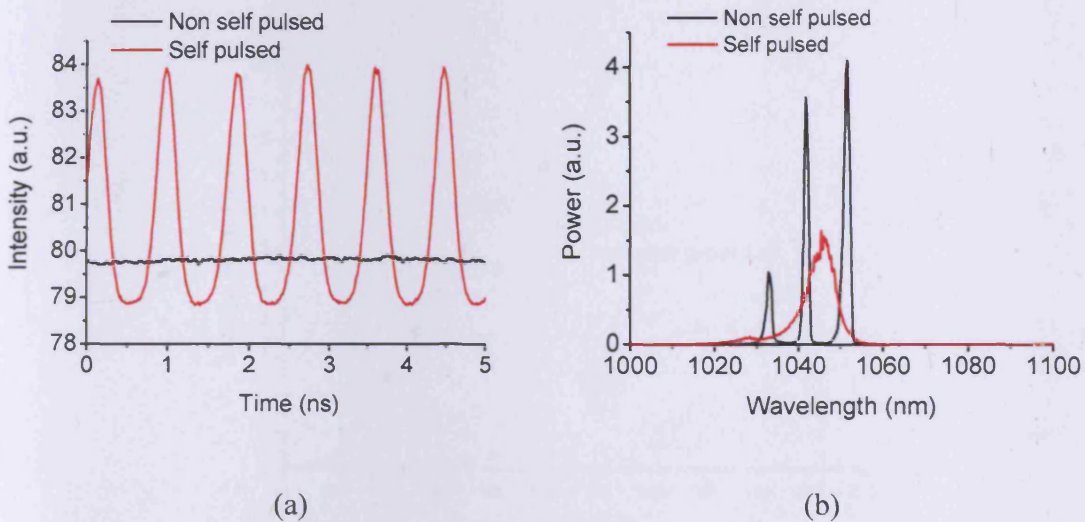


Figure 4.15 (a) light intensity in a 5ns window when the device is operated non self pulsed (all gain) and self pulsed (absorber grounded) (b) spectrum when the device is operated non self pulsed and self pulsed.

Figure 4.15 shows the corresponding light intensity changes and the optical spectra. The pulse duration is measured to be  $\sim 270$  ps, and the pulse repetition rate is 1.2 GHz. With all sections pumped with a forward bias, the multiple peaks in the output spectra, which are separated by  $\sim 10$  nm (larger than the longitudinal mode spacing which is 0.07 nm), are groups of modes originating from the sub-

strate leakage and the reflection effect [4.4]. The discrete narrow modes merge to form a broad continuous lasing spectrum on application of the saturable absorber.

The device has also been tested under continuous drive current operation. Figure 4.16 shows the output power versus current characteristics for the same device operated with continuous drive current and with a Peltier controlled heat sink with a temperature of 15 °C. When all the sections are forward biased the laser has a threshold current of 20 mA and an external differential slope efficiency of 0.24 W/A. With the absorber section earthed the threshold current increases to 110 mA and the slope has a rapid initial rise, typical of devices with a saturable absorber, followed by an external differential slope efficiency of 0.11 W/A.

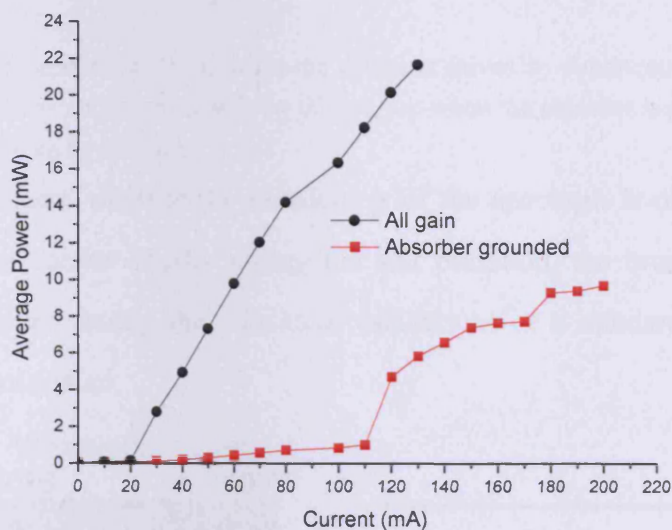


Figure 4.16 Light-current characteristics at 15 °C when the device is driven by continuous current

Figure 4.17 shows the lasing spectra corresponding to the conditions of figure 4.16 for an optical output power of  $\sim 7.5$  mW in each case. The necessary current increases from 50 mA to 150 mA but the spectrum changes from narrow discrete modes, when all sections are forward biased, to a broad continuous lasing

spectrum ( $\sim 10$  nm at Full width half maximum), and centered at around 1050 nm, when the absorber sections are grounded.

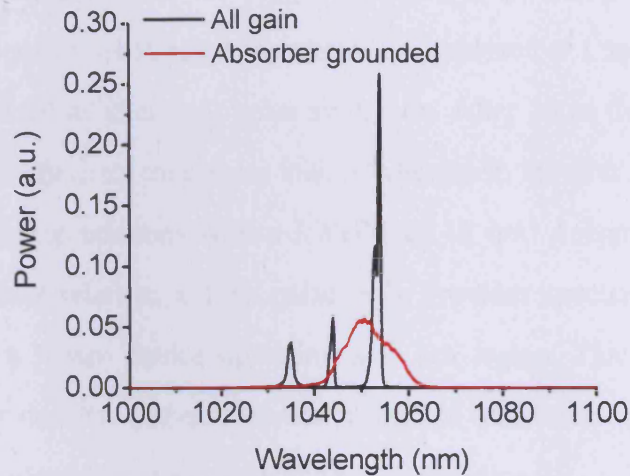


Figure 4.17 lasing spectra at 15 °C when the device is driven by continuous current, Black: when all the sections are driven as gain by 50 mA, red when the absorber is grounded and the gain section is driven by 100 mA

To investigate whether the broadening of the spectrum is obtained due to changes in the carrier density during the self pulsation, the broadening of the spectrum obtained during the relaxation oscillations of a standard quantum dot laser were investigated.

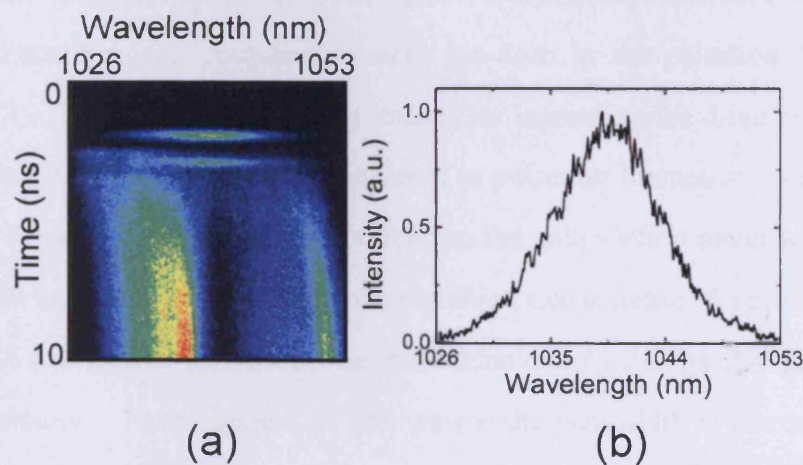


Figure 4.18 (a) Streak camera image of light observed in a 10 ns window (first 10 ns of the light pulse) for a standard single section ridge laser. (b) The normalized spectrum of the first pulse

As shown in figure 4.18, a 1 mm long single section ridge waveguide laser, driven using a pulsed source (pulse length 1  $\mu$ s and repetition rate 5 kHz) at 80 mA was examined. The streak camera was triggered to look at the first few ns of the light pulse. 1 ns sections of the streak camera trace are analysed at 1 ns after light pulse switch on and at 10 ns after light pulse switch on. After 10 ns the carrier density has stabilised and discrete modes are visible whereas in the first few ns the spectrum is broad and continuous with a FWHM of 12 nm. According to the time bandwidth product relation, a 1 ns pulse only provides spectral broadening of 0.0004 nm for a 1 mm device operating at 1  $\mu$ m region. This suggests that a changing carrier density, that also occurs during the relaxation oscillations, is the cause of the broadened spectrum seen under self pulsation.

### 4.3.2 Drive current, reverse bias and temperature effects on self-pulsation

The self-pulsation oscillation frequency is controlled by the response times of the electron and photon populations and the rate of carrier injection into the gain region of the device. As the pumping rate of the laser is altered, changing the system dynamics, corresponding changes are seen in the pulsation frequency. Figure 4.19 shows the streak camera images for increasing the drive current. For an increase in injection current, an increase in pulsation frequency occurs. Figure 4.20 (a) shows when injection current on the gain section increases from 80 mA to 100 mA and then to 120mA, the repetition rate increases from 0.64 GHz to 1.16 GHz and then to 1.47 GHz. The pulse durations are 310 ps, 270 ps, and 310 ps respectively. From figure 4.20 (b), we see the bandwidth is increased when the injection current increases.

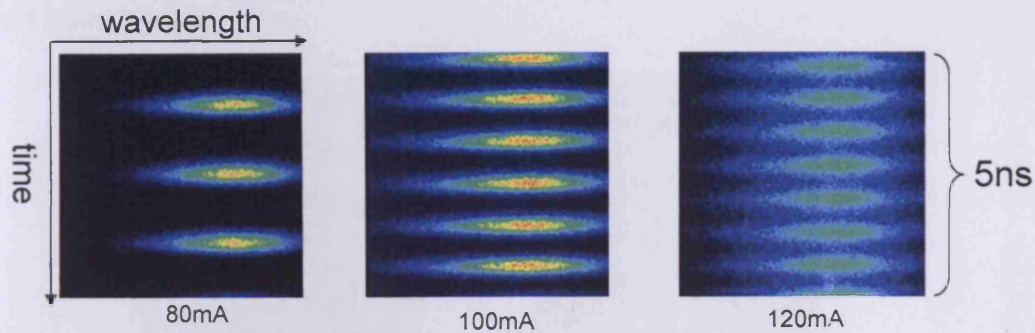


Figure 4.19 streak camera images when the device is driven at different currents

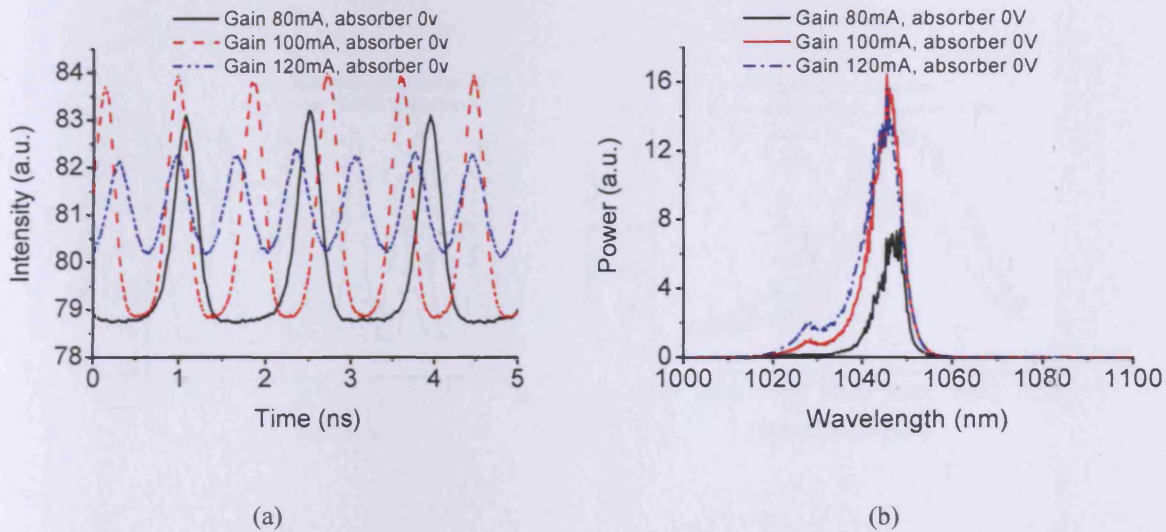


Figure 4.20 (a) self pulsation frequency varied by injection current (b) spectra under different self pulsation

Applying a reverse bias to the device has the effect of aiding the removal of carriers from the quantum dot states, thus decreasing the absorber recovery time. This however will actually increase the time for the absorber to be saturated if the current to the gain section is kept at the same level. Thus we should see a decrease in repetition rate and an increase in pulse length occurring. Figure 4.21 shows the streak camera images when the device is driven at same current but with different reverse bias on the absorber. Figure 4.22 shows the corresponding pulsation rate

and lasing spectra.

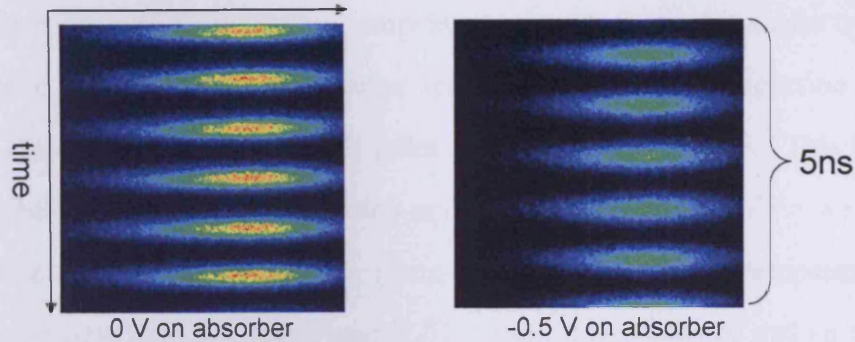


Figure 4.21 Streak camera images when the gain section is driven at same current but the absorber with different reverse bias

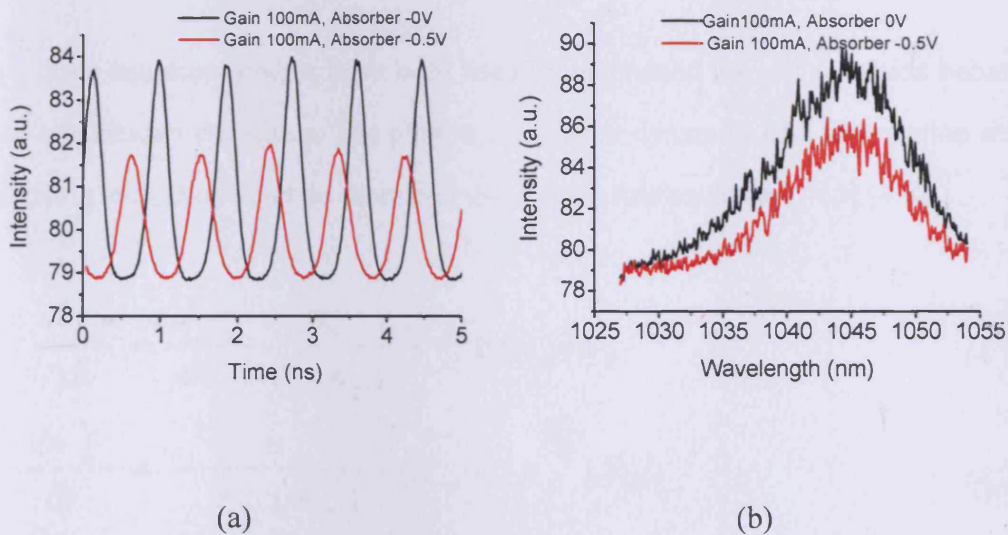


Figure 4.22 (a) self pulsation frequency varied by reverse bias on absorber (b) spectra under different reverse bias

As we can see from figure 4.21 and figure 4.22 (a), the pulse repetition rate decreases when the applied reverse bias increases. The repetition rate is decreased from 1.16 GHz to 1.12 GHz, and the pulse length is increased from 270 ps to 337 ps. Figure 4.22 (b) shows the spectra from individual pulses, we see that shorter pulse (black curve which is 270 ps) has broader spectrum than the longer pulse (red curve which is 337 ps).

A change of self pulsation is observed when the operating temperature is varied. This is because the operating temperature changes both the carrier dynamics in the gain section and in the absorber section. By varying the injection current, we are able to make the device self pulse at different temperatures. This gives us the flexibility to broaden the emission at different wavelengths when we operate the device at different temperature (long wavelength at higher temperature and shorter wavelength at low temperature). The results are presented and an explanation is discussed with a rate equation model in the following section.

#### 4.4 Rate equation simulation of self pulsation

Rate equation models have been used to understand the self pulsation behaviour of quantum dot lasers. The photon and carrier dynamics of a two-section self pulsating laser diode can be described using three rate equations [4.5] [4.6].

$$\frac{dn_g}{dt} = \frac{J_g}{eh} - \frac{n_g}{\tau_g(n_g)} - v_g g(n_g) S_g \quad (4.1)$$

$$\frac{dn_\alpha}{dt} = - \frac{n_\alpha}{\tau_\alpha(n_\alpha)} - v_g g(n_\alpha) S_\alpha \quad (4.2)$$

$$\frac{dS}{dt} = v_g (f_g g(n_g) + f_a g(n_\alpha) - \alpha_0) S + \beta B n_g^2 \quad (4.3)$$

Electrons are defined to be located in the active region of the sample. The active region contains quantum dots layers as well as wetting layers. Electrons density is considered as an average value over the whole active region. The active region is defined by the mode profile of the fabricated sample (ridge device fabricated using M1963). Equation (4.1) describes the carrier dynamics in the gain section; the

carrier density ( $n_g$ ) is supplied by the current injection to the gain section ( $\frac{J_g}{eh}$ ) and depleted by the non-radiative emission, spontaneous emission ( $\frac{n_g}{\tau_g(n_g)}$ ) and the stimulated emission ( $v_g g(n_g)S_g$ ). Equation (4.2) describes the carrier dynamics in the absorber section, the carrier density ( $n_a$ ) is depleted by non-radiative emission, spontaneous emission ( $\frac{n_a}{\tau_a(n_a)}$ ) and is increased by the stimulated absorption ( $v_g g(n_a)S_a$ ), because the carrier density  $n_a$  in the absorber section is below the transparent point, this will provide a negative gain, i.e absorption. Equation (4.3) describes the photon dynamics in the whole cavity. Photons are generated by the spontaneous emission ( $\beta B n_g^2$ ) and stimulated emission ( $v_g f_g g(n_g)S$ ) in the gain section, and depleted by the stimulated absorption ( $v_g f_a g(n_a)S$ ) in the absorber section; it is also depleted by the total loss ( $\alpha_0$ ) of the cavity. The symbols are defined as follows:  $n_g$  and  $n_a$  is the carrier density in the gain section and in the absorber section respectively.  $J_g$  is the current density to the gain section.  $h$  is the active region thickness,  $e$  is the electric charge.  $v_g$  is the group velocity of the light in the cavity. The gain section extends along a fraction  $f_g$  of cavity and the absorber section extends along the remaining fraction  $f_a$  of the cavity.  $g(n_g)$  is the modal gain in the gain section (using the measured modal gain for M1963), and  $g(n_a)$  is the modal gain (M1963) in the absorber section (in this case the negative modal gain, so actually the modal loss).  $\alpha_0$  is the combination of the mirror losses  $\alpha_m$  (calculated us-

ing the mirror reflectivity) and the internal losses  $\alpha_i$  (measured from experiment, see chapter 3 for details) in the laser cavity.  $\beta$  is the fraction of spontaneous emission coupled into the lasing mode and B is the bimolecular radiative coefficient.  $\tau_g(n_g)$  and  $\tau_a(n_a)$  is the carrier lifetime in the gain section and absorber section respectively and is defined as :

$$\tau_g(n_g) = \frac{1}{A_g + Bn_g} \quad (4.4)$$

$$\tau_a(n_a) = \frac{1}{A_a + Bn_a} \quad (4.5)$$

where  $A_g$  and  $A_a$  are the non-radiative recombination rate in the gain section and in the absorber section respectively. The carrier life time is decided by the non-radiative recombination term and the radiative recombination term. For simplicity, the effect of Auger recombination, which may not be a significant mechanism in these quantum dot lasers, is not included. The photon density in the gain ( $S_g$ ) and absorber ( $S_a$ ) sections are related to the mean photon density in the whole cavity ( $S$ ) using the cavity round trip resonance condition (see detailed derivations in the appendix 1):

$$S_a = \frac{S}{f_a \left( 1 + \frac{-\gamma_a (1 - e^{-\gamma_g L f_g}) (e^{-\gamma_a L f_a} + R \cdot e^{(\gamma_g L f_g + \gamma_a L f_a)})}{\gamma_g (e^{-\gamma_a L f_a} - 1) (1 + R \cdot e^{\gamma_a L f_a})} \right)} \quad (4.6)$$

$$S_g = S_a \frac{-\gamma_a f_a (1 - e^{-\gamma_g L f_g}) (e^{-\gamma_a L f_a} + R \cdot e^{(\gamma_g L f_g + \gamma_a L f_a)})}{\gamma_g f_g (e^{-\gamma_a L f_a} - 1) (1 + R \cdot e^{\gamma_a L f_a})} \quad (4.7)$$

where R is the reflectivity of the facet, L is the total length of the cavity and  $\gamma_a$  and  $\gamma_g$  are give by

$$\gamma_{\alpha} = g(n_{\alpha}) - \alpha_0 \quad (4.8)$$

$$\gamma_g = g(n_g) - \alpha_0 \quad (4.9)$$

The measured peak modal gain versus current density and modal loss versus current density have been formularised using a linear approximation. To use the data in the simulation, the current density is related to the carrier density through the following equation:

$$J = \frac{neh}{\tau_g(n)} \quad (4.10)$$

where  $J$  is the drive current density used to measure the gain,  $n$  is the corresponding carrier density.  $e$  is the electronic charge,  $h$  is the active region thickness.  $\tau_g(n)$  is the carrier life time. Other parameters used in the modelling are selected according to the real structure of our self pulsating laser. They are shown in table 4.1.

Parameter	Parameter symbol	Value	Unit
Drive current density	$J_g$	Varied	A/m <sup>2</sup>
Active region thickness	H	0.1455*10 <sup>-6</sup>	m
Length of the device	L	2*10 <sup>-3</sup>	m
Gain section fraction	F <sub>g</sub>	0.85 (can be varied)	
Absorber section fraction	F <sub>a</sub>	0.15 (can be varied)	
Fraction of spontaneous emission coupled into the lasing mode	$\beta$	10 <sup>-4</sup>	

Bimolecular radiative coefficient	B	$10^{-16}$	$\text{m}^3/\text{s}$
Non-radiative coefficient (gain section)	$A_g$	$3 \cdot 10^9$ (varied)	/s
Non-radiative coefficient (absorber)	$A_a$	$\sim 3 \cdot 10^9$ (varied)	/s
Mirror reflectivity	R	0.32	
Group velocity of the light in the cavity	$v_g$	$0.75 \cdot 10^8$	m/s
Internal losses	$\alpha_i$	1500	/m
Total losses	$\alpha_0$	$\sim 2070$	/m

Table 4.1 Parameters used in simulations

The rate equations are solved numerically using Mathcad. The detailed codes are presented in the appendix 2. The simulation results show that the general trends of the variation of pulsation due to changes in different parameters are consistent with the experimental results. Simulations also show the similar threshold current values as well as the self pulsation rate compared to the experimental results. This suggests the simulations are suitable for explaining the examined self pulsation behaviour of our device.

#### 4.4.1 The conditions for self pulsation

Early theoretical work showed that self-pulsation was a natural operating mode of the nonlinear, coupled electron-photon system, and could be produced by optical feedback via saturable absorption within the laser cavity [4.7]. Among other research [4.8, 4.9], they stated that for self-pulsation to occur, the modulus of the differential gain in the absorber region has to be greater than that in the gain region:

$$\frac{d\alpha}{dN} \geq \frac{dg}{dN} \quad (4.11)$$

This expression assumes that any changes in the absorber section caused by the photon field in the gain section occur instantaneously. However, the carrier lifetime in each section is finite and so this instantaneous change cannot occur. Henry [4.10] showed a more complete condition which involves the influence of the carrier life times as the following inequality:

$$\frac{1}{\tau_\alpha} + \nu_g \frac{d\alpha}{dN} P > \frac{1}{\tau_g} + \nu_g \frac{dg}{dN} P \quad (4.12)$$

where  $\tau_\alpha$  and  $\tau_g$  are the carrier lifetime in the absorber and gain region respectively.  $\nu_g$  and  $P$  are the group velocity and density of photons respectively.

The differential gain in the gain and absorber regions are represented by  $\frac{dg}{dN}$  and  $\frac{d\alpha}{dN}$ . The quantum dot device used for the self pulsation experiments has a greater differential loss than the differential gain (see measured peak modal gain/loss from figure 3.16). In the simulation, the carrier lifetime in the absorber section and in the gain section are defined separately (see equation 4.4 and 4.5). It varies by the change of carrier density in each section. By varying the reverse bias on the absorber section, we effectively change the non radiative coefficient ( $A_\alpha$ ) in the absorber section, hence vary the carrier life time in the absorber region. This causes a change in self pulsation. By varying the operation temperature of the device, we effectively change the non radiative coefficient in both the absorber section ( $A_\alpha$ ) and the gain section ( $A_g$ ) and this varies the carrier life time in both regions. Therefore, it changes the self pulsation of the device. By varying the driving current to the gain section, we effectively change the rate of saturation in the absorber; therefore vary the self pulsation of the device.

### 4.4.2 The effect of driving current

To understand the effect of the drive current on the self pulsation, simulations have been performed with different drive currents to the gain section. The parameters are set as:  $A_g = 3 \cdot 10^9 (s^{-1})$ ,  $A_a = 3 \cdot 10^9 (s^{-1})$ ,  $fg = 0.85$ ,  $fa = 0.15$ , other parameters are same as described in table 4.1. This is equivalent to the situation when the absorber section is grounded (no reverse bias) and the gain section is driven by the current. The driving current to the gain section was varied from below the threshold to above the threshold then to well above the threshold. Simulation shows the device from non-lasing to self pulsating lasing then to non-self pulsating lasing. The results are shown in the following figures.

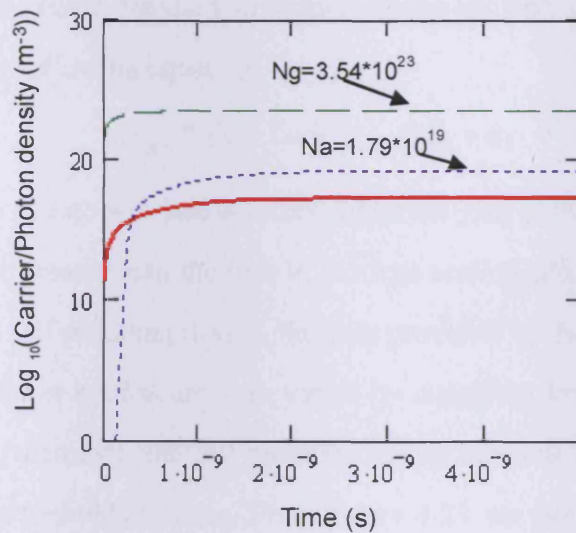


Figure 4.23 Simulation result for  $I = 0.085$  A. carrier density and photon density in a 5 ns window in logarithm scale. Green: carrier density in the gain region. Blue: carrier density in the absorber section, red: photon density.

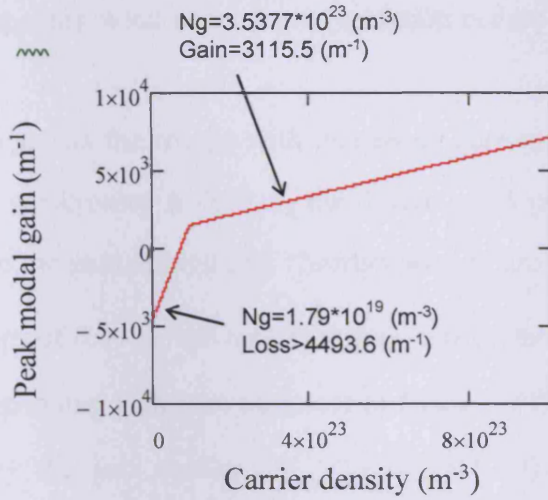


Figure 4.24 The gain versus carrier density for the quantum dot material (M1963), the labels show the corresponding carrier density in figure 4.23 and their gain/loss value.

For lasing to occur, the gain of the device must be equal or greater than the total loss of the device, for the two section device the threshold condition can be described in the following equation:

$$G_{gain} * f_g \geq Loss_{absorber} * f_a + a_0 \quad (4.13)$$

This means the device will lase at a time when the gain provided by the gain section is equal or greater than the loss in the loss section plus the total loss of the device. For the self pulsating device, the gain provided by the gain section and the loss in the absorber section are both varied by changing the carriers in each section with time, therefore, the self pulsation lasing behaves like a series of lasers with different thresholds in time. From figure 4.23 we can see the gain section carriers are provided by the drive current, the spontaneous emission occurs due to the carriers supplied in the gain section, the absorber absorbs the light, the carrier density in the absorber then increases. However, as we can see from figure 4.24, the gain provided by the gain section ( $G_{gain} * f_g = 3115 * 0.85 = 2647 \text{ (m}^{-1}\text{)}$ ) is less than the total absorption ( $Loss_{absorber} * f_a + a_0 = 4493 * 0.15 + 2070 = 2743 \text{ (m}^{-1}\text{)}$ );

there is no lasing, only weak spontaneous emission occurs (red curve in the figure).

Figure 4.25 shows the results with increasing current. When the current to the gain section is increased to 0.09 A, the device emits pulses of light, and the carrier density in the gain section and absorber section are also changed periodically. At a current of 0.09 A, the corresponding carrier density is  $N = 3.74 \times 10^{23} \text{ (m}^{-3}\text{)}$ , the corresponding gain (can be found in figure 4.24) is:  $3241.2 \text{ (m}^{-1}\text{)}$ . The gain provided by the gain section ( $G_{gain} * f_g = 3241.2 * 0.85 = 2755.02 \text{ (m}^{-1}\text{)}$ ) is greater than the total maximum absorption ( $Loss_{absorber} * f_a + a_0 = 4500 * 0.15 + 2070 = 2745 \text{ (m}^{-1}\text{)}$ ), the maximum loss of the absorber is when there are no carriers in the absorber).

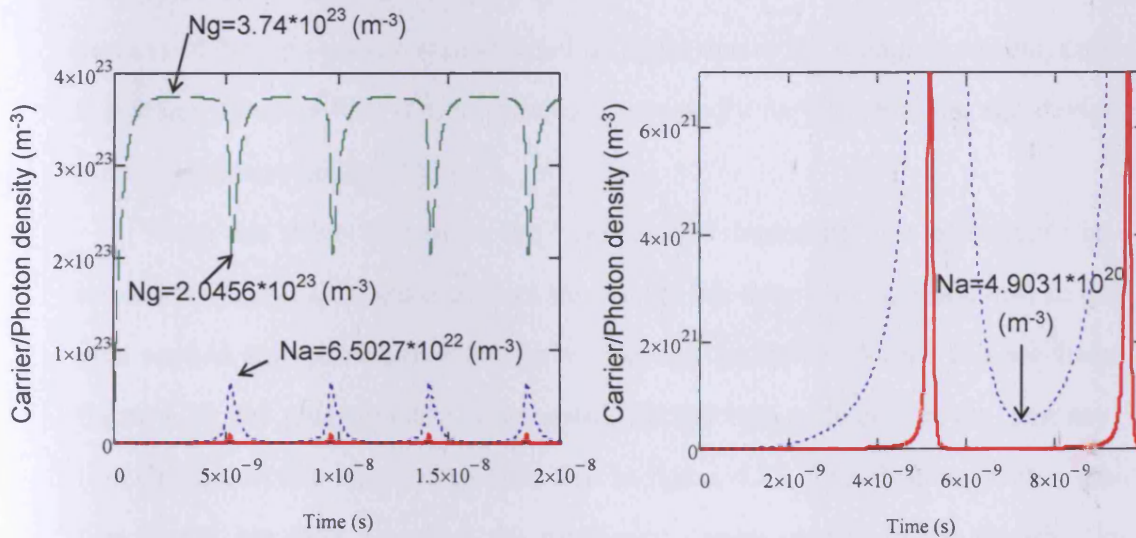


Figure 4.25 Simulation result for  $I = 0.09\text{A}$ . left: carrier density and photon density in a 20 ns window, right: carrier density and photon density in a 10 ns window. Green: carrier density in the gain region. Blue: carrier density in the absorber section, red: photon density. Labels show the corresponding carrier density values.

The carriers in the gain section are provided by the drive current, these carriers ensure that the gain section emits spontaneous photons, light is then absorbed

by the absorber section, and the carrier density in the absorber section is then increased due to the absorption of light. The absorption of the absorber section is then reduced. Because the differential loss is greater than the differential gain, for a fixed number of carriers, the reduction of the gain is less than the reduction of the loss; therefore, the process builds up the overall gain. As the increased stimulated emission consumes the carriers in the gain section, the gain is reduced until the gain is less than the total loss. (Note: here the absorber is not saturated even when it reaches the maximum carrier density of  $N_a = 6.5027 \cdot 10^{22} \text{ (m}^{-3}\text{)}$ , the loss is  $346 \text{ (m}^{-1}\text{)}$  instead of  $0 \text{ (m}^{-1}\text{)}$ , this remaining loss acts as the internal loss, i.e. non-saturated loss). The light intensity starts to decrease and the carrier density in the absorber decreases due to lack of light. The carriers in the absorber section are not decreased to zero because of the spontaneous emission in the gain section. The carriers of the gain section start to build up again due to the pumping current, until it reaches the total loss. These processes repeatedly happen; making the device output a stream of pulsed light.

When the drive current to the gain section increases, this effectively increases the initial gain and decreases the carrier life time (see equation 4.4) in the gain section and hence increases the rate of self pulsation. As we can see from figure 4.26, the pulsation rate is increased and the carrier density in the gain section changes over a larger range than that in figure 4.25. The absorber in this setting is still not fully saturated; the maximum carrier density in the absorber is  $6.83 \cdot 10^{22} \text{ (m}^{-3}\text{)}$ , and the loss is  $135 \text{ (m}^{-1}\text{)}$ .

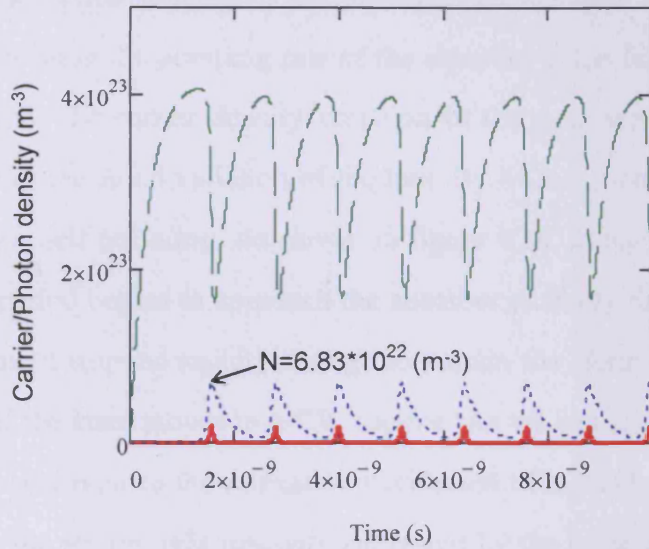


Figure 4.26 Simulation result for  $I = 0.1$  A. Carrier density and photon density in a 10 ns window, Green: carrier density in the gain region. Blue: carrier density in the absorber section, red: photon density. Labels show the corresponding carrier density values.

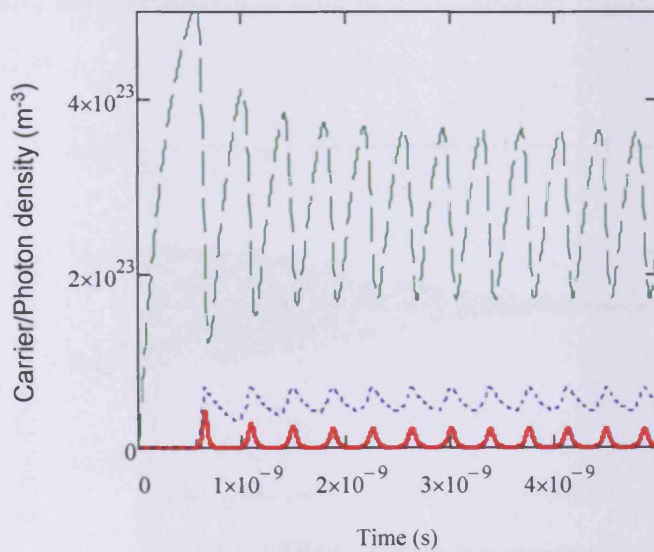


Figure 4.27 simulation result for  $I = 0.15$  A. Carrier density and photon density in a 5 ns window, Green: carrier density in the gain region. Blue: carrier density in the absorber section, red: photon density.

The pulsation rate keeps increasing with increasing drive current to the gain section (see figure 4.27). When the current is 0.15 A, the absorber cannot recover

completely (the carrier density in the absorber section does not return to low level), this is because the pumping rate of the absorber is too fast for the absorber to fully recover. The carrier density variation in the gain section also becomes small because of the small variation of the loss. By further increasing the current, the device stops self pulsating. As shown in figure 4.28, at high injection current the pulsation period begins to approach the absorber recovery time and eventually the system cannot respond rapidly enough to sustain the Henry inequality (equation 4.12), and the laser moves to a CW regime. As we can see from figure 4.28, the behaviour is similar to the relaxation oscillation of a standard laser. It can be understood as the strong light intensity generated by the large current to the gain section bleaches the absorber, and the absorber is too slow to return to the high loss value. If the carrier life time in the absorber section can be controlled to a short time scale, the pulsation will maintain. Simulation results are shown in the following section.

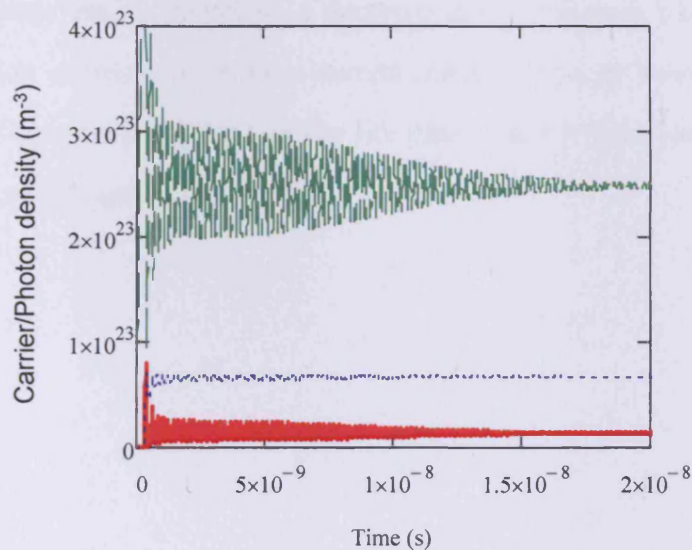


Figure 4.28 simulation result for  $I = 0.26$  A. Carrier density and photon density in a 20 ns window, Green: carrier density in the gain region. Blue: carrier density in the absorber section, red: photon density.

### 4.4.3 The effect of reverse bias

The increased reverse bias to the absorber section is effectively equivalent to increasing the non-radiative coefficient of the absorber section and this makes the carrier life time in the absorber section short (see equation 4.5). At the same drive current, it takes more time to saturate the absorber; this effectively decreases the rate of self pulsation. The simulation parameters are the same as in previous section except for the non-radiative coefficient in the absorber section, which is increased to  $A_{\alpha} = 5 * 10^9$  (s<sup>-1</sup>). This is equally to increase the reverse bias on the absorber thus reduce the carrier life time in the absorber. This effectively decreases the time of carriers being swept out. At the same drive current, it then takes longer to saturate the absorber. Therefore the pulsating rate is reduced. As we can see from figure 4.29, the pulsation rate is lower (6 pulses in 10 ns) than in figure 4.26 (8 pulses in 10 ns). The simulation result agrees with the experiments, when the reverse bias is increased, a decrease in the pulsation rate occurs while the gain section is driven at the same current (measured result shown in the figure 4.22). This is because the shorter carrier life time means it takes longer to saturate the absorber, at the same drive current.

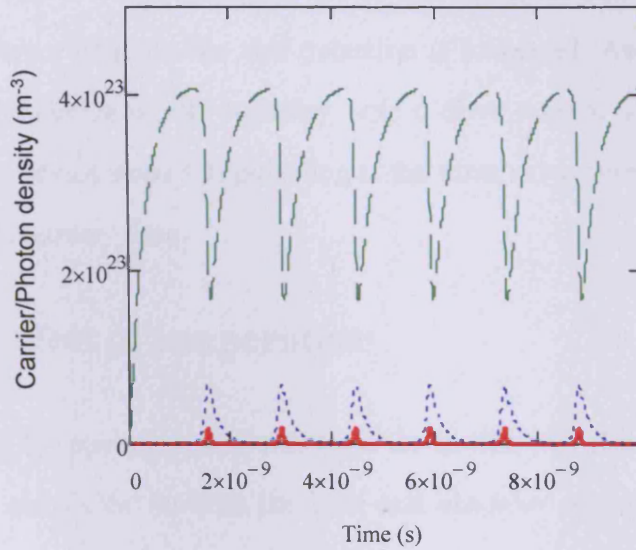


Figure 4.29 simulation result for  $I = 0.1$  A.  $A_{\alpha} = 5 * 10^9$  ( $s^{-1}$ ). Carrier density and photon density in a 10 ns window, Green: carrier density in the gain region. Blue: carrier density in the absorber section, red: photon density.

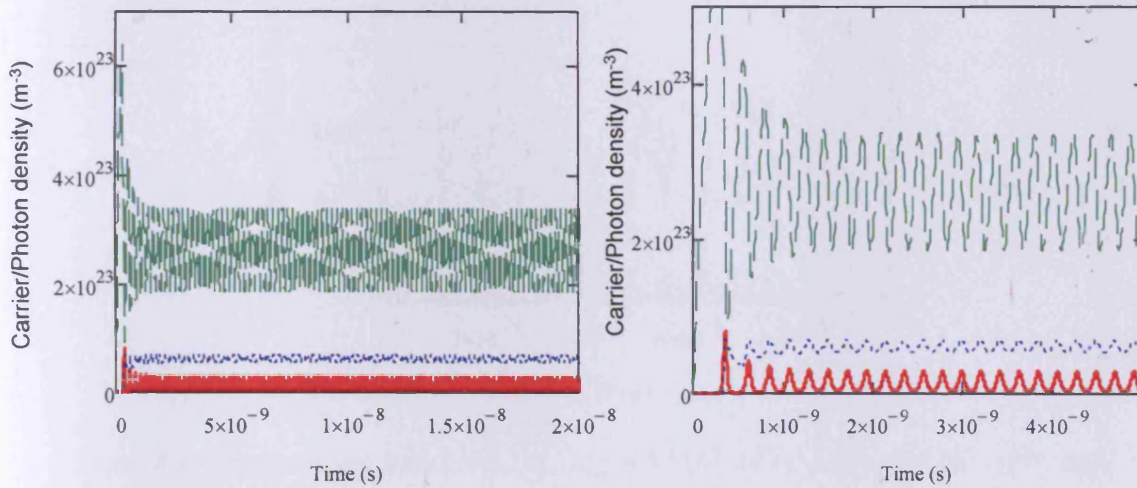


Figure 4.30 simulation result for  $I = 0.26$  A.  $A_{\alpha} = 5 * 10^9$  ( $s^{-1}$ ). Left: carrier density and photon density in a 20 ns window, right: carrier density and photon density in a 5 ns window, Green: carrier density in the gain region. Blue: carrier density in the absorber section, red: photon density.

If the current to the gain section can be increased, the pulsation will become faster. The current limit for the self pulsation is increased. As we can see from figure 4.30, the device is self pulsating with a drive current of 0.26 A while in figure 4.28 the device stops self pulsating at the same drive current because of the slow absorber recovery time.

#### 4.4.4 The effect of temperature

Changing the operating temperature of the device will effectively change the non-radiative coefficient in both the gain and absorber sections. Increasing the temperature will increase the non-radiative coefficient ( $A$ ) and decreasing the temperature will decrease the non-radiative coefficient ( $A$ ).

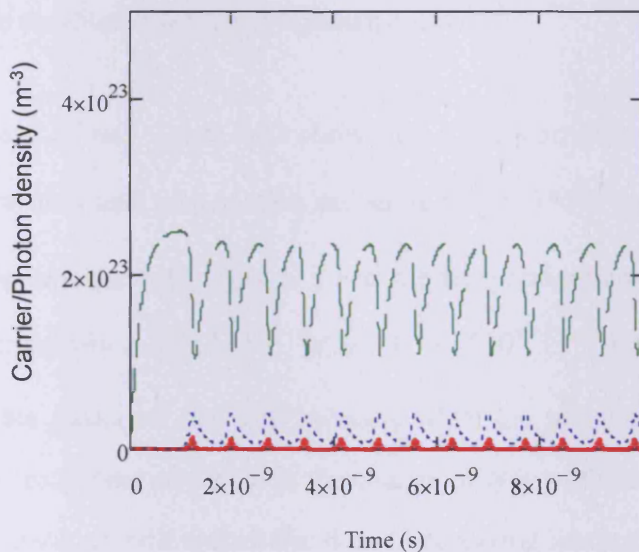


Figure 4.31 simulation result for  $I = 0.1$  A.  $A_a = 5 * 10^9$  ( $s^{-1}$ ),  $A_g = 5 * 10^9$  ( $s^{-1}$ ). Carrier density and photon density in a 10 ns window. Green: carrier density in the gain region. Blue: carrier density in the absorber section, red: photon density.

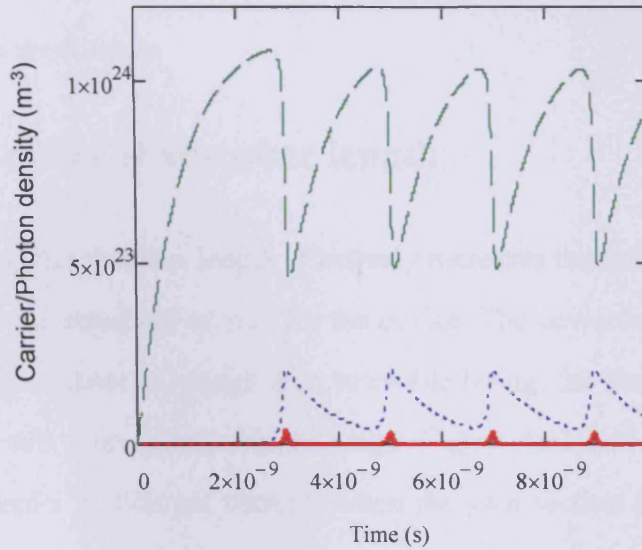


Figure 4.32 simulation result for  $I = 0.1$  A.  $A_{\alpha} = 1 * 10^9$  ( $s^{-1}$ ),  $A_g = 1 * 10^9$  ( $s^{-1}$ ). Carrier density and photon density in a 10 ns window. Green: carrier density in the gain region. Blue: carrier density in the absorber section, red: photon density.

As figure 4.31 and figure 4.32 show that if the non-radiative coefficient in the absorber section and gain section are same ( $A_{\alpha} = 5 * 10^9$  ( $s^{-1}$ ),  $A_g = 5 * 10^9$  ( $s^{-1}$ ) for the simulation in figure 4.31), and the temperature change has the same effect on both sections ( $A_{\alpha} = 1 * 10^9$  ( $s^{-1}$ ),  $A_g = 1 * 10^9$  ( $s^{-1}$ ) for the simulation in figure 4.32), the pulsation rate will increase when the temperature is increased. However, this result does not include the change of gain with temperature change. Increasing temperature will reduce the B and decreasing temperature will increase B. The increased temperature will reduce the gain/loss of the device; the decreased gain will decrease the pulse repetition rate. Hence, the effect of temperature change has no direct linear relationship to the self pulsation. In the experiment, the change in temperature affects the device's self pulsation and the lasing wavelength. In the tested temperature range (15 °C to 25 °C), the self pulsation can be re-established by changing only the driving current to the gain section.

This provides the flexibility to self pulsate the device at different central wave lengths over a small range.

#### 4.4.5 The effect of absorber length

Increasing the absorber length effectively increases the saturable losses. This will increase the threshold current for the device. The device needs more gain to achieve lasing. If there is enough gain to enable lasing, the carrier density in the gain section will change in a bigger range. Figure 4.33 and figure 4.34 show simulation results at different currents when the gain section fraction is 0.8, the absorber section fraction is 0.2. Other parameters are the same as used in section 4.3.2.

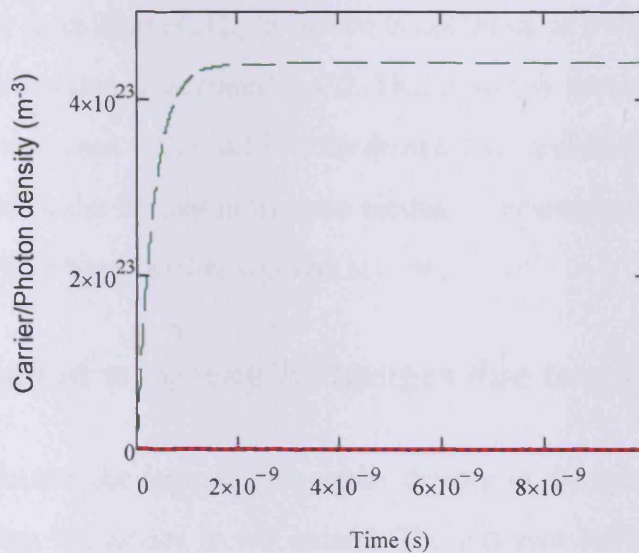


Figure 4.33 simulation result for  $I = 0.1A$ ,  $f_g = 0.80$ . Carrier density and photon density in a 10 ns window, Green: carrier density in the gain region. Blue: carrier density in the absorber section, red: photon density.

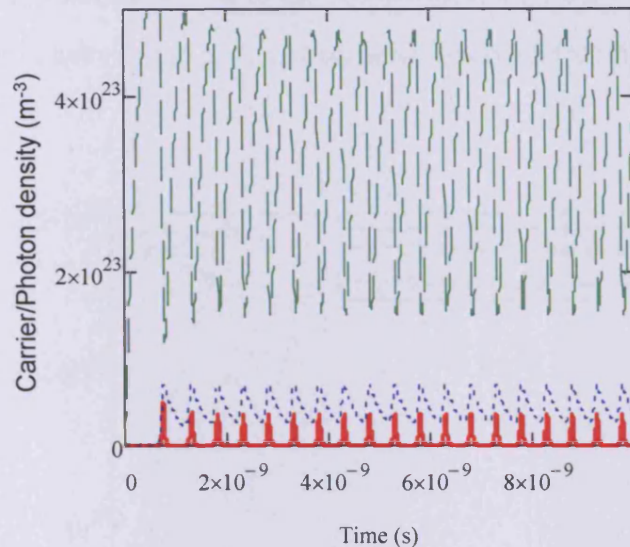


Figure 4.34 simulation result for  $I = 0.15\text{A}$ ,  $fg=0.80$ . Carrier density and photon density in a 10 ns window, Green: carrier density in the gain region. Blue: carrier density in the absorber section, red: photon density.

As we can see from figure 4.33, the device is not lasing at  $I = 0.1\text{ A}$  when the absorber section fraction is increased to 0.2. This is simply because the total loss of the device is increased. At  $I = 0.15\text{ A}$ , the device lases and produces self pulsation. The change of carrier density in the gain section is greater than that shown in the figure 4.27 which has a smaller absorber section.

#### 4.4.6 Emission wavelength changes due to self pulsation

As the results demonstrate, the carrier density in the gain section is varied with time when the device is self pulsed. The different carrier densities correspond to different peak gain at different wavelengths for the quantum dot material. For the range of carrier densities where it is above threshold, the variation in carrier density makes the device emit light at different wavelengths. When the device is operated with no self pulsed operation, the carrier density in the gain section is not changing, and a relatively narrow wavelength range is produced. Figure 4.35

shows a simulated device similar to the one shown in figure 4.15 (b) driven at 150 mA, the carrier density in the gain section periodically varies with time due to self pulsation.

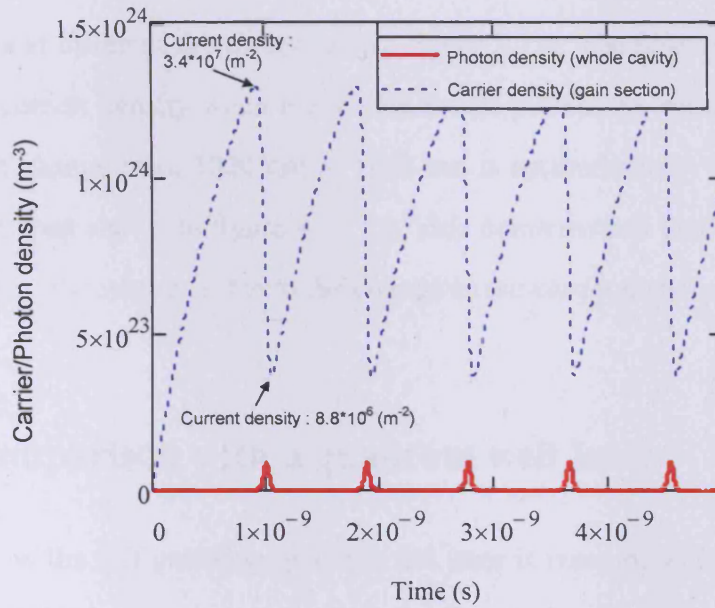


Figure 4.35 the carrier density change in the gain section of a self pulsation device driven at 150 mA. Blue: carrier density in the gain region, red: photon density for the whole cavity. The labels show the corresponding current density.

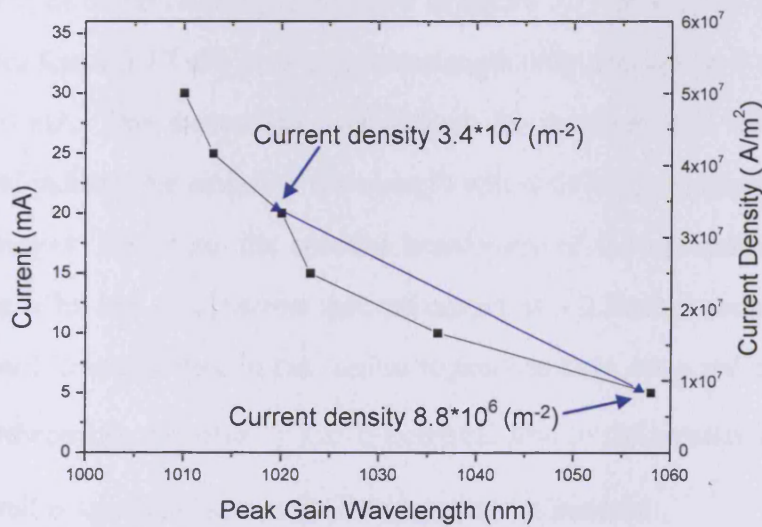


Figure 4.36 the current density change and the corresponding peak gain wavelength

As measured gain curve shown in figure 3.15, the peak gain wavelength varies with the driving current; figure 4.36 shows the corresponding wavelength for the carrier density change in figure 4.35. The black curve shows the peak gain wavelength at different drive current (data points are taken from the measured gain spectra at different drive current, see figure 3.15). The blue curve shows the change of current density when the device is self pulsed. As we can see that the wavelength change from 1020 nm to 1058 nm is approximately the same as the wavelength span shown in figure 4.15 (b). This demonstrated that the broadening of the emission spectrum is due to the change in the carrier density during the self pulsation.

#### 4.4.7 Comparison with a quantum well laser

To show the self pulsating quantum dot laser is more suitable for generating broadband light than a quantum well laser, the modal gain and modal loss of a quantum well material which has emission wavelength around 1  $\mu\text{m}$  has been measured at 15  $^{\circ}\text{C}$ . The measured net modal gain spectra and the peak modal gain as a function of current density are shown in figure 3.17 and figure 3.18. As we can see from figure 3.17, the peak gain wavelength only changes by 5 nm between 60 and 110 mA. This means that even though the quantum well device can be made to self pulsate, the emission wavelength will not change much as the carrier density changes. Therefore, the spectral broadening of the self pulsed quantum well device is limited. The narrow spectral output of  $\sim 2.5$  nm from a self pulsed quantum well laser operated in the similar region has been observed by reference [4.11]. Furthermore, the ratio ( $\gamma$ ) of differential loss to differential gain for the quantum well is smaller than it is for the quantum dot material.

$$\gamma = \frac{d\alpha / dN}{dg / dN} \quad (4.13)$$

For self pulsation to occur, this value must be as large as possible [4.12]. For the quantum well material, this value is: 6.24. For the quantum dot material, this value is 9.46. This shows the quantum dot material is more suitable for realising self pulsation.

## 4.5 Summary and discussion

The self pulsation of the two section laser has been explained through rate equation simulations. For an ideal broadband self pulsation device, the net modal gain spectra need to have different peak wavelengths at different drive current. The modal gain also needs to be broad. When applying the self pulsation, the carrier density change in the gain section needs to be as large as possible. Thus we can have a broadband wavelength output. This can be realised by introducing a large absorber section. An absorber fraction of 0.9 has been tested in the simulation. The device can lase and produce self pulsation at a drive current of 0.58 A. The carrier density in the gain section varies in a very large span. If the gain wavelength varies with carrier density, we will have a very broad spectral output. However, in reality we can not have such a large absorber section, because the gain provided by the gain section is not high enough to conquer the losses. This is because of the gain saturation and the heating problem at high current. The device cannot be driven at significantly high currents since the heating will damage the device. The pulsation rate and pulse duration can be reduced by increasing the reverse bias on the absorber. With a very short carrier life time in the absorber section and a very high current in the gain section, we can have very fast pulses. In the simulation, the non-radiative coefficient was chosen to be very small ( $A_{\alpha} = 10^{12} \text{ (s}^{-1}\text{)}$ ). The device emits very short pulses with very fast repetition rate. This however can not be realised in reality; the reverse bias applied on the ab-

sorber cannot be made extremely large because large reverse bias will damage the device. In the experiment, when increased reverse bias is applied on the absorber, the device temperature increases as well. To reduce this problem, a fast heat dissipation system is needed. In the experiment, when a large reverse bias ( $>7$  V) is applied on the absorber, devices are believed to experience catastrophic optical damage. This could be caused by the very short light pulse with large peak power damaging the mirror facet. This problem could be possibly improved by coating the mirrors or other methods [4.13].

## 4.6 References

- [4.1] Evgeny A. Viktorov, Thomas Erneux, Paul Mandel, Tomasz Piwonski, Gillian Madden, Jaroslaw Pulka, Guillaume Huyet, and John Houlihan, “Recovery time scales in a reversed-biased quantum dot absorber”, *Applied Physics Letters*, Vol. 94, 263502, (2009).
- [4.2] E.A. Avrutin, J.H.Marsh, and E.L. Portnoi, “Monolithic and multi-GigaHertz mode-locked semiconductor lasers: Constructions, experiments, models and applications”, *IEE Proceedings, Optoelectronics*, Vol.147, No. 4, pp.251 - 78, (2000).
- [4.3] Minoru Yamada, “A Theoretical Analysis of Self-sustained Pulsation Phenomena in Narrow-Stripe Semiconductor Lasers”, *IEEE Journal of quantum electronics*, Vol. 29, No. 5, pp. 1330 -1336, (1993).
- [4.4] D.Bhattacharyya, E.A.Avrutin, A.C.Bryce, J.H.Marsh, D. Bimberg, F. Heinrichsdorff, V.M. Ustinov, S.V.Zaitsev, N.N.Ledentsov, P.S.Kop’ev, Zh.I.Alferov, A.I.Onischenko, and E.P.O’Reilly, “Spectral and Dynamic Properties of InAs-GaAs Self-Organized Quantum-Dot Lasers”, *IEEE Journal of selected topics in quantum electronics*, Vol.5, No.3, pp. 648 – 657, (1999).

- [4.5] A. Egan, P. Rees, J. O’Gorman, M. Harley- Stead, G. Farrell, J. Hegary, P. Phelan, “Theoretical investigations of electro-optical synchronisation of self-pulsating laser diodes”, *IEE Proceedings, Optoelectronics*, Vol. 143, No. 1, pp. 31 - 36, (1996).
- [4.6] A. Owen, P. Rees, I. Pierce, D. Matthews and H.D. Summers, “Theory of Q-switching in a quantum-dot Baser diode”, *IEE Proceedings, Optoelectronics*, Vol. 150, No. 2, pp. 152 -158, (2003).
- [4.7] G. J. Lasher, “Analysis of a proposed bistable injection laser”, *Solid-State Electronics* Vol. 7, No. 10, pp.707 – 716, (1964).
- [4.8] Richard W. Dixon, William B. Joyce, “A possible mode for sustained Oscillations (Pulsations) in (Al,Ga)As Double-Heterostructure Lasers”, *IEEE Journal of Quantum Electronics*, Vol. 15, No. 6, 15, pp. 470 - 474, (1979).
- [4.9] Ueno, Masayaso and Lang, Roy, “Conditions for Self-Sustained Pulsation and Bistability in Semiconductor Lasers”, *Journal of Applied Physics*, Vol. 58, No. 4, pp.1689 -1692, (1985).
- [4.10] Henry, C. H., “Theory of defect – induced pulsations in semiconductor injection lasers”, *Journal of applied physics*, Vol. 51, No. 6, pp.3051 – 3062, (1980).
- [4.11] Daniel Matthews, “The influence of wetting-layer states on the properties of InGaAs quantum dot lasers”, PhD thesis, Cardiff University, 2003.
- [4.12] H.D.Summers, P.Rees, “Experimental investigation of the differential gain in semiconductor lasers and its influence on Q-switching performance”, *Applied physics letters*, Vol. 69, No. 14, pp. 2009 - 2011, (1996).
- [4.13] D.A. Livshits, I.V. Kochnev, V.M. Lantratov, N.N. Ledentsov, T.A. Nalyot, I.S. Tarasov and Zh.I. Alferov, “Improved catastrophic optical mirror damage level in InGaAs/AlGaAs laser diodes”, *Electronics letters*, Vol.36, No.22, pp. 1848 – 1849, (2000).

# **Chapter 5 Measurements of other light sources**

## **5.1 Introduction**

In this chapter results obtained on a super luminescent light emitting diode (SLD) light sources provided by Exalos and an EC project are reported to give an idea of the relative performance of different approaches and to give some further information on the light source properties that are necessary to achieve useful images. In terms of construction, a SLD is similar to a laser diode which contains an electrically driven p-n junction and an optical waveguide. However, unlike a laser diode, SLDs are designed to have high single pass amplification for the spontaneous emission generated along the waveguide. There is insufficient feedback to achieve lasing action. The feedback is suppressed by tilting the facets relative to the waveguide and can be suppressed further with anti-reflection coatings. The emission peak wavelength and the intensity of the light emitted from the SLD depend on the active material composition and on the level of current injection.

## **5.2 Exalos SLD measurements**

Two different types of SLD devices with central emission around 1050 nm have been tested. To avoid reflection, one of the devices has a tilted waveguide. The structure of that device is shown in figure 5.1.

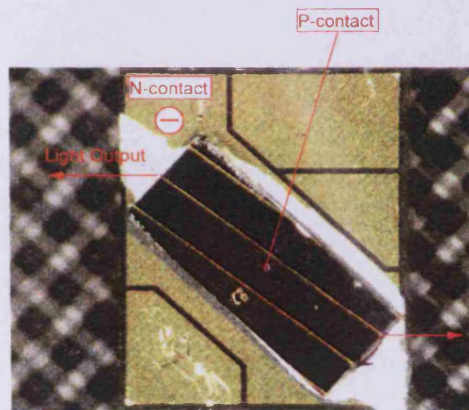


Figure 5.1 Structure of a tilted waveguide SLD

The optical feedback into this waveguide is reduced through tilting of the ridge waveguide by  $12^\circ$ . The light incident on the facets gets partially transmitted and partially reflected outside the waveguide where it is absorbed by the unbiased regions of the device. The spectral output and the power of the device have been measured using the setup described in chapter 2. The emission spectra are shown in figure 5.2 and the output power versus drive current is shown in figure 5.3.

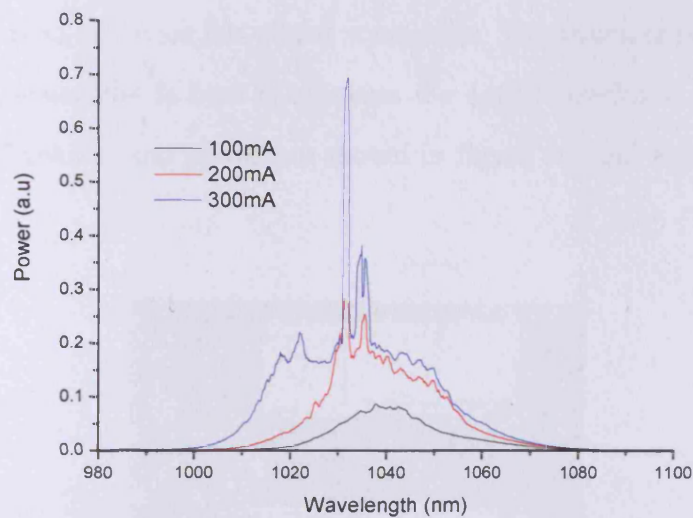


Figure 5.2 Measured Spectra of tilted waveguide SLD

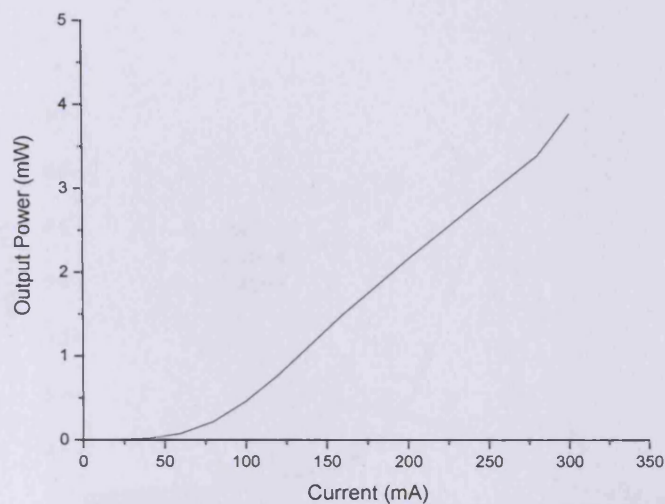


Figure 5.3 Output power of the tilted waveguide SLD

As we can see from figure 5.2, when the device is driven at high current (300 mA), the optical feedback can not be sufficiently suppressed; There is a strong emission peak at  $\sim 1030$  nm. The device may lase at this current. The output power of the device is also not considered sufficient for OCT applications as shown in figure 5.3.

The 2nd type of device has a bent waveguide. The structure is shown in figure 5.4. The waveguide is bent to suppress the optical feedback of the mirrors. The measured spectra and power are shown in figure 5.5 and figure 5.6 respectively.

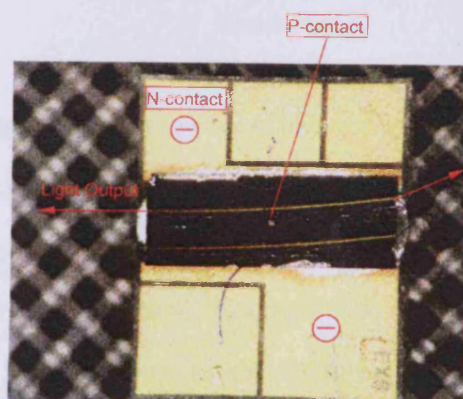


Figure 5.4 Structure of bent waveguide SLD

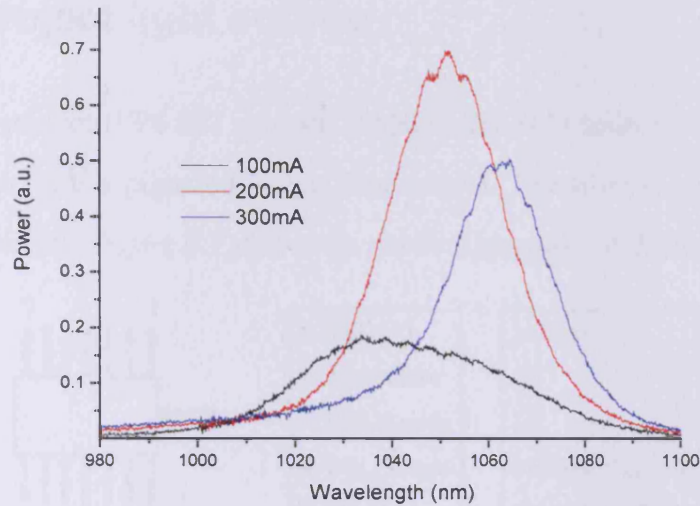


Figure 5.5 Measured Spectra of bent waveguide SLD

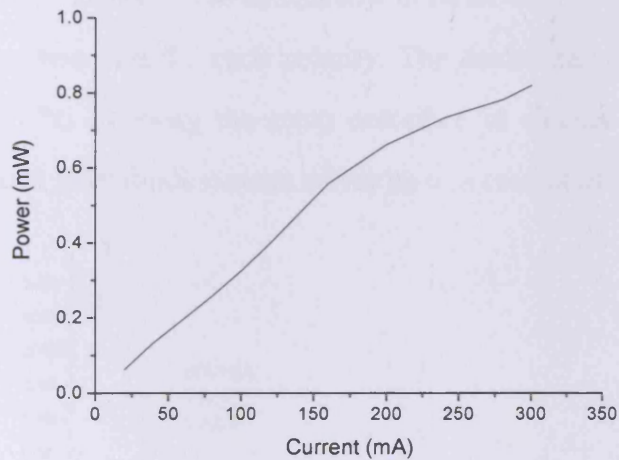


Figure 5.6 Output power of bent waveguide SLD

As we can see from figure 5.5, this structure has a better suppression of the optical feedback; the emission spectra are Gaussian like and have bandwidth of  $\sim 25$  nm at FWHM. However as shown in figure 5.6, the output power is too weak for OCT applications. This L-I is measured by manually changing the current applied to the device. There are no data points below 20 mA because the light signal

below 20 mA is too small.

### 5.3 EC project light source

The EC project (FP6 IST project, NANO-UB) SLD source tested has a butterfly package with a pigtailed single fibre output. The fibre is equipped with a FC/APC connector. Figure 5.7 shows the pin configuration of the device.

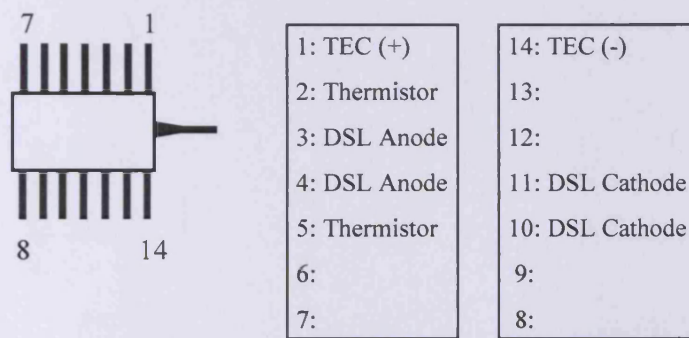


Figure 5.7 Pin configuration of the EC SLD

The SLD has two pins for each polarity. The device has been operated at a temperature of 15 °C by using the setup described in chapter 2. The device is driven by a constant laser diode current driver up to a current of 1.42 A.

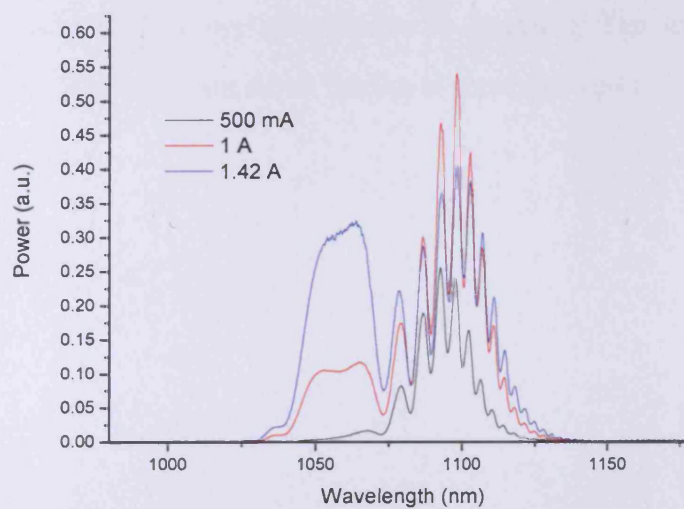


Figure 5.8 Spectra with strong feedback

Figure 5.8 shows the spectra measured under different currents. As we can see from the figure there are strong ripples. The mode separation is 6 nm; this indicates a cavity length of 29  $\mu\text{m}$ . The cavity length of the SLD is much longer than 29  $\mu\text{m}$ . This indicates the modes are caused by feedback due to mismatched connectors. The feedback can be weakened by the increase in the return losses. This is achieved by making loops of  $\sim 2$  cm in diameter with the fibre.

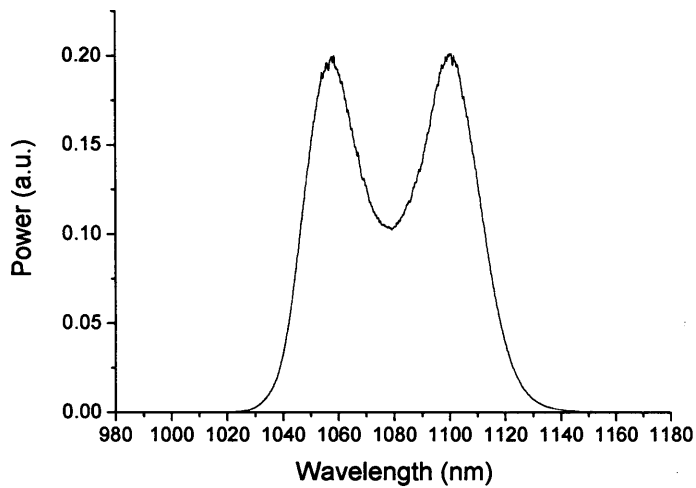


Figure 5.9 Spectrum measured at 1.42 A with fibre loops

Figure 5.9 shows the spectrum measured with two fibre loops. As we can see from the figure, a smooth shape of the spectrum is obtained. The measured optical power from the fibre end versus drive current is shown in figure 5.10.

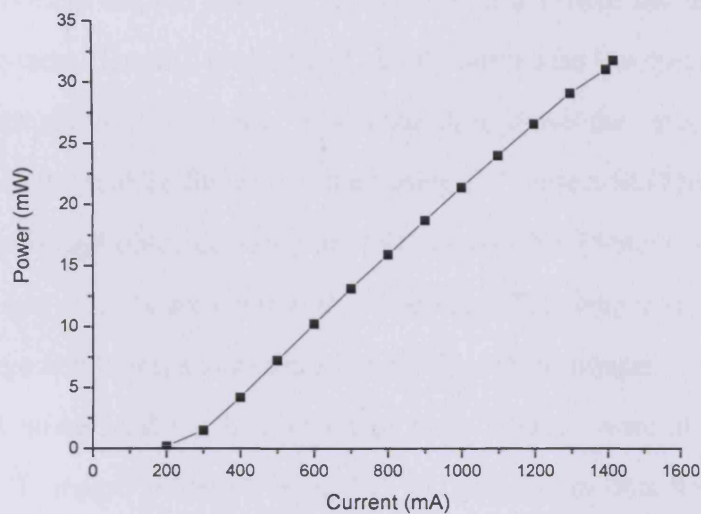


Figure 5.10 End fibre power output

The device has a bandwidth of  $\sim 65$  nm and optical power of 31 mW. This device has been interfaced to the existing OCT system and the images of my retina have been obtained and shown in figure 5.11 (b). For comparison, OCT images obtained using an 800 nm light source is shown in figure 5.11 (a).

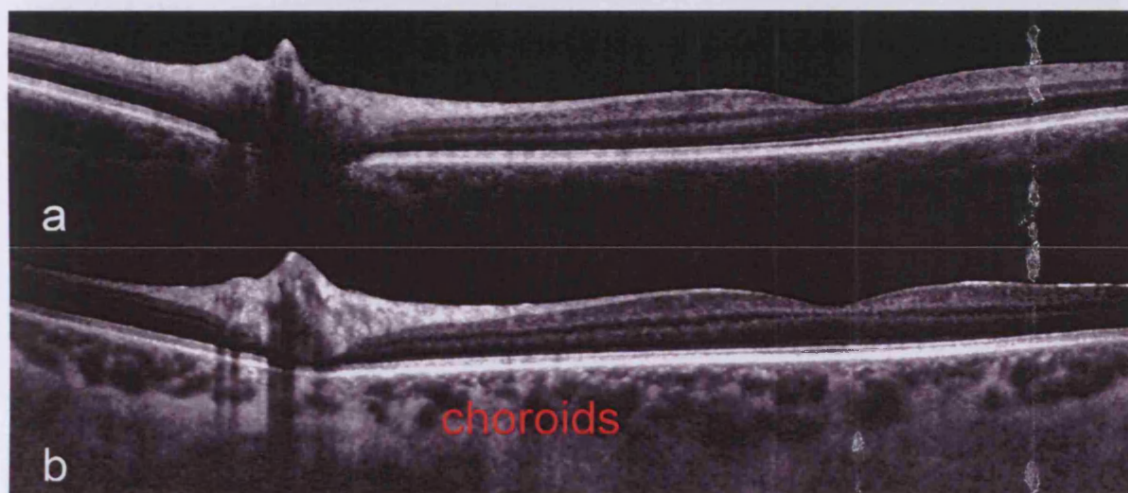


Figure 5.11 in-vivo OCT images of human retina. a. Measured by using 800 nm light source. b. Measured by using 1060 nm EC project SLD

We can clearly see the choroids in the 1060 nm system but hardly see it in the 800 nm system. The EC project SLD light source also has been tested to image the human skin. OCT images of human skin above the proximal interphalangeal joint of the middle finger obtained using EC project SLD have been compared with the image obtained using an ASE source (NP Photonics, Tucson, Arizona). Both light sources are centred at  $\sim 1060$  nm. The images are shown in figure 5.12. Image resolution and penetration depth of these images were comparable as the output power and the bandwidth of these sources were almost identical. However, OCT images obtained using EC SLD (quantum dots based SLD) displayed less speckle noise (speckle noise is the granular noise that can be seen in the images). The structures can be seen with higher clarity in (a) due to its reduced speckle noise. The image was also devoid of any ringing artifacts (see artifact on figure b for comparison), arising due to the polarization mismatch between the arms of the Michelson interferometer [5.1].

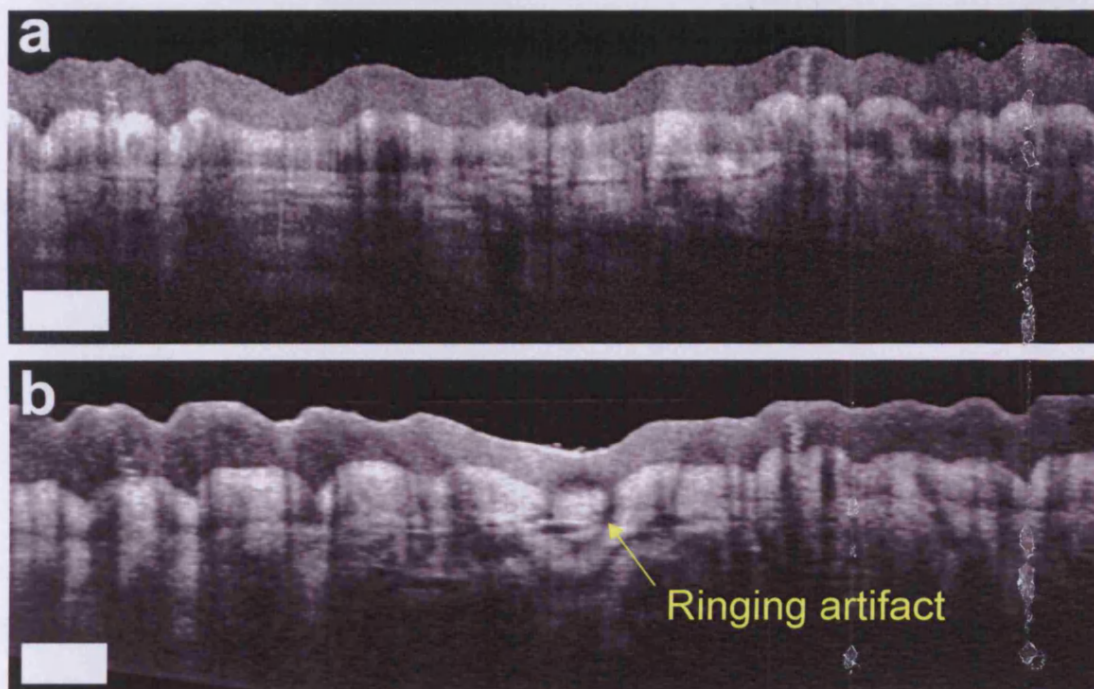


Figure 5.12 OCT images of human skin above the proximal interphalangeal joint of the middle finger obtained at 1060 nm using (a) quantum dot SLD and (b) amplified spontaneous emission light source.

## 5.4 Discussions and Summary

As the results show above, the bandwidth and power requirements of the EC SLD are sufficient to obtain useful clinical images. Comparing to the fibre based ASE source, the quantum dots SLD also show less noise. However, for practical clinic applications, SLD techniques still encounter two main drawbacks [5.2]:

1. *Current “spike” damages SLD much easier than laser diode.*

The reason for this is the non-uniform distribution of drive current inside the active region of the SLD. Because of the low efficiency operation to achieve the required power, the SLD is normally driven at very high current (1.4 A for the EC project SLD), the higher the SLD current, the higher the fraction near the crystal facet. Therefore, a current spike will mainly flow through the areas near the crystal facet, and this will additionally increase the probability of damage with respect to laser diodes. Latent damage near the crystal facet, is the reason for extra reflection and may not affect the SLD power considerably but may strongly increase the SLD spectral ripple and makes device non-useable;

2. *Minor optical feedback may easily result in fatal SLD damage especially if SLD is powerful.*

It would be ideal if the spectral shape is Gaussian as the width of the coherence function is limited by the Fourier uncertainty relation, which says that the product of the variances of a Fourier transform pair reaches its minimum for Gaussian functions [5.3]. Therefore, in the majority of cases a Gaussian power spectrum is desirable. During the imaging process, the output spectrum of the EC SLD has been reshaped using a mathematical method [5.1]. There were not any visible artifacts due to the double peaks of the EC SLD spectrum.

The power and bandwidth of the EC SLD are reached to obtain useful OCT

images. For improvement of the OCT image, spectral shape needs to be Gaussian to reduce the processing time, and the SLD lifetime needs to be prolonged. The bandwidth of the device may be further broadened as broader bandwidth provides higher resolution. Higher power will also help to improve the image quality. However, for work with the eye, there is a limit for the maximum power that can be used as discussed in chapter 1. For dermatological applications, this limit is not critical. It will be useful if the output power of the EC SLD can be increased.

## **5.5 References**

- [5.1] Aneesh Alex, “Multispectral and Multimodal Three-dimensional Optical Coherence Tomography”, PhD thesis, Cardiff university, (2010).
- [5.2] Vladimir Shidlovski, “Superluminescent Diodes- Short overview of device operation principles and performance parameters”, SuperlumDiodes Ltd, 2004.
- [5.3] A F Fercher, W Drexler, C K Hitzenberger and T Lasser, “Optical coherence tomography – principles and applications ”, *Reports on Progress in Physics*, Vol. 66, p. 239, (2003).

# Chapter 6 Summary and further work

## 6.1 Summary

The work in this thesis analysed and discussed the requirements of new light sources for the state of art OCT applications. Result in chapter 5 shows that a compact, economic broadband light source centred at  $\sim 1050$  nm is very important for the next generation ophthalmic OCT applications. Using the EC project SLD as a benchmark, the ideal semiconductor light source will need to have a bandwidth of  $\sim > 70$  nm and have a Gaussian shape. The output power from the fibre should be greater than 30 mW. Although, the bandwidth and the power requirement are reached to obtain useful clinical image (see figure 5.11), for practical clinic applications, the SLD technique however encounters drawbacks as discussed in chapter 5. Such as: 1) Current “spike” damages in SLDs occur much easier than in laser diodes. 2) Minor optical feedback may easily result in fatal SLD damage especially if the SLD is powerful. Furthermore, the spectrum shape of the EC SLD is not Gaussian and this requires extra signal processing time to obtain the OCT image.

As an alternative method to SLD, quantum dot lasers have been proposed as a broadband light source. Self-assembled QD lasers can have a low threshold current density and a low temperature sensitivity of the threshold current as originally suggested in reference [6.1]. Compared to quantum well lasers, self-assembled QD lasers have naturally inhomogeneously broadened gain spectra due to differences in the size and shape of the individual dots [6.2]. The QD laser diode output can therefore be tuned over a wide wavelength range [6.3]. Laser diodes fabricated from different quantum dot materials have been tested for the broadband emission at  $\sim 1050$  nm. The results are summarised below.

### 6.1.1 Broadband emission centred at ~ 1050 nm

- InGaAs dot layers capped with GaAs well layers have central emission wavelength at ~ 1050 nm. InGaAs dots layers capped with  $\text{Al}_{0.15}\text{Ga}_{0.85}\text{As}$  well layers have central emission wavelength at ~ 1000 nm.
- The multiple uncoupled dot layer (InGaAs dots with GaAs/ $\text{Al}_{0.15}\text{Ga}_{0.85}\text{As}$  wells) system has a broader emission (~15 nm) than the multiple coupled dot layer system (InGaAs dots with GaAs wells). This is because for the uncoupled dot layer, each InGaAs dot layer is not electronically coupled with each other, as the InGaAs (dot layer) /GaAs (Well layer) pair is separated by high energy  $\text{Al}_{0.15}\text{Ga}_{0.85}\text{As}$  barrier (see table 2.1). Each layer may lase independently at different wavelengths. Thus, all the dot layers collectively provide a broad emission spectrum. The examined multiple uncoupled dot layer laser has a bandwidth ~ 15 nm at FWHM for a 0.5 mm device.
- For the multiple coupled dot layer system (InGaAs dots with GaAs wells), more layers do not lead to increased inhomogeneous broadening but less inhomogeneous broadening. This is because the very thin GaAs layer (7 nm) between the dot layers, where the upper layer dots are grown on seed potentials formed by lower layer dots, this results in size averaging in the lateral direction. Therefore, the inhomogeneous broadening is reduced. The laser with 7 repeated coupled dots layer has a bandwidth of ~ 5 nm at FWHM while the laser with 5 repeated coupled dot layer has a bandwidth of ~ 6 nm at FWHM.
- The central emission wavelength of the device can be controlled over a

small range ( $\sim 10$  nm) by varying the device length (see figure 3.13, figure 3.14). Shorter devices have emission at shorter wavelengths while longer devices have emission at longer wavelengths. This is because the peak modal gain wavelength shifts to the shorter wavelength when the drive current density is increased. For a shorter device, the threshold current density will be higher, therefore the device emits at a shorter wavelength.

### 6.1.2 Self pulsation and spectra broadening

The self pulsation technique has been proposed and examined as a method to further explore the broad gain bandwidth of the quantum dot material. Self pulsation has been achieved on both wide area stripe and ridge waveguide laser structures by configuring the devices with split contacts. Part of the device has been driven by forward bias to provide gain; part of the device has been driven by reverse bias to act as a saturable absorber. The spectral broadening effects have been observed for both stripe and ridge samples:

- For stripe samples, the devices have a broader spectrum when operated self pulsed compared to when operated in a non-self pulsed mode. At 300 mA, under the non self pulsation operation, the bandwidth of the spectrum is  $\sim 3$  nm. Under the same conditions, the bandwidth of the spectrum is  $\sim 12$  nm when it is operated in a self pulsed mode.
- For the ridge waveguide devices, when operated without a saturable absorber, the laser emits a number of discrete narrow modes, which merge to form a broad continuous lasing spectrum on application of the saturable absorber. The spectral width achieved is  $\sim 10$  nm, and the average output power is  $\sim 7.5$  mW. In the time domain, we observe continuous emission that becomes self pulsating, with pulse widths of 200 - 300 ps

and frequency of 0.6 – 1.5 GHz depending on drive current and reverse bias on application of the saturable absorber.

- The broadening of the spectrum is due to the changing carrier density during the self pulsation. This effect has been supported by observing the broadening of the spectrum in the relaxation oscillations of a standard QD laser.

### 6.1.3 Different effects to the self pulsation

A rate equation model has been used for understanding the self pulsation behaviour of the two section devices. The modal gain and modal loss of the M1963 quantum dot material has been measured and used in the simulation.

- Measured data shows that the differential loss is larger than the differential gain which is crucial for self pulsation to occur as discussed in chapter 4.
- The measured data also shows a shift of peak gain wavelength when the drive current is changed. This will cause the device to have a broader wavelength emission when the carrier density of the gain section is changed during self pulsation.

The effects of the drive current, reverse bias and absorber lengths on self pulsation have been examined experimentally as well as using the simulations.

- The increased drive current to the gain section effectively increases the gain provided by the gain section and shortens the carrier lifetime in the gain section, thus increasing the repetition rate of self pulsation.
- The increased reverse bias on the absorber effectively increases the non-radiative coefficient in the absorber section hence shortens the carrier lifetime in the absorber section. Using a fixed drive current to the gain

section, this reduces the repetition rate of self pulsation. With an increased drive current to the gain section, the repetition rate of the self pulsation increases.

- The absorber length determines changes in the amplitude of the carrier density. A longer absorber section leads to a large variation in carrier density during the self pulsation.

### 6.1.4 Comparisons to a quantum well

To compare the self pulsation in quantum dot material with quantum well material, the modal gain and modal loss of a standard quantum well laser lasing at  $\sim 1 \mu\text{m}$  has also been measured. The comparisons are as follows:

- Results show a smaller differential loss/differential gain ratio (6.24) than that for the quantum dot material (9.46). This shows the quantum dot material is more suitable for self pulsation as discussed in chapter 4.
- Furthermore, measured gain spectra from quantum well material do not show a significant shift in the peak gain wavelength when the drive current is varied. Compared to the quantum dot laser, a smaller spectrum broadening effect will happen even when the quantum well device is self pulsed. A narrow spectral output of  $\sim 2.5 \text{ nm}$  from a self pulsed quantum well device is reported in reference [6.4].

In conclusion, results show that quantum dot lasers are more suitable for self pulsation and are more suitable for generating broadband emission than quantum well lasers. Self pulsed quantum dot lasers can be used as an alternative method to SLD to provide compact, economic broad band light source solutions for OCT applications. A simple approach to realise continuous drive current using a TEC system has been performed. The output of the ridge waveguide laser light was coupled into a lensed single mode fibre. For the material examined, based on the

measurement of the modal gain and the simulation, a  $\sim 30$  nm bandwidth may be achieved. If self pulsation can be performed using an intentionally designed quantum dot material for broadband emission, even broader bandwidth may be obtained. The future works which could improve the performance of the self pulsed quantum dot lasers for fast broadband emission are listed below.

## 6.2 Future work

There are some practical limitations for realising broadband self pulsing laser diodes. The catastrophic optical mirror damage limits the peak power generated by the self pulsation device. It has been found that the device can experience catastrophic optical damage when a large reverse bias is applied on the absorber and a large current is applied on the gain section. This damage is caused by the large peak power of the light pulse melting the facet. It has also been observed that the increased reverse bias will increase the device temperature. Ideally, the absorber length needs to be large in order to have a large variation in the carrier density, hence the broadband emission. In reality, the absorber length can not be very large because that the gain section can not be driven at significantly high current to provide enough gain to achieve lasing. As discussed above, several possible improvements are listed:

- Apply self pulsation using materials with multiple quantum dot layers which are intentionally designed for broad band emission.

In order to generate broadband emission, the material gain bandwidth needs to be very broad in the first instance. The dot materials we have examined are existing dot materials in the lab and are not designed for broadband emission. This means that there is not enough gain and gain bandwidth. Specially designed multiple quantum dot layers grown under different conditions may provide higher saturation gain and broader gain bandwidth [6.5, 6.6]. This en-

ables the self pulsed device to have a larger absorber section and the gain section driven at higher currents.

- Enhancing the near field design

The ridge structure examined has a width of 2  $\mu\text{m}$ . The measured mode field diameter for the 1060 nm EC SLD is  $\sim 6 \mu\text{m}$ . Therefore, for future designs, the width of the ridge can be increased to provide more power. This can also narrow the far field of the light emission hence improve the coupling efficiency.

- Coating of the facets

It has been observed that the facet can be damaged using a high reverse bias. This is caused by the high peak power of the light pulse heating the facet. The catastrophic optical damage can be improved by coating the facet. On the other hand, since we are only coupling the output light from one facet of the laser diode, the front facet can be coated with anti reflective and the back facet can be coated with highly reflective coating.

- Improve the cooling system performance.

As discussed above, the increased reverse bias will increase the device temperature. The undissipated heat may damage the device. This heat needs to be dissipated as quickly as possible. This may be improved by using a better quality Peltier with a better thermal electronic temperature controller.

## 6.3 References

- [6.1] Y. Arakawa and H. Sakaki, "Multidimensional quantum well laser and temperature dependence of its threshold current", *Applied physics letters*, Vol. 40, No. 11, p. 939, (1982).
- [6.2] L. V. Asryan and R. A. Suris, "Inhomogeneous line broadening and the threshold current density of a semiconductor quantum dot laser", *Semi-*

*conductor science and technology*, Vol. 11, pp. 554 - 567, (1996).

- [6.3] H.S.Djie and B.S.Ooi, X.-M. Fang, Y. Wu, J. M. Fastenau, W. K. Liu, and M. Hopkinson, "Room-temperature broadband emission of an InGaAs/GaAs quantum dots laser", *Optics letters*, Vol. 32, No. 1, pp. 44 - 46, (2007).
- [6.4] Daniel Matthews, "The influence of wetting-layer states on the properties of InGaAs quantum dot lasers", PhD thesis, Cardiff University, 2003.
- [6.5] S.K.Ray, K.M.Groom, M.D.Beattie, H.Y.Liu, M.Hopkinson, and R.A.Hogg, "Broad-band superluminescent light-emitting diodes incorporating quantum dots in compositionally modulated quantum wells", *IEEE photonics technology letters*, Vol. 18, No.1, pp. 58 - 60, (2006).
- [6.6] X.Q.Lv, N.Liu, P.Jin, and Z.G.Wang, "Broadband emitting superluminescent diodes with InAs quantum dots in AlGaAs matrix", *IEEE photonics technology letters*, Vol. 20, No. 20, pp. 1742 - 1744, (2008).

## Appendix A: Derivations for the cavity round trip resonance condition

The equations (4.6) and (4.7) used in the simulations are derived in this appendix step by step. A sketch of a two sections laser cavity is shown in figure A.1

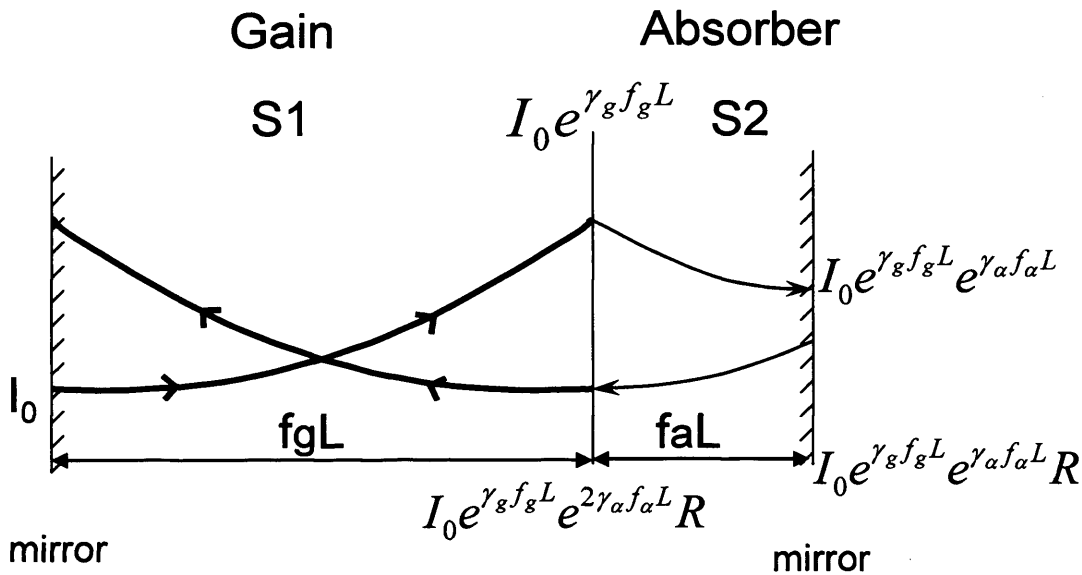


Figure A.1 a laser cavity with an absorber section

$S_1$  represents the total light intensity in the gain section and  $S_2$  represents the total light intensity in the absorber section.  $\gamma_\alpha$  represents the net modal loss and  $\gamma_g$  represents the net modal gain as indicated in equations (4.8) and (4.9).

The intensity  $S_1$  is:

$$S_1 = \int_0^{f_g L} I_0 e^{\gamma_g x} + \int_0^{f_g L} I_0 e^{\gamma_g f_g L} e^{2\gamma_\alpha f_a L} R \cdot e^{\gamma_g x} \quad (\text{A.1})$$

Calculate and rearrange the equation we have:

$$S_1 = \frac{I_0}{\gamma_g} e^{\gamma_g f_g L} (1 - e^{-\gamma_g f_g L}) \cdot e^{\gamma_\alpha f_\alpha L} \cdot (e^{-\gamma_\alpha f_\alpha L} + R \cdot e^{\gamma_g f_g L + \gamma_\alpha f_\alpha L}) \quad (\text{A.2})$$

For the absorber section, from figure A.1, we have:

$$S_2 = \int_0^{f_\alpha L} I_0 e^{\gamma_g f_g L} \cdot e^{\gamma_\alpha x} + \int_0^{f_g L} I_0 e^{\gamma_g f_g L} e^{\gamma_\alpha f_\alpha L} R \cdot e^{\gamma_\alpha x} \quad (\text{A.3})$$

Calculate and rearrange the equation we have:

$$S_2 = \frac{I_0}{\gamma_\alpha} e^{\gamma_g f_g L} (1 - e^{-\gamma_\alpha f_\alpha L}) \cdot e^{\gamma_\alpha f_\alpha L} \cdot (1 + R \cdot e^{\gamma_\alpha f_\alpha L}) \quad (\text{A.4})$$

Divide equation (A.2) by equation (A.4), we have:

$$\frac{S_1}{S_2} = \frac{-\gamma_\alpha (1 - e^{-\gamma_g f_g L}) (e^{-\gamma_\alpha f_\alpha L} + R \cdot e^{\gamma_g f_g L + \gamma_\alpha f_\alpha L})}{\gamma_g (e^{-\gamma_\alpha f_\alpha L} - 1) (1 + R \cdot e^{\gamma_\alpha f_\alpha L})} \quad (\text{A.5})$$

The photon density in the gain section is related to the  $S_1$  by:

$$S_1 = S_g f_g L \quad (\text{A.6})$$

The photon density in the absorber section is related to the  $S_2$  by:

$$S_2 = S_a f_a L \quad (\text{A.7})$$

Substitute S1 and S2 with equation (A.6) and (A.7), we have:

$$S_g = S_a \frac{-\gamma_a f_a (1 - e^{-\gamma_g L f_g})(e^{-\gamma_a L f_a} + R \cdot e^{(\gamma_g L f_g + \gamma_a L f_a)})}{\gamma_g f_g (e^{-\gamma_a L f_a} - 1)(1 + R \cdot e^{\gamma_a L f_a})} \quad (\text{A.8})$$

The photon density in the gain section ( $S_g$ ) and the photon density in the absorber section ( $S_a$ ) are related to the mean photon density of the cavity ( $S$ ) by :

$$S_g f_g L + S_a f_a L = SL \quad (\text{A.9})$$

Substitute  $S_g$  with equation (A.8), we have:

$$S_a = \frac{S}{f_a \left[ 1 + \frac{-\gamma_a (1 - e^{-\gamma_g L f_g})(e^{-\gamma_a L f_a} + R \cdot e^{(\gamma_g L f_g + \gamma_a L f_a)})}{\gamma_g (e^{-\gamma_a L f_a} - 1)(1 + R \cdot e^{\gamma_a L f_a})} \right]} \quad (\text{A.10})$$

## Appendix B: Mathcad code for the simulation

This function defines the carrier life time

$$\tau(N) := \begin{cases} A \leftarrow 3 \times 10^9 \\ B \leftarrow 10^{-16} \\ \text{carrierT} \leftarrow \frac{1}{A + B \cdot N} \\ \text{return carrierT} \end{cases}$$

This function converts carrier density to current density

$$c(N) := \begin{cases} e \leftarrow 1.6 \cdot 10^{-19} \\ h \leftarrow 0.1455 \cdot 10^{-6} \\ \text{current} \leftarrow \frac{N \cdot e \cdot h}{\tau(N)} \\ \text{return current} \end{cases}$$

This function describes the modal gain/loss vs current density

$$g(N) := \begin{cases} \text{if } c(N) > 6.6 \cdot 10^6 \\ \left| \begin{array}{l} a \leftarrow 8.66 \cdot 10^{-5} \\ b \leftarrow 951 \end{array} \right. \\ \text{otherwise} \\ \left| \begin{array}{l} a \leftarrow 9.13 \cdot 10^{-4} \\ b \leftarrow -4500 \end{array} \right. \\ \text{gain} \leftarrow a \cdot c(N) + b \\ \text{return gain} \end{cases}$$

This function defines the carrier life time in the absorber section

$$\tau\alpha(N) := \left| \begin{array}{l} A \leftarrow 3 \times 10^9 \\ B \leftarrow 10^{-16} \\ \text{carrierT} \leftarrow \frac{1}{A + B \cdot N} \\ \text{return carrierT} \end{array} \right.$$

This function calculates the carrier density in the gain section, absorber section and the photon density

$$\begin{array}{l} \text{rate} := \\ \text{cg} \leftarrow 0.75 \cdot 10^8 \\ \text{h} \leftarrow 0.1455 \cdot 10^{-6} \\ \text{L} \leftarrow 2 \cdot 10^{-3} \\ \text{fg} \leftarrow 0.85 \\ \text{fa} \leftarrow 1 - \text{fg} \\ \beta \leftarrow 10^{-4} \\ \text{B} \leftarrow 10^{-16} \\ \alpha_d \leftarrow 1500 \\ \text{R} \leftarrow 0.32 \\ \alpha_m \leftarrow \frac{1}{L} \cdot \ln\left(\frac{1}{\text{R}}\right) \\ \alpha_{\text{tot}} \leftarrow \alpha_m + \alpha_d \\ e \leftarrow 1.6 \cdot 10^{-19} \\ m \leftarrow 1 \\ \delta t \leftarrow 100 \\ \Delta t \leftarrow 0.5 \cdot 10^{-13} \end{array}$$

```

I ← 0.085
J ←  $\frac{I}{L \cdot fg \cdot 2 \cdot 10^{-6}}$ 
P1 ← 0
Pg ← 0
Pa ← 0
Ng1 ← 0
Na1 ← 0
for t ∈ 1..2000000
    Ng2 ← Ng1 +  $\left( \frac{J}{e \cdot h} - \frac{Ng1}{\tau(Ng1)} - cg \cdot g(Ng1) \cdot Pg \right) \cdot \Delta t$ 
    Na2 ← Na1 +  $\left( -\frac{Na1}{\tau\alpha(Na1)} - cg \cdot g(Na1) \cdot Pa \right) \cdot \Delta t$ 
    P2 ← P1 +  $\left[ \beta \cdot B \cdot (Ng1^2) + cg \cdot (fg \cdot g(Ng1) + fa \cdot g(Na1)) - \alpha \cdot tot \right] \cdot P1 \cdot \Delta t$ 
    γa ← g(Na1) - α · tot
    γg ← g(Ng1) - α · tot
    Pa ←  $\frac{P1}{fa \cdot \left[ 1 + \frac{-\gamma a \cdot (1 - e^{-\gamma g \cdot L \cdot fg}) \cdot [e^{-\gamma a \cdot L \cdot fa} + R \cdot e^{(\gamma g \cdot L \cdot fg + \gamma a \cdot L \cdot fa)}]}{\gamma g \cdot (e^{-\gamma a \cdot L \cdot fa} - 1) \cdot (1 + R \cdot e^{\gamma a \cdot L \cdot fa})} \right]}$ 
    Pg ← Pa ·  $\frac{-\gamma a \cdot fa \cdot (1 - e^{-\gamma g \cdot L \cdot fg}) \cdot [e^{-\gamma a \cdot L \cdot fa} + R \cdot e^{(\gamma g \cdot L \cdot fg + \gamma a \cdot L \cdot fa)}]}{\gamma g \cdot fg \cdot (e^{-\gamma a \cdot L \cdot fa} - 1) \cdot (1 + R \cdot e^{\gamma a \cdot L \cdot fa})}$ 
    if t = m · Δt
        m ← m + 1
        Outm,1 ← P1
        Outm,2 ← Na1
        Outm,3 ← Ng1
        Outm,4 ← t · Δt
    P1 ← P2
    Ng1 ← Ng2
    Na1 ← Na2
return Out

```

# **Appendix C: Publications and presentations**

## **Publications:**

### **Self-pulsing 1050 nm quantum dot edge emitting laser diodes**

H.L. Liu, P.M. Snowton, H.D. Summers, G. Edwards, W. Drexler,  
Applied Physics Letters, Vol. 95, No. 10, 101111, (2009).

### **Self pulsing quantum dot lasers for optical coherence tomography**

Haoling Liu; Peter Snowton; Gareth Edwards; Wolfgang Drexler; Huw Summers  
SPIE Proceedings Vol. 7230, 72300 A (2009). Novel In-Plane Semiconductor  
Lasers VIII

## **Presentations:**

### **Photonics West, January 2009, Photonics West, San Jose USA**

Self pulsing quantum dot lasers for optical coherence tomography, H Liu, P.M.  
Snowton, G.T. Edwards, W. Drexler, H.D. Summers

### **SIOE 2008, March 31st-April 2nd, Cardiff, U.K.**

1050 nm Quantum Dots Laser Diodes for Optical Coherence Tomography, H. Liu,  
P.M. Snowton, H.D. Summers, W Drexler